QUANTUM TRANSPORT IN GRAPHENE

QUANTUM TRANSPORT IN GRAPHENE

Proefschrift

ter verkrijging van de graad van doctor
aan de Technische Universiteit Delft,
op gezag van de Rector Magnificus prof. ir. K. C. A. M. Luyben,
voorzitter van het College voor Promoties,
in het openbaar te verdedigen op dinsdag 27 april 2010 om 10:00 uur

door

Jeroen Bart OOSTINGA

natuurkundig ingenieur
geboren te Aduard.

Dit proefschrift is goedgekeurd door de promotoren:

Prof. dr. H. W. M. Salemink
Prof. dr. A. F. Morpurgo

Samenstelling promotiecommissie:

Rector Magnificus	voorzitter
Prof. dr. H. W. M. Salemink	Technische Universiteit Delft, promotor
Prof. dr. A. F. Morpurgo	Université de Genève, promotor
Prof. dr. Y. V. Nazarov	Technische Universiteit Delft
Prof. dr. S. G. Lemay	Universiteit Twente, Technische Universiteit Delft
Prof. dr. ir. B. J. van Wees	Rijksuniversiteit Groningen
Dr. F. Guinea	Instituto de Ciencia de Materiales de Madrid
Dr. ir. R. Hanson	Technische Universiteit Delft
Prof. dr. H. W. Zandbergen	Technische Universiteit Delft, reservelid

Keywords: nano-electronics, electronic devices, mesoscopic physics, electronic transport, graphene

Printed by: Gildeprint Drukkerijen, Enschede (The Netherlands)

Cover design: by Emeline Debackere, Ignacio Gutiérrez Lezama, Marjan Oostinga, Jeroen Oostinga. Cover picture: Resistance of a double-gated bilayer graphene device as a function of the voltages applied to both gate electrodes, showing the transition from a metallic to an insulating state in bilayer graphene (chapter 3). Inset: The honeycomb lattice structure of graphene drawn by a graphite pencil.

Casimir PhD series, Delft-Leiden 2010-10

ISBN 978-90-8593-073-0

An electronic version of this dissertation is available at
`http://repository.tudelft.nl/`.

Dit boek draag ik in het bijzonder op aan
mijn ouders,
mijn familie,
mijn vrienden.

Jeroen Oostinga

PREFACE

"Time flies when you are having fun", is what people usually say. This applies also to the four years of my PhD research project. It was an enjoyable time with numerous scientific and personal challenges. Since I am close to finish my PhD-project now, it is a good moment to look back. Let's go back ten years in time!

It was 28 January 1999 when I graduated as "natuurkundig ingenieur" at the University of Groningen. For several personal reasons I decided to search for a job as applied scientist at a research institute, instead of finding a PhD position at a university. Within a few months I found a job as "wetenschappelijk medewerker" at TNO (Netherlands Organisation for Applied Scientific Research) in The Hague, and I started to do contract research in the field of (electro)magnetics, mainly related to Defence Research. During my TNO-years, I learned a lot from my close colleagues, who made TNO a valuable work experience for me (in particular thanks to Frank, Rik, Arnold, Guus and Eugène: I enjoyed a lot working with you for almost seven years). In 2005, after the second reorganization that had hit me personally, I started to feel more and more uncomfortable at TNO. For this reason, I forced myself to think deeply and concretely about what I really wanted in my life. After a thorough orientation during my summer holidays of 2005, I decided to find a challenging PhD-position in nano-electronics. It felt like making an old wish come true!

The Kavli Institute of NanoScience of the Delft University of Technology attracted me the most, so I decided to write an application letter to the group "Molecular Electronics and Devices" (MED), led by Herre van der Zant, Alberto Morpurgo and Peter Hadley. After sending this letter, things started to accelerate. First I met Herre and Alberto to talk about my motivation to start a PhD in nano-electronics (on my 30th age!). Within a few days, Alberto offered me a PhD-position on "Quantum transport in graphene". He told me that graphene was just discovered and that he wanted to start working on it as soon as possible. I immediately decided to do it, because after reading the key-papers of that time I realized that graphene is a fascinating material. I left my permanent position at TNO in The Hague and started on 1 February 2006 as a "PhD-student" in Delft. Alberto, in the first place I am grateful to you for giving me the opportunity to work with you on graphene. I experience you as a hard-working and determined scientist. I am impressed of your scientific knowledge and the numerous creative scientific ideas you often have. Thanks for being my promoter and daily supervisor. Alberto, I wish you the luck and happiness in Geneva that you deserve. In the second place, I would like to thank Huub Salemink for being my promoter in Delft. In the first two years we hardly had any contact, but since I decided to continue my PhD in Alberto's new group in Geneva, you showed that you felt responsible for me and we had good contact on a more regular basis (thanks Huub).

During my first weeks in Delft, Peter Hadley took care of me and introduced me very well within the university (Peter, thanks for this). When I started, there was almost no time to refresh my mind in the field of condensed matter physics and mesoscopic physics, because the "graphene-team", which I had joined, needed to score scientifically as quickly as possible. Therefore, I experienced my start in Delft as jumping on a very fast train. The graphene-team was successful, because after six months we could submit our first paper to Nature. I would like to thank the graphene-team (Lieven, Pablo and Hubert of QT and Alberto of MED) for the discussions at the weekly graphene-meetings during which I learned "everything" I needed to know about graphene. In particular, I am grateful to Hubert and Pablo, who learned me the nanofabrication and cryogenic measurement techniques. In June 2006, Pablo and I visited Kostya Novoselov at the University of Manchester, who is one of the inventors of the "scotch-tape technique" to obtain graphene by peeling graphite: Kostya and co-workers, thanks for showing us the "tricks".

After the summer of 2006, I started to work more independently on graphene and I needed to build up my own dipstick measurement setup for graphene research. I would like to thank my (former) MED-colleagues for technical support, in particular Edgar, Kevin, Mascha and Jan. Furthermore, I would like to thank all@MED for having fun, for instance during the movie nights, the Christmas dinners and other enjoyable group activities (for instance the "groepsuitjes" in Noordwijk and Scheveningen): thanks to Anna, Helena, Iulean, Hangxing, Ignacio, Pietro, Monica, Jae, Piet, Edgar, Menno, Samir, Kevin, Jos (thanks for providing the TeX-template for my thesis), Benoit, Anne, Andreas, Bo, Murat, Warner, Gijs, Christian, Ferry, Hidde, Alexander, Mascha, Jan, Herre, Irma, Maria and Monique.

Till 2008, the graphene research remained a good collaboration between Lieven (QT) and Alberto (MED). For this reason, it was always possible to use the cryogenic measurement setups of QT without any problem (thanks to the QT-group, in particular Leo, Lieven, Ivo and Katja). After Pablo and Hubert left, new people joined the graphene-team: Lan, who started as a PhD of Lieven, and Saverio & Monica, who became postdocs of Alberto (Lan, good luck with finishing your work on graphene quantum dots; Saverio & Monica, I enjoyed our collaboration and I hope you both will have a promising future at the University of Exeter). I am also grateful to my MSc-students: Dominique and Samira. Due to our good collaboration we had nice results on the nanoribbons and AB-rings (Dominique, thanks for improving the "scotch-tape technique" and the cleaning procedure; with your chemistry background and creativity you helped us a lot). Furthermore, I would like to thank Yaroslav Blanter from the Theory Group for joining the weekly graphene-meetings and for having good discussions. You showed that it is useful to have a theoretician at the table when experimentalists try to interpret their measurement data. Doing experimental work is almost impossible without good support of experienced technicians, therefore I am very grateful to Jan & Mascha (MED), Ron (PD), Remco, Bram & Peter (providing helium and evaporator QT), Jaap (evaporator MB), Raymond & Jack (developing and making the best electronics!), Roel, Patrick, Marco, Marc, Arnold & Anja (DIMES cleanroom).

In September 2008, Alberto moved to Geneva to become professor of his new "Quantum Electronics" (QE) group. Quite some time before, Alberto had asked me whether I would like to join his new group. Since I preferred to continue working with Alberto (and I liked the challenge to live abroad for some years), I decided to join Alberto's new group at the University of Geneva, while remaining formally a PhD-student in Delft. I was not the only one, also Hangxing and Ignacio (Nacho) decided to move to Geneva. Together we formed the "Three Musketeers" who helped Alberto to move his equipment from Delft to Geneva and to build up the new lab. Unfortunately, the movement gave rise to huge conflicts within the TU Delft which made it an extremely unpleasant period for all people involved, including the Three Musketeers (Hangxing and Nacho, I am happy that the Three Musketeers will show up again in Delft during my defence: both of you as my "paranimfen" and me as the defender).

After our movement to Geneva, Alberto's new group started to grow fast: Niko (the Swissie), Masaki (the mighty Jappie postdoc) and Shimpei (Jappie, the Japan promoter) joined Ignacio (the Mexie) and Hangxing (the Chinie; good luck in your new job at Polymer Vision!) to work on organic crystals; Benjamin (the Frenchie) and Nuno (the Portie) started to work with me (the Dutchie) on graphene. To build up the new labs in Geneva, it took us a lot of time and energy, but we managed to do it with technical support of our new technician Alexander (and a few weeks help from our old technician Jan Toth from Delft). Besides building up a lab, we also needed to build up a new life in Geneva. QE-members, thanks for the enjoyable time during social activities, for instance, skiing in the Alpes, enjoying music at Jazz Festival Montreux, Rock Festival Paleo in Nyon and the concerts of "Pony Pony Run Run" and "Summer Went Too Soon", partying at Fête de Genève, Wii-party at Nacho's house, karting, visiting CERN and all the frequent social (drinking) events with all of you ("Let's eat BB at Les Brasseurs!"). In particular, I want to thank Shimpei for giving me the opportunity to visit Japan (for instance, Jun Takeya's lab at Osaka University, Yoshi Iwasa's lab at Tohoku University and the RIKEN workshop in Tokyo). Finally, I would like to thank all the secretaries: Irma, Maria, Monique

(MED) and Marja (PD) in Delft and Mélanie, Esther, Denise in Geneva for kindly helping me for whatever needed to be arranged.

While reading this preface, you may wonder whether I don't have a life outside the university, but I surely have and I am proud of that. When I moved to Geneva, I needed to leave my friends and family in The Netherlands. We kept in touch by modern communication (internet rules the world). For me, it turned out that Skype (and Gmail Videochat and Voipbuster) are media which almost compensate real physical visits to friends and familiy: Gerhart & Elvira, als goede vrienden voor het leven hebben we regelmatig en intensief skype-contact, waardoor we niet het gevoel hebben dat we verre vrienden zijn; Michiel & Marja, ik heb genoten van de "virtuele biertjes" die we regelmatig op zondagen gedronken hebben (Proost... en niet morsen op het toetsenbord!); alle anderen natuurlijk ook bedankt voor de gezellige skype-sessies! Furthermore, I really enjoyed the weekends when family and/or friends came to Geneva to visit me: dat jullie de moeite namen om te komen betekent veel voor mij; hiervoor bedankt allemaal! Besides physics, Scouting is an essential part of my life. When I was a young child I lost my heart at the scouting associations "de Bevers" in Lettelbert and later, when I was grown-up, "de Chauken" in Groningen. When I am at Scouting, I always feel home immediately: Bevers en Chauken, bedankt voor alle mooie belevenissen; een leven zonder scouting kan ik me niet voorstellen en ik verlang daarom naar de volgende scoutiviteiten!

Last but not least, I proudly thank my family for all their love and support in my life and for being a good example for me. Marjan & Addy (en de kleine Flo), Edwin & Annemieke (en de jongste Oostinga: Lola), ik kijk uit naar alle mooie momenten die we in de toekomst gezamenlijk zullen hebben. Pap & mam, het laatste woord wil ik tot jullie richten. Jullie staan altijd voor me klaar, welke keuzes ik ook neem in mijn leven. Deze onvoorwaardelijke steun is echt en voelt goed. Jullie betekenen daarom erg veel voor mij. Zonder jullie had ik nooit bereikt wat ik nu heb bereikt!

Jeroen Oostinga
Genève, 13 March 2010

CONTENTS

1

INTRODUCTION

Carbon is one of the most important building blocks of life on earth. It is even believed that life would not be possible without carbon. Carbon, which is the sixth element of the periodic table, is therefore one of the most fascinating elements. In nature, a large variety of carbon-based molecules exists, from CO_2, alcohol and oil to proteins, vitamins and DNA. Most of them are called organic molecules.

Since the twentieth century, organic molecules are extensively studied by scientists. New organic materials and molecules have been developed and their synthesis has given rise to a huge chemical industry in the world. Since several decades, numerous organic materials are also studied because of their interesting electronic properties. As a consequence, organic electronics has become nowadays a growing field of interest for science and industry.

1.1 CARBON ALLOTROPES

A special family of organic materials consists of the so-called carbon allotropes (figure 1.1). Carbon allotropes are well-defined structures which only consist of carbon atoms. The most well known among them are diamond and graphite, which are used by mankind since ancient times. Diamond is famous for its use in jewelry, but nowadays, it is also often used in industry, for example, to scratch or cut other materials, because it is one of the hardest materials on earth. Natural graphite was discovered more than 400 years ago for its use in pencils for writing and drawing. Since the twentieth century, it is also used for several industrial purposes, because, for instance, it is a good electrical conductor, it is cheap to produce and has a light weight. Graphite and diamond are both three-dimensional crystals.

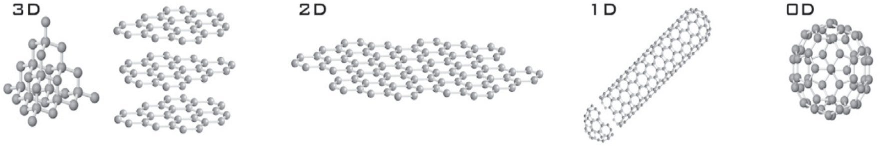

FIGURE 1.1: Structures of different allotropes of carbon. From left to right: three-dimensional diamond and graphite; two-dimensional graphene, one-dimensional nanotubes; zero-dimensional fullerenes (adapted from [2]).

More recently, new carbon allotropes of smaller dimensionality have been synthesized in laboratories. First, in the 1980s the fullerenes have been discovered, which are molecules in which the carbon atoms form closed structures (figure 1.1). The most famous fullerene is the buckyball which consists of a sphere of 60 carbon atoms (C_{60}). The fullerenes have interesting electronic properties, because they behave effectively as zero-dimensional systems. In the 1990s, another carbon allotrope has been discovered, namely the carbon nanotube (figure 1.1). Carbon nanotubes are cylindrical structures entirely made of carbon, and are effectively one-dimensional systems. Depending on the precise way in which the cylinder is made, carbon nanotubes have metallic or semiconducting/insulating properties. The discovery of fullerenes and carbon nanotubes opened the new field of carbon electronics [1].

The family of carbon allotropes seemed to be almost complete, only the two-dimensional allotrope was missing [3]. Since statistical mechanics predicts that two-dimensional crystals are thermodynamically unstable [4], it was believed that a two-dimensional crystal of carbon atoms could not exist in nature. However, this two-dimensional carbon allotrope, which is called graphene, had already been studied theoretically since the 1940s, when people started to investigate the electronic properties of graphite [5]. Basically, graphite is a stack of many graphene layers and its electronic properties can be analyzed starting from the bandstructure of graphene. Later, when the fullerenes and the carbon nanotubes were discovered, the bandstructure of graphene was studied in greater detail, because the fullerenes can be considered as graphene wrapped up into spheres and nanotubes as graphene rolled up into cylinders. Thus, some of the electronic properties of graphene were known, long before its experimental discovery.

In 2004, the scientific community was highly surprised when Andre Geim, Kostya Novoselov and co-workers at the University of Manchester discovered that, contrary to the theoretical predictions, graphene exists in nature [6,7]. They succeeded to isolate one single layer of graphite, which was the first experimental realization

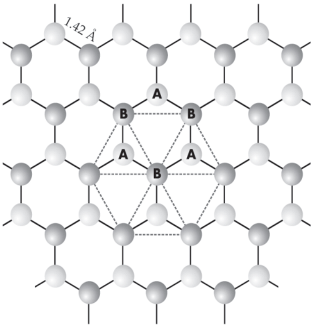

FIGURE 1.2: The honeycomb lattice structure of graphene, consisting of two interpenetrating triangular sublattices A and B (adapted from [8]).

of graphene. From this moment, all eyes were focussed on graphene for a number of reasons that we will discuss more in detail below. Not only the scientific community was attracted by graphene, also industrial research labs were interested in this new promising material.

1.2 DIRAC FERMIONS IN GRAPHENE

Most fascination for graphene comes from its peculiar electronic properties, which differ from those of usual materials. In conventional materials, the electron dynamics is well described by the Schrödinger equation. For low-energy electrons in graphene, however, the Schrödinger equation transforms into an equation which is formally identical to the Dirac equation (well-known from the theory of quantum electrodynamic). Usually, only relativistic particles, like neutrino's, are described by this relativistic version of the Schrödinger equation. Although the electrons in graphene are not relativistic, they are effectively described by the Dirac equation and, consequently, behave as Dirac fermions. Since two important theories, quantum electrodynamics and condensed matter physics, meet each other in graphene, scientists are intrigued by graphene's electronic properties [2,3,8].

In graphene's ultra-relativistic regime, the Fermi velocity of the electrons plays the role of the speed of light ($v_F \approx c/300 \approx 10^6$ m/s). Most interestingly, the Fermi velocity does not depend on energy in the low energy limit. As a consequence, the electron dynamics in graphene is described by a linear dispersion relation. Furthermore, the electrons have a pseudospin (in addition to the normal spin). This pseudospin is related to the honeycomb lattice structure of graphene, which consists of two sublattices (figure 1.2). The electron states have an amplitude on both

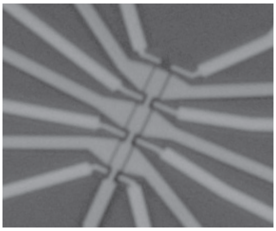

FIGURE 1.3: An optical picture of a graphene device on a silicon substrate. A graphene flake, obtained by mechanical exfoliation using adhesive tape, is contacted by metals to enable electronic transport measurements. This device also contains back- and sidegates for electrostatic control of the charge density.

sublattices and are therefore described by a two-component wavefunction (which is equivalent to a spinor). Due to this pseudospin, the electrons in graphene behave as chiral electrons. To understand electronic transport in graphene, we will consider in chapter 2 the properties of graphene's Dirac fermions in more detail.

1.3 GRAPHENE-BASED ELECTRONICS

People are intrigued by graphene, not only because it enables the study of Dirac fermions in solid state devices, but also because it is a promising new material for nano-electronics [3]. Graphene has strong interatomic bonds preventing the presence of structural defects and, therefore, consists of an almost perfect crystal quality. Since also extrinsic disorder in graphene is small, the charge carriers exhibit large mean free paths. Recently, room temperature mobilities higher than ~100,000 $\mathrm{cm}^2/\mathrm{Vs}$ have been reported [9]. This excellent electronic behaviour makes graphene a good candidate for electronic devices (figure 1.3).

Graphene is a zero-gap semiconductor, which enables electron and hole transport, without the need of chemical doping. By tuning the Fermi-level, by electrostatic gating of a graphene device, the carrier density can be controlled up to values higher than ~10^{13} cm^{-2}. At the crossing-point between valence and conduction band, which is called the Dirac point, the density of states vanishes, but the conduction remains non-zero ($\sigma_{min} \sim 4e^2/h$). This property prevents switching off the conduction and, therefore, creates an obstacle for the development of graphene field-effect transistors. Fortunately, strategies can be found to switch off conduction in graphene-based devices, as we will show in this thesis.

Furthermore, since the phase coherence length of electrons in graphene is large ($\sim 3-5\mu$m at 260 mK [10]), graphene is an interesting material for investigating quantum transport. In addition, electrons in graphene have a long spin relaxation length ($\sim 2\mu$m at room temperature [11]), which makes graphene also a good candidate for spin transport. In this thesis, we will study quantum transport in graphene devices to shine light on its phase coherent transport properties.

1.4 OUTLINE OF THIS THESIS

This thesis focusses on electronic transport in graphene devices on the sub-micron scale. Therefore, in chapter 2 several electronic properties of graphene will be discussed from a theoretical point of view. First, the bandstructure of graphene will be described, which shows why electrons in graphene behave as Dirac fermions. Additionally, the electronic properties of bilayer graphene, trilayer graphene and graphene nanoribbons will be considered. Subsequently, the electronic transport properties of graphene will be discussed. Also some essential concepts known from mesoscopic physics will be explained, like quantum interference phenomena and Josephson supercurrents. After these theoretical considerations, our experimental results will be presented in the following chapters.

In chapter 3, transport measurements on bilayer graphene devices will be discussed. Bilayer graphene is, like single-layer graphene, a zero-gap semiconductor and, consequently, exhibits metallic behaviour, irrespective of the charge density. However, in bilayer graphene an energy-gap between valence and conduction band opens when a perpendicular electric field is applied. We will show that in a bilayer graphene device, the conduction can be turned from metallic to insulating, simply by applying two gate-voltages, which enable the control of a perpendicular electric field as well as the Fermi energy in the bilayer.

Chapter 4 focusses on the transport properties of trilayer graphene. Trilayer graphene is a semi-metal with a small band-overlap. We have investigated the transport properties of double-gated trilayer graphene devices. We will show that the band-overlap increases by applying a perpendicular electric field, which manifests itself as an increase of the conduction at the charge neutrality point. Thus, next to bilayer graphene, trilayer graphene is a second material in which the bandstructure can be manipulated by applying control voltages in a double-gated device.

To investigate phase coherent transport properties of graphene, we have studied Josephson supercurrents and weak localization as well as the Aharonov-Bohm effect in graphene devices. In chapter 5, we will show that the occurence of bipolar supercurrent in graphene is a very robust phenomenon, while weak localization, which like supercurrent relies on the presence of time reversal symmetry and phase coherence, exhibits an uncommon dependence on the device under investigation. In particular, the observation of dissipationless supercurrents, even at the Dirac point, proofs that electronic transport in graphene is phase coherent. In chapter 6, we will consider the observation of the Aharonov-Bohm effect in ring-shaped structures of graphene, which is another manifestation of phase coherent transport.

Finally, we will consider the electronic transport properties of graphene nanoribbons in chapter 7. Graphene nanoribbons are (quasi-)one-dimensional structures etched out of graphene. We will show that the conduction of graphene nanoribbons vanishes at low charge density. This observation can be well explained by strong localization of electronic states due to disorder in the ribbon. The occurrence of strong localization in graphene nanoribbons is in sharp contrast with normal graphene devices, in which localization effects are often suppressed.

This thesis will be concluded with a summary of the experimental work that has been performed within this PhD research project.

1.5 REFERENCES

1. R. Saito, G. Dresselhaus, M. S. Dresselhaus, Physical Properties of Carbon Nanotubes (Imperial College Press, London, UK, 1998).
2. M. I. Katsnelson, Graphene: carbon in two dimensions, Materials Today 10 (1-2), 20-27 (2007).
3. A. K. Geim, K. S. Novoselov, The rise of graphene, Nature Materials 6, 183-191 (2007).
4. N. D. Mermin, Crystalline order in two dimensions, Phys. Rev. 176, 250-254 (1968).
5. P. R. Wallace, The band theory of graphite, Phys. Rev. 71 (9), 622-634 (1947).
6. K. S. Novoselov et al., Electric field effect in atomically thin carbon films, Science 306, 666-669 (2004).
7. K. S. Novoselov et al., Two-dimensional atomic crystals, PNAS 102 (30), 10451-10453 (2005).
8. A. K. Geim, A. H. MacDonald, Graphene: Exploring carbon flatland, Physics Today 60, 35-41 (2007).
9. K. I. Bolotin, Ultrahigh electron mobility in suspended graphene, Solid State Communication 146, 351-355 (2008).
10. F. Miao et al., Phase-coherent transport in graphene quantum billiards, Science 317, 1530-1533 (2007).
11. N. Tombros, C. Josza, M. Popinciuc, H. T. Jonkman, B. J. van Wees, Electronic spin transport and spin precession in single graphene layers at room temperature, Nature 448, 571-575 (2007).

2

THEORY

In this chapter, we consider electronic transport in graphene from a theoretical point of view. In §2.1 we derive the bandstructure of single-layer graphene by using a tight-binding model. Subsequently, the bandstructures of bilayer and trilayer graphene are discussed in §2.2. In §2.3 we consider the bandstructure of graphene nanoribbons with zigzag as well as armchair edges. The peculiar bandstructure of graphene gives rise to interesting transport properties, which will be discussed in §2.4. In §2.5 and §2.6, we focus on quantum interference phenomena and the Josephson effect in graphene. This chapter ends with §2.7 about the preparation and identification of graphene.

2.1 ELECTRONIC BANDSTRUCTURE OF GRAPHENE

Graphene is a conjugated sheet of carbon atoms arranged in a hexagonal lattice structure (figure 2.1) [1]. Since carbon is the sixth element of the periodic table, each atom has six electrons. The two inner electrons are core electrons ($1s^2$ orbitals) and the four outer electrons are valence electrons ($2s^2 2p^2$ orbitals). The core electrons are strongly bound to the nucleus and do not interact with neighbouring atoms. The valence electrons, on the other hand, interact with the surrounding carbon atoms. The chemical and electronic properties of graphene are therefore determined by the valence electrons.

The valence electrons of a carbon atom form $2s$, $2p_x$, $2p_y$ and $2p_z$ orbitals. These orbitals give rise to the covalent bonds between neighbouring atoms in a molecule or a lattice. In order to create these bonds, the $2s$ orbital hybridizes with $2p$ orbitals to form sp^n orbitals ($n = 1, 2, 3$). Three hybridization processes

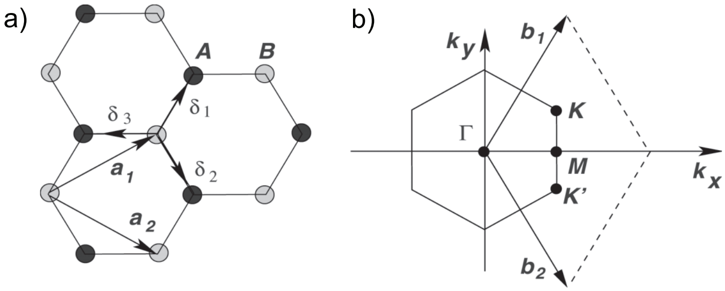

FIGURE 2.1: (a) The hexagonal lattice structure of graphene. The Bravais lattice contains two carbon atoms (A, B) per unit cell. The lattice vectors are $\mathbf{a}_1$ and $\mathbf{a}_2$. Three nearest neighbour vectors from sublattice B to A are shown (δ_i for $i = 1,2,3$). (b) The reciprocal lattice spanned by the vectors $\mathbf{b}_1$ and $\mathbf{b}_2$. The first Brillouin zone has a hexagonal shape giving rise to high symmetry points (Γ, M, K and K') (adapted from [5]).

are possible: sp^1 hybridization as in acetylene ($HC{\equiv}CH$); sp^2 hybridization as in graphite, carbon nanotubes, fullerenes and graphene; sp^3 hybridization as in diamond. These hybridization processes yield high binding energies resulting in strong covalent bonds.

2.1.1 TIGHT BINDING MODEL OF GRAPHENE

Here, we will focus on sp^2 hybridization in graphene and the consequences for the electronic properties. For each carbon atom in graphene, the $2p_x$ and $2p_y$ orbitals hybridize with the $2s$ orbital to form three sp^2 bonds with neighbouring atoms. These so-called σ-bonds are in-plane of the graphene sheet (xy-plane). The remaining $2p_z$ orbital is perpendicular to the graphene sheet. The p_z orbitals of neighbouring atoms overlap resulting in the π and π^*-bands. These electrons are weakly bound to the atoms and, therefore, are considered as free electrons or conduction electrons. The dispersion relation for the π and π^* bands of graphene can be calculated by using a tight binding model [1-5].

The Bravais lattice of graphene consists of a unit cell with a basis of two carbon atoms (figure 2.1) with lattice vectors:

$$\mathbf{a}_1 = \frac{a}{2}(3, \sqrt{3}) \tag{2.1}$$

$$\mathbf{a}_2 = \frac{a}{2}(3, -\sqrt{3}) \tag{2.2}$$

where a is the interatomic distance (C-C = 1.42 Å). The reciprocal lattice vectors of this Bravais lattice are

$$\mathbf{b}_1 = \frac{2\pi}{3a}(1, \sqrt{3}) \tag{2.3}$$

$$\mathbf{b}_2 = \frac{2\pi}{3a}(1, -\sqrt{3}) \tag{2.4}$$

In figure 2.1 the first Brillouin zone of graphene is shown, including the high symmetry points in momentum space: $\Gamma = (0,0)$, $M = (\frac{2\pi}{3a}, 0)$, $K = (\frac{2\pi}{3a}, \frac{2\pi}{3\sqrt{3}a})$ and $K' = (\frac{2\pi}{3a}, -\frac{2\pi}{3\sqrt{3}a})$.

The electronic states $|\psi\rangle$ and the corresponding energy values E_k are obtained by solving the Schrödinger equation

$$H|\psi\rangle = E_k|\psi\rangle \tag{2.5}$$

where H is the tight-binding Hamiltonian. The electronic wavefunctions should satisfy the Bloch condition, which means that, under translation of the crystal lattice vectors, they need to satisfy the relation

$$\psi(\mathbf{r} + \mathbf{R}) = e^{i\mathbf{k}\cdot\mathbf{R}}\psi(\mathbf{r}) \tag{2.6}$$

for $\mathbf{R} \in G$ where G denotes the set of all lattice vectors ($\mathbf{R} = n\mathbf{a}_1 + m\mathbf{a}_2$ with n and m are integers). Since graphene has two atoms per unit cell (A and B), the wavefunctions can be written as

$$\psi(\mathbf{k}, \mathbf{r}) = \frac{1}{\sqrt{N}}\left(c_A \sum_{\mathbf{R}_A}^{N} e^{i\mathbf{k}\cdot\mathbf{R}_A}\varphi_A(\mathbf{r} - \mathbf{R}_A) + c_B \sum_{\mathbf{R}_B}^{N} e^{i\mathbf{k}\cdot\mathbf{R}_B}\varphi_B(\mathbf{r} - \mathbf{R}_B)\right) \tag{2.7}$$

where N is the number of unit cells in the crystal lattice, $\mathbf{R}_A$ ($\mathbf{R}_B$) are the lattice vectors of sublattice A (B), φ_A (φ_B) are the atomic wavefunctions at the sites corresponding to sublattice A (B), and c_A (c_B) is the amplitude of ψ on sublattice A (B). The energy dispersion can be calculated by using the following relations for the wavefunctions on both sublattices:

$$\langle\varphi_A|H|\psi\rangle = E_k\langle\varphi_A|\psi\rangle \tag{2.8}$$

$$\langle\varphi_B|H|\psi\rangle = E_k\langle\varphi_B|\psi\rangle \tag{2.9}$$

In a first approximation, only the nearest neighbour interactions need to be considered in the tight-binding model, because the interaction terms corresponding to atoms at larger distances are relatively small. If we use the expression of the wavefunction of eq. (2.7), then eq. (2.8) can be rewritten as:

$$c_A\langle\varphi_A|H|\varphi_A\rangle + c_B\langle\varphi_A|H|\varphi_B\rangle(1+e^{-i\mathbf{k}\cdot\mathbf{a}_1}+e^{-i\mathbf{k}\cdot\mathbf{a}_2}) =$$

$$E_k\left(c_A\langle\varphi_A|\varphi_A\rangle + c_B\langle\varphi_A|\varphi_B\rangle(1+e^{-i\mathbf{k}\cdot\mathbf{a}_1}+e^{-i\mathbf{k}\cdot\mathbf{a}_2})\right) \tag{2.10}$$

and eq. (2.9) becomes

$$c_B\langle\varphi_B|H|\varphi_B\rangle + c_A\langle\varphi_B|H|\varphi_A\rangle(1+e^{i\mathbf{k}\cdot\mathbf{a}_1}+e^{i\mathbf{k}\cdot\mathbf{a}_2}) =$$

$$E_k\left(c_B\langle\varphi_B|\varphi_B\rangle + c_A\langle\varphi_B|\varphi_A\rangle(1+e^{i\mathbf{k}\cdot\mathbf{a}_1}+e^{i\mathbf{k}\cdot\mathbf{a}_2})\right) \tag{2.11}$$

In these equations, $\langle\varphi_A|\varphi_A\rangle = \langle\varphi_B|\varphi_B\rangle = 1$ and the on-site energy is defined as $\epsilon_0 = \langle\varphi_A|H|\varphi_A\rangle = \langle\varphi_B|H|\varphi_B\rangle \equiv 0$. Furthermore, the transfer integral matrix between nearest neighbours is $\gamma_0 = \langle\varphi_A|H|\varphi_B\rangle = \langle\varphi_B|H|\varphi_A\rangle \approx 2.8$ eV [5] and the overlap integral matrix between nearest neighbours is $\beta_0 = \langle\varphi_A|\varphi_B\rangle = \langle\varphi_B|\varphi_A\rangle = 0$. As a result, the Schrödinger equation can be approximated by the following matrix equation:

$$\begin{pmatrix} 0 & (1+e^{i\mathbf{k}\cdot\mathbf{a}_1}+e^{i\mathbf{k}\cdot\mathbf{a}_2})\gamma_0 \\ (1+e^{-i\mathbf{k}\cdot\mathbf{a}_1}+e^{-i\mathbf{k}\cdot\mathbf{a}_2})\gamma_0 & 0 \end{pmatrix}\begin{pmatrix} c_A \\ c_B \end{pmatrix} = E_k\begin{pmatrix} c_A \\ c_B \end{pmatrix} \tag{2.12}$$

The corresponding dispersion relation is

$$E(k_x,k_y) = \pm\gamma_0\sqrt{1+4\cos\left(\frac{3ak_x}{2}\right)\cos\left(\frac{\sqrt{3}ak_y}{2}\right)+4\cos^2\left(\frac{\sqrt{3}ak_y}{2}\right)} \tag{2.13}$$

Two bands are distinguished: the π band at $E<0$ and the π^* at $E>0$ (figure 2.2). Both bands touch at the high symmetry K points, which are the corners of the first Brillouin zone. Although there are six of these points, only two of them are independent: the K and the K' points (figure 2.2). Since there are two free electrons per unit cell, the π band, which is the valence band, is completely filled and the π^* band, which is the conduction band, is completely empty. Consequently, the Fermi energy is exactly at these K and K' points (at $E=0$).

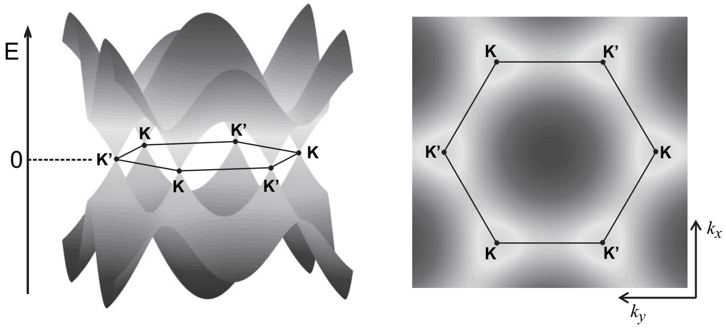

FIGURE 2.2: The bandstructure of graphene, which shows the valence band (or the π-band at $E < 0$) and the conduction band (or the π^*-band at $E > 0$). The Fermi energy is exactly at the K and K' points, where the valence and conduction bands touch (at $E = 0$). The states near the K and K' points form independent valleys in momentum space.

2.1.2 ELECTRONIC STATES IN THE LOW-ENERGY LIMIT

The electronic states close to the Fermi level ($E = 0$) determine the electronic transport properties of conduction electrons in graphene. Therefore, we consider the electronic states close to the K and K' points in the low-energy limit [2,4-8]. Since the electronic states in both valleys are not coupled, the electronic states in each valley can be studied separately by using an effective Hamiltonian for each valley. If $\mathbf{k} = \mathbf{K} + \kappa$ (and $\mathbf{k} = \mathbf{K}' + \kappa$) with $\kappa \ll \mathbf{K}, \mathbf{K}'$, then the tight-binding Hamiltonian (which is the 2x2 matrix in eq.(2.12)) can be approximated by

$$H_K = \begin{pmatrix} 0 & \frac{3\gamma_0 a}{2}\left(\kappa_x - i\kappa_y\right) \\ \frac{3\gamma_0 a}{2}\left(\kappa_x + i\kappa_y\right) & 0 \end{pmatrix} = \hbar v_F \begin{pmatrix} 0 & \kappa_x - i\kappa_y \\ \kappa_x + i\kappa_y & 0 \end{pmatrix} \quad (2.14)$$

at the K point, and

$$H_{K'} = \begin{pmatrix} 0 & \frac{3\gamma_0 a}{2}\left(\kappa_x + i\kappa_y\right) \\ \frac{3\gamma_0 a}{2}\left(\kappa_x - i\kappa_y\right) & 0 \end{pmatrix} = \hbar v_F \begin{pmatrix} 0 & \kappa_x + i\kappa_y \\ \kappa_x - i\kappa_y & 0 \end{pmatrix} \quad (2.15)$$

at the K' point. Both effective Hamiltonians operate on a two-component wavefunction $(\varphi_A, \varphi_B)^T$, where φ_A and φ_B are the components of the wavefunction ψ

on sublattices A and B, respectively. These effective Hamiltonians yield a linear dispersion relation:

$$\varepsilon_\kappa = \pm\left(\frac{3\gamma_0 a}{2}\right)|\kappa| = \pm\hbar v_F|\kappa| \tag{2.16}$$

As a consequence, the value of the Fermi velocity is constant: $v_F = \frac{3\gamma_0 a}{2\hbar} \approx 10^6$ m/s (notice that the direction of $\mathbf{v}_F = \hbar^{-1}\nabla_\kappa E$ is equal to the direction of κ). This gives rise to a conically shaped bandstructure at the K and K' points (figure 2.3).

An essential electronic property of graphene is revealed by inspection of the electronic wavefunctions. The effective Hamiltonians give rise to two-component wavefunctions for each valley:

$$\psi_{\pm,K}(\kappa) = \frac{1}{\sqrt{2}}\begin{pmatrix} e^{-i\theta_\kappa/2} \\ \pm e^{i\theta_\kappa/2} \end{pmatrix} \tag{2.17}$$

$$\psi_{\pm,K'}(\kappa) = \frac{1}{\sqrt{2}}\begin{pmatrix} e^{i\theta_\kappa/2} \\ \pm e^{-i\theta_\kappa/2} \end{pmatrix} \tag{2.18}$$

with $\theta_\kappa = \arctan(\kappa_x/\kappa_y)$ the angle of the wavevector κ in momentum space. The states with ± signs correspond to the energies $\varepsilon_\kappa = \pm\hbar v_F|\kappa|$. The two-component wavefunction $(\varphi_A, \varphi_B)^T$ has spinor-like properties and is therefore called a pseudospinor. For instance, a rotation of $\theta_\kappa = 2\pi$ around a K point leads to a π phase shift of the wavefunction. This π phase shift is in general known as a Berry's phase. Basically, this phase shift is identical to the phase that a spin 1/2 particle acquires when it makes an adiabatic rotation of 2π in a magnetic field (although one should realize that the pseudospin in graphene has nothing to do with the real electron spin).

An important property of the pseudospin is found after rewriting the effective Hamiltonian in the low-energy limit as:

$$H_K = \hbar v_F \sigma\cdot\kappa = -i\hbar v_F \sigma\cdot\nabla \tag{2.19}$$

where $\sigma = \sigma_x\hat{x} + \sigma_y\hat{y}$ and σ_x and σ_y are the Pauli matrices. In quantum mechanics, the helicity operator is defined as $\hat{h} \equiv \frac{1}{2}\sigma\cdot\frac{\kappa}{|\kappa|}$ [5], which is the projection of the pseudospin direction along the momentum direction. Since $H_K|\psi_\pm\rangle = \varepsilon_\kappa|\psi_\pm\rangle$ with $\varepsilon_\kappa = \pm\hbar v_F|\kappa|$, we obtain $\sigma\cdot\frac{\kappa}{|\kappa|} = \pm 1$. Consequently, at the K point, the pseudospin direction σ is parallel to κ for states with $\varepsilon_\kappa > 0$ and antiparallel for states with $\varepsilon_\kappa < 0$ (figure 2.3). In other words, the helicity is positive if $\varepsilon_\kappa > 0$ and negative if $\varepsilon_\kappa < 0$ (note that the helicity is reversed at the K' point).

One of the most striking results is that the effective Hamiltonian of graphene is equivalent to the Dirac equation, which is the relativistic version of the Schrödinger

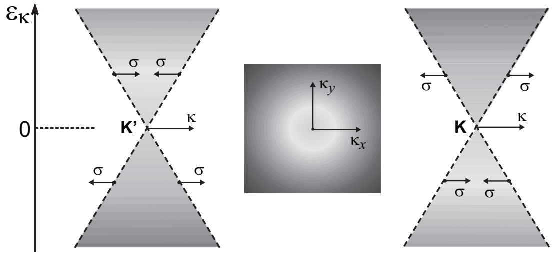

FIGURE 2.3: Both valleys at the Fermi energy have a conically shaped bandstructure. The dispersion is linear: $\varepsilon_\kappa = \hbar v_F|\kappa|$. Electron (hole) states in the conduction (valence) band at the K points possess a pseudospin whose direction is parallel (anti-parallel) to the momentum vector (κ). Note that the pseudospin directions are reversed at the K' points.

equation, known from quantum electrodynamics [9]. Consequently, the low-energy electrons in graphene behave as massless chiral charge carriers with similar properties as massless spin 1/2 relativistic particles†. However, in graphene the Fermi velocity and the pseudospin play the role of the speed of light and the real spin. Graphene is identified as the first material which supports Dirac fermions in two dimensions, and is therefore considered as an interesting playground for solid state physicists. Mesoscopic phenomena may manifest themselves differently in graphene than in 'conventional' materials [5,9]. Several electronic transport properties of graphene will be discussed in §2.4−2.6.

2.2 BANDSTRUCTURE OF BI- AND TRILAYER GRAPHENE

The electronic bandstructures of bilayer and trilayer graphene are different from single layer graphene. In the tight binding model of bilayer and trilayer graphene, not only the interaction between in-plane nearest neighbours, but also interactions between neighbours in different layers need to be included. The interactions between the layers highly depend on the layer stacking. Here we will consider Bernal stacking, which is the stacking order most often found in natural graphite. Bernal stacking is also called AB-stacking, because the A atoms in one layer are

---

† In relativistic dynamics, particles with a linear dispersion relation are massless, which is why electrons in graphene are referred to as "massless Dirac electrons". Note that in a periodic potential the effective mass is a tensor defined by the relation $m^{-1}_{\mu\nu} = \frac{1}{\hbar^2}\frac{d^2E}{dk_\mu dk_\nu}$ with μ and ν Cartesian coordinates. For particles with a linear dispersion relation, the tensor $\frac{d^2E}{dk_\mu dk_\nu}$ is not invertible (i.e. the determinant is zero) and therefore the effective mass cannot be defined, as it should be expected.

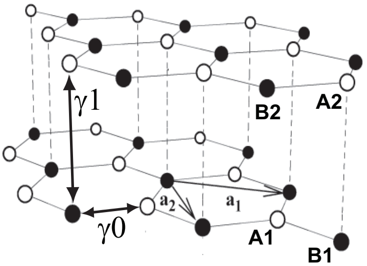

FIGURE 2.4: The lattice structure of Bernal stacked bilayer graphene (with sublattices A2 and B1 on top of each other). In a first approximation, only the tight binding parameters γ_0 and γ_1 are considered to obtain an effective Hamiltonian in the low-energy limit.

on top of the B atoms of an adjacent layer (as shown in figure 2.4 and figure 2.7 for bilayer and trilayer graphene, respectively). The interlayer distance for Bernal stacking is $t = 3.35$ Å.

2.2.1 BILAYER GRAPHENE

In figure 2.4, a Bernal stacking of bilayer graphene is shown. A unit cell consists of a basis of four atoms (i.e. A1, B1, A2 and B2). In the simplest tight binding calculation of bilayer graphene, which will be sufficient here, the following interaction terms are included [5,10,11]:

- The in-plane nearest neighbour coupling, which is similar to the one in single layer graphene, gives $\gamma_{A1B1} = \gamma_{A2B2} \equiv \gamma_0 \approx 2.8$ eV.
- The interlayer coupling between the $A2$ and $B1$ atoms, which are on top of each other in Bernal stacked bilayer graphene. This interaction gives rise to $\gamma_{A2B1} \equiv \gamma_1 \approx 0.39$ eV.

Similar to single-layer graphene, bilayer graphene has two valleys which are not coupled. To determine the electronic states in both valleys, McCann et al. have calculated effective Hamiltonians in the low-energy limit for both valleys (which we will not derive here) [10,11]:

$$H = \xi \begin{pmatrix} \Delta & 0 & 0 & \hbar v(\kappa_x - i\kappa_y) \\ 0 & -\Delta & \hbar v(\kappa_x + i\kappa_y) & 0 \\ 0 & \hbar v(\kappa_x - i\kappa_y) & -\Delta & \xi\gamma_1 \\ \hbar v(\kappa_x + i\kappa_y) & 0 & \xi\gamma_1 & \Delta \end{pmatrix} \tag{2.20}$$

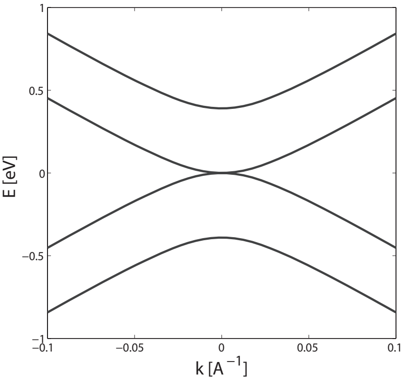

FIGURE 2.5: The low-energy bandstructure of bilayer graphene near a valley (K or K'). Bilayer graphene has four bands: two valence and two conduction bands. The two valence bands are completely filled, while the two conduction bands are empty. The highest valence and lowest conduction bands touch at the K and K' points, where the Fermi level is located.

This effective Hamiltonian acts on $\psi = (\psi_{A1}, \psi_{B2}, \psi_{A2}, \psi_{B1})^T$ at the K point ($\xi = 1$) and on $\psi = (\psi_{B2}, \psi_{A1}, \psi_{B1}, \psi_{A2})^T$ at the K' point ($\xi = -1$). The diagonal terms represent the on-site energies: Δ at sublattices A1 and B1, and $-\Delta$ at sublattices A2 and B2.

When the on-site energy terms of both layers are identical ($\Delta = 0$), then the energy dispersion close to the K points can be approximated by [10,12]

$$\varepsilon_\kappa = \pm\frac{\gamma_1}{2} \pm \sqrt{\frac{\gamma_1^2}{4} + (\hbar v \kappa)^2} \tag{2.21}$$

with $v = \frac{3\gamma_0 a}{2\hbar}$. This relation shows that bilayer graphene has four electronic bands, which are plotted in figure 2.5. Both valence bands are completely filled and both conduction bands are empty. Since the higher valence and the lowest conduction bands touch at the K and the K' points in momentum space, the Fermi level is exactly at these points ($E = 0$).

In the low-energy limit, we only need to consider the electronic states corresponding to the lowest valence and highest conduction bands. In a first approximation, the effective Hamiltonians for these bands become [9,10]

$$H_K = -\frac{\hbar^2}{2m}\begin{pmatrix} 0 & (\kappa_x - i\kappa_y)^2 \\ (\kappa_x + i\kappa_y)^2 & 0 \end{pmatrix} \tag{2.22}$$

and

$$H_{K'} = -\frac{\hbar^2}{2m}\begin{pmatrix} 0 & (\kappa_x + i\kappa_y)^2 \\ (\kappa_x - i\kappa_y)^2 & 0 \end{pmatrix} \tag{2.23}$$

which operate on the two-component wavefunction $(\varphi_{A1}, \varphi_{B2})^T$. Notice that, contrary to single layer graphene, the components of this wavefunction are related to sublattices $A1$ and $B2$, which are in *different* layers. The effective Hamiltonian yields a parabolic dispersion relation:

$$\varepsilon_\kappa = \pm\frac{\hbar^2\kappa^2}{2m} \tag{2.24}$$

and the electrons and holes have a non-zero effective mass: $m = \gamma_1 / v^2$.

The two-component wavefunctions of the effective Hamiltonian are

$$\psi_{\pm,K}(\kappa) = \frac{1}{\sqrt{2}}\begin{pmatrix} e^{-i\theta_\kappa} \\ \pm e^{i\theta_\kappa} \end{pmatrix} \tag{2.25}$$

and

$$\psi_{\pm,K'}(\kappa) = \frac{1}{\sqrt{2}}\begin{pmatrix} e^{i\theta_\kappa} \\ \pm e^{-i\theta_\kappa} \end{pmatrix} \tag{2.26}$$

Like in single layer graphene, these electron states possess chirality [5,10,12]. While the electrons in single layer graphene behave as massless chiral particles, the electrons in bilayer graphene behave as massive chiral particles. Another difference between both graphene types is the Berry's phase. The two-component wavefunctions of the bilayer show that a rotation of κ around the K point (i.e. $\theta\kappa = 2\pi$) results in a 2π phase shift of the wave function. Thus, the Berry's phase in bilayer graphene is 2π, while the Berry's phase in single layer graphene is π.

So far, we assumed that the diagonal terms of the Hamiltonian are zero ($\Delta = 0$ in eq. (2.20)). However, the diagonal terms of the Hamiltonian become non-zero when both layers have different on-site energies (Δ for the atoms A1 and B1, and $-\Delta$ for the atoms A2 and B2) or, in other words, when the symmetry between both layers is broken [11]. If the layer symmetry is broken, the effective Hamiltonian in the low energy-limit can be approximated by

$$H_K = \begin{pmatrix} \Delta & -\frac{\hbar^2}{2m}(\kappa_x - i\kappa_y)^2 \\ -\frac{\hbar^2}{2m}(\kappa_x + i\kappa_y)^2 & -\Delta \end{pmatrix} \tag{2.27}$$

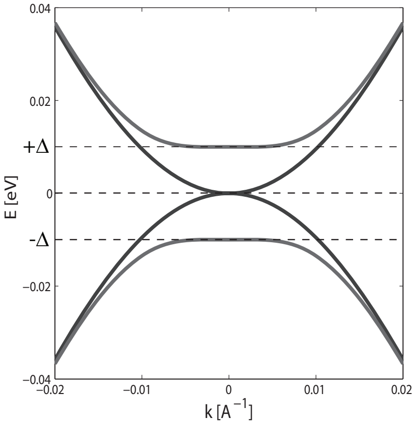

FIGURE 2.6: In the symmetric case ($\Delta = 0$), the lowest conduction and the highest valence band touch (black). In the asymmetric case ($\Delta \neq 0$), both bands are pushed away to higher energies and a bandgap opens (gray; here $\Delta = 0.01$ eV)

The asymmetry between sublattices A1 and B2 yields the following dispersion relation for the highest valence and lowest conduction bands (if $\Delta \ll \gamma_1$)

$$\varepsilon_\kappa = \pm\sqrt{\Delta^2 + \left(\frac{\hbar^2\kappa^2}{2m}\right)^2} \tag{2.28}$$

Most strikingly, a non-zero Δ gives rise to a bandgap at the K and K' points: $E_{gap} = 2\Delta$. While the highest valence and lowest conduction bands touch at the K points in the symmetric case, they are pushed away to higher energies when the symmetry is broken (figure 2.6). As a consequence, a bandgap opens and bilayer graphene can be turned from a metal into an insulator by just breaking the symmetry between both layers.

2.2.2 TRILAYER GRAPHENE

In figure 2.7, a Bernal stacking of trilayer graphene is shown (B1-A2-B3 atoms stacked on top of each other). To be capable of describing the low-energy electronic properties of trilayer graphene properly, the complete set of tight binding parameters of graphite needs to be used in the bandstructure calculation, which are γ_i for $i = 0,..,5$ (γ_0 and γ_1 are identical to bilayer graphene) [5,13].

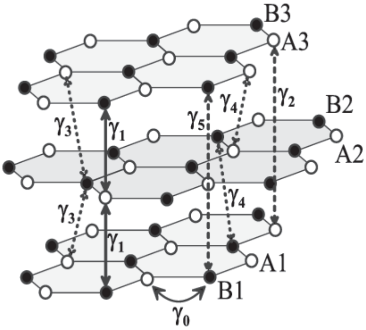

FIGURE 2.7: Bernal stacked trilayer graphene (with sublattices B1, A2, B3 on top of each other). The tight binding model is described by the same set of parameters as for graphite: $\gamma_0, \gamma_1, \gamma_2, \gamma_3, \gamma_4$ and γ_5 (adapted from [14]).

- γ_2 is a coupling between the outer layers of trilayer graphene (between A1 and A3 atoms). This interaction yields $\gamma_{A1A3} \equiv \gamma_2 \approx -0.020$ eV.
- The interlayer coupling between the atoms $A1 - B2$ and $B2 - A3$ gives rise to $\gamma_{A1B2} = \gamma_{B2A3} \equiv \gamma_3 \approx 0.315$ eV.
- The interlayer coupling between the atoms $A1 - A2$, $B1 - B2$, $A2 - A3$ and $B2 - B3$ yields $\gamma_{A1A2} = \gamma_{B1B2} = \gamma_{A2A3} = \gamma_{B2B3} \equiv \gamma_4 \approx 0.044$ eV.
- γ_5 is a coupling between the outer layers of trilayer graphene (between B1 and B3 atoms). This interaction gives rise to $\gamma_{B1B3} \equiv \gamma_5 \approx 0.038$ eV.

Koshino et al. have derived an effective tight-binding Hamiltonian in the low-energy limit for each valley (which we will not derive here) [14]. They showed that the effective Hamiltonian of trilayer graphene has blocks which are similar to the effective Hamiltonians of single-layer and bilayer graphene. In a first approximation (by setting all parameters zero, except γ_0 and γ_1), the effective Hamiltonian of trilayer graphene gives rise to four low-energy bands, which appear around the K and K' points: two linear and two parabolic bands, which meet at the Fermi level, $E = 0$ (figure 2.8a).

Moreover, Koshino et al. showed that the linear and parabolic bands hybridize when the interlayer symmetry of trilayer graphene is broken. As a result, the linear bands are pushed away from the Fermi level and the parabolic bands start to overlap (figure 2.8b). Consequently, only the overlapping parabolic bands give rise to a density of states at the Fermi level. More interestingly, the band-overlap and the corresponding density of states increase if the asymmetry becomes larger. This

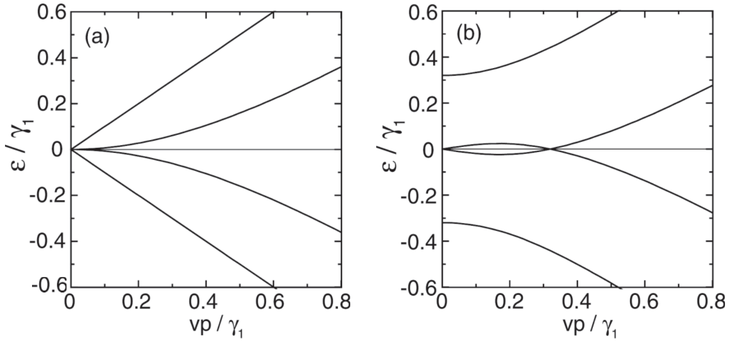

FIGURE 2.8: First approximation of the low-energy bandstructure of trilayer graphene, near a K point (the energy in dimensionless units $[\varepsilon/\gamma_1]$ versus momentum in dimensionless units $[\upsilon p/\gamma_1]$). (a) If the interlayer symmetry is not broken, then two linear and two parabolic bands are present at the Fermi level. (b) If the interlayer symmetry is broken, only both parabolic bands remain at the Fermi level and both linear bands are shifted to higher energies. The overlap between the parabolic bands depends on the interlayer asymmetry (adapted from [14]).

result is in stark contrast with bilayer graphene, where symmetry breaking induces a bandgap in the bandstructure.

2.3 BANDSTRUCTURE OF GRAPHENE NANORIBBONS

Graphene is a two-dimensional crystal. However, narrow channels can be cut out of a sheet to create (quasi-)one-dimensional graphene. Electrons will be laterally confined in narrow graphene ribbons, similar to constrictions in conventional 2DEGs. The narrow width yields the quantization of the wavevector in lateral direction: $k_y W \sim n\pi$ (for $n \geq 1$) where a square-well potential equal to the ribbon width (W) is presumed [15]. For two-dimensional graphene, the dispersion relation at the Fermi level is: $E_{2D} = \hbar\upsilon_F\sqrt{k_x^2 + k_y^2}$. Using the quantization of k_y, the dispersion relation of one-dimensional graphene is obtained: $E_{1D} = \hbar\upsilon_F\sqrt{k_x^2 + (n\pi/W)^2} = \sqrt{E_x^2 + E_n^2}$ with $E_n \equiv n\hbar\upsilon_F\pi/W$. This simple calculation results in a bandgap at the Fermi level ($E_F = 0$), since the density of states vanishes at energies below the minimum value of the lowest subband, $|E| < E_1(k_x = 0) = \hbar\upsilon_F\pi/W \approx (2eV \cdot nm)/W$ [16]. However, this first approximation is not very accurate, because the specific properties of armchair and zigzag edges are not taken into account. When these boundary conditions are included in the calculations [17-19], a different result is obtained, as we will show below.

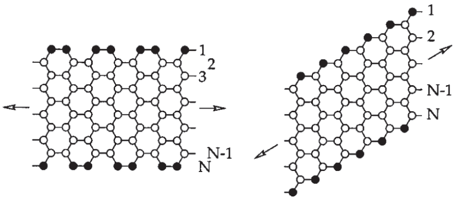

FIGURE 2.9: An armchair ribbon (left) and a zigzag ribbon (right). The number of carbon rows (N) in lateral direction characterize the ribbon width (adapted from [17]).

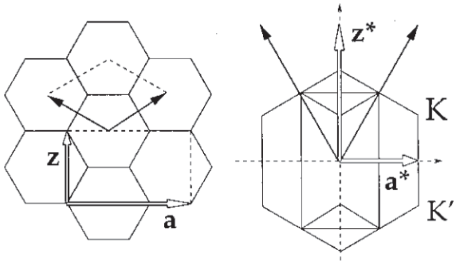

FIGURE 2.10: The defined unit cell for graphene nanoribbons (left) and the corresponding reciprocal lattice with the first Brillouin zone (right) compared with normal graphene (adapted from [17]).

2.3.1 RIBBONS WITH ARMCHAIR EDGES

In graphene ribbons, two different types of edges are distinguished: zigzag and armchair edges (figure 2.9). Both types have 30 degrees difference in cutting direction from a sheet of graphene. Intermediate cutting directions will result in mixed edges. Nakada et al. have calculated the tight binding model of ribbons with zigzag as well as armchair edges [17]. They considered a rectangular unit cell with a basis of four atoms. In figure 2.10, the vectors $\mathbf{a}$ and $\mathbf{z}$ are the translational vectors of the unit cell with $\mathbf{a}$ ($\mathbf{z}$) parallel to an armchair (zigzag) edge. The reciprocal lattice spanned by the translational vectors $\mathbf{a}^*$ and $\mathbf{z}^*$ gives rise to a rectangular Brillouin zone which is half the size of the hexagonal Brillouin zone of a normal sheet of graphene (figure 2.10). Nakada et al. used a zone-folding technique to calculate the bandstructure [1,17]. With this technique, the bandstructure of two-dimensional graphene is projected on the corresponding axis of the ribbon, which is $\mathbf{a}^*$ for armchair ribbons and $\mathbf{z}^*$ for zigzag ribbons. As a result, the projected K-points appear at $k = 0$ for armchair ribbons and at $k = \pm 2\pi/3\sqrt{3}a$ for zigzag ribbons (figure 2.10, 2.11).

The bandstructures of armchair ribbons with three differents widths are shown in figure 2.12a-c. Two of these ribbons have a bandgap at the Fermi level ($N = 4$

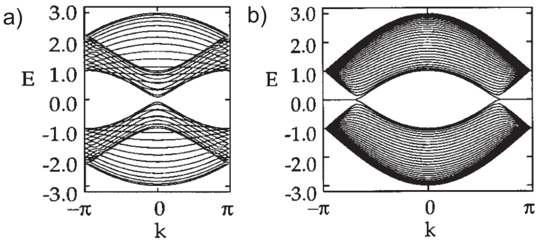

FIGURE 2.11: The bandstructures of (a) a $N = 30$ armchair and (b) a $N = 30$ zigzag ribbon (with k in units of $(\sqrt{3}a)^{-1}$; adapted from [17]).

and $N = 6$), while the third ribbon is gapless ($N = 5$). In general, Nakada et al. showed that ribbons are gapless when $N = 3p+2$, where p is a positive integer, and gapped otherwise (see for example figure 2.11a, which shows the bandstructure of an armchair ribbon of $N = 30$). Thus, an armchair nanoribbon is metallic or insulating, dependent on its widths (figure 2.13a; note that the bandgap decreases if N increases).

The bandstructure of armchair ribbons is slightly different when the difference between edge and bulk atoms is included in the calculations [19]. For instance, the carbon atoms at the edges have dangling bonds which are terminated by 'foreign' atoms or molecules (e.g. hydrogen). Consequently, the σ bonds between edge atoms will not be similar to the bonds between bulk atoms and, therefore, the interatomic distance will be different at the edges. This will lead to different values of the transfer integrals and on-site energies ($\gamma_0^{edge} \neq \gamma_0^{bulk}$ and $\epsilon_0^{edge} \neq \epsilon_0^{bulk}$). Son et al. included such edge effects in their bandstructure calculations [19] and, surprisingly, found out that all armchair ribbons, irrespective of the width, have a bandgap (figure 2.13b).

2.3.2 RIBBONS WITH ZIGZAG EDGES

The bandstructure of zigzag ribbons is remarkably different from armchair ribbons [17,20]. Figure 2.12d-f show the bandstructures of zigzag ribbons with different widths. Surprisingly, in the region between the projected K point and the edge of the Brillouin zone, $|k| \in \frac{\pi}{\sqrt{3}a}[\frac{2}{3}, 1]$, the highest valence and lowest conduction bands are almost flat. The band flatness increases with the ribbon width (see for example figure 2.11b, which shows the bandstructure of a zigzag ribbon of $N = 30$). Independent of the width, both bands are degenerate at $|k| = \pi/\sqrt{3}a$ and, consequently, there is no bandgap in zigzag ribbons. Nakada et al. examined the charge density distribution of a zigzag ribbon and found that the states in the flat

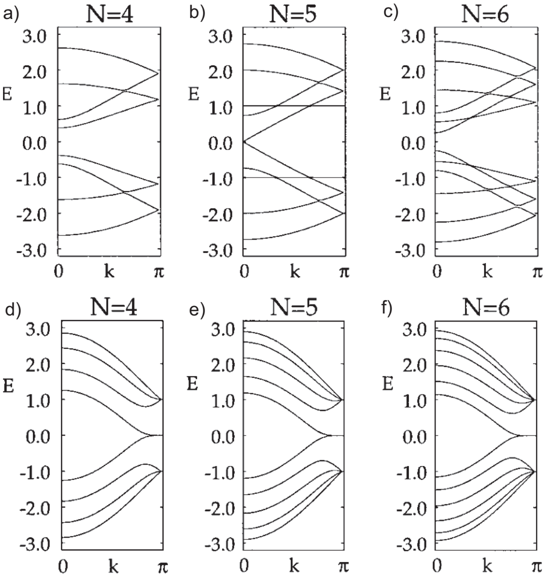

FIGURE 2.12: The bandstructures of armchair (a-c) and zigzag nanoribbons (d-f) for different widths ($N = 4,5,6$). Zigzag ribbons are gapless and armchair ribbons are, dependent on their width, either gapped ($N = 4,6$) or ungapped ($N = 5$) (with k in units of $(\sqrt{3}a)^{-1}$; adapted from [17]).

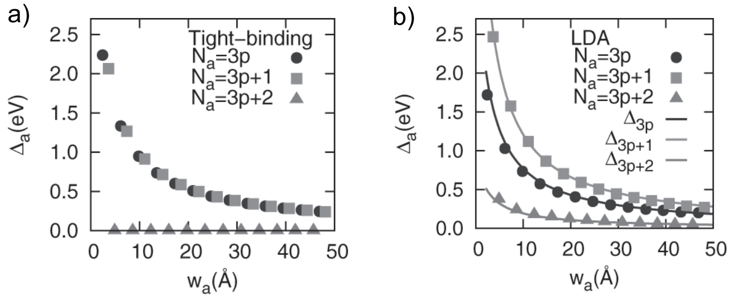

FIGURE 2.13: (a) Bandgap calculations of armchair ribbons as a function of the width w_a (according to the model of Nakada et al. [17]). (b) Bandgap calculations by including the deviation of tight binding parameters at the edges (model of Son et al.). According to this model, all armchair ribbons are gapped, irrespective of the width (adapted from [19]).

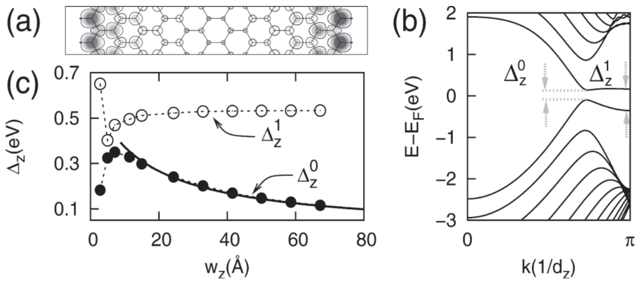

FIGURE 2.14: (a) The spatial distribution of the charge difference between both magnetic polarizations (light and dark gray denote the opposite polarizations α and β). (b) The bandstructure of a $N = 12$ zigzag nanoribbon (with k in units of $d_z^{-1} = (\sqrt{3}a)^{-1}$ showing the direct bandgaps Δ_z^0 and Δ_z^1 at $k = \frac{2\pi}{3\sqrt{3}a}$ and $k = \frac{\pi}{\sqrt{3}a}$, respectively. (c)The direct bandgaps Δ_z^0 and Δ_z^1 as a function of width w_z (adapted from [19]).

bands correspond to electronic states localized at the zigzag edges [17,20]. The density of states at the edges gives rise to metallic behaviour of zigzag ribbons, irrespective of the width.

The bandstructure of zigzag ribbons is slightly different when magnetic ordering of spins is included in the calculations [19,20]. Son et al. showed that magnetic ordering gives rise to a ground state, in which the atoms of both sublattices are spin polarized with opposite spin orientations (i.e. an antiferromagnetic ordering with respect to sublattices A and B). Since both edges correspond to different sublattices and the edge states decay exponentially towards the center of the ribbon, both edges are effectively polarized with opposite magnetization. Due to this magnetic ordering, the sublattice symmetry is broken and gives rise to a bandgap in zigzag nanoribbons (figure 2.14). However, we should note that Son et al. also showed that zigzag ribbons can be turned into half-metals (supporting spin polarized currents) when opposite electrostatic potentials are applied to both edges [21]).

2.4 ELECTRONIC TRANSPORT IN GRAPHENE

The electronic transport properties of graphene are determined by the electronic states around the Fermi energy. In undoped graphene, the Fermi level is exactly at the K and K' points. Around these points, the electronic states are described by a linear dispersion relation. The sublattice symmetry gives rise to a pseudospin and a chirality. As a consequence, graphene has some unique transport properties, like an anomalous quantum Hall effect and a minimum conductivity at the

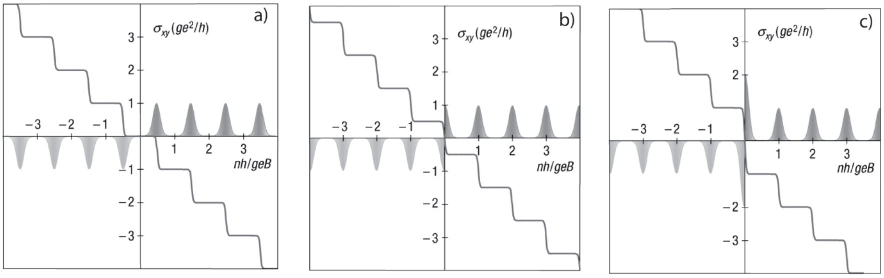

FIGURE 2.15: Schematic picture of the Hall conductivity σ_{xy} as a function of carrier concentration for usual materials (a), single-layer graphene (b) and bilayer graphene (c). Additionally, the sequence of Landau levels as a function of carrier concentration is shown (adapted from [12]).

charge neutrality point. Furthermore, graphene exhibits very high electron and hole mobilities, exceeding ~ 10^5 cm^2/Vs at room temperature.

2.4.1 QUANTUM HALL EFFECT

If a magnetic field is applied perpendicular to a two-dimensional conductor, the electrons experience a Lorentz force and move along circular trajectories. In the quantum regime, these closed cyclotron orbits give rise to discrete energy levels: Landau levels. For usual conductors, the energies of these Landau levels equal $E_N = \pm\hbar\omega_c(N+1/2)$ for electrons (+) and holes (−), with $\omega_c = eB/m$ being the cyclotron frequency and N the quantum number which refers to the Nth Landau level [15,22]. Electrons and holes can only occupy these discrete energy levels and the density of states vanishes between the Landau levels. At each Landau level, the density of states is $n = g_s g_v eB/h$ (with g_s and g_v the spin and valley degeneracies). Since the lowest Landau level is at $E = \frac{1}{2}\hbar\omega_c$, a magnetic field induces an energy-gap at $E = 0$. Note that the level spacing between the Landau levels, $\Delta E = \hbar eB/m$, is independent of N.

Due to the presence of Landau levels, the electronic states at the edges have unique properties. If the Fermi level is between two Landau levels, there are no bulk states in the conductor which can contribute to the conductivity. Electronic transport through the conductor only occurs via edge states, which form one-dimensional conducting channels at the physical edges of the device. Electrons at one edge propagate in one direction (k states), while electrons at the other edge propagate in opposite direction ($-k$ states). Since each edge consists of only k or $-k$ states (depending on the sign of the magnetic field), backscattering in the conducting edge channels is prevented and, consequently, the longitudinal resistance (measured in a four-terminal configuration) vanishes. At the same time, the Hall conductance becomes quantized: $G_{xy} = \pm g_s g_v N e^2/h$ with N the number of edge channels. This phenomenon is called the integer quantum Hall effect (figure 2.15a) [15,22].

In single-layer graphene, the quantization of the Hall conductivity is remarkably different [23,24]. The chirality of the electrons gives rise to a Berry's phase of π and, consequently, the Landau levels appear at different energy values: $E_N = \pm v_F \sqrt{2e\hbar B N}$ (notice that the level spacing ΔE_N depends on N). Most surprisingly, a Landau level is present at $E = 0$, irrespective of the magnetic field. A unique property of this zeroth Landau level is that it consists of electron and hole states. At this Landau level, the degeneracy per charge carrier type is two times smaller than at higher order Landau levels. Therefore, the density of the electron (hole) states at the zeroth Landau level is only $n = 2eB/h$, while the density at the higher order Landau levels equals $n = 4eB/h$ (figure 2.15b). As a consequence, single-layer graphene exhibits a different sequence of quantization levels of the Hall conductance: $G_{xy} = \pm 4e^2/h(N + 1/2)$ (the factor 4 arises from the double spin and double valley degeneracies). This new quantization sequence is called the half-integer quantum Hall effect to make a distinction with the integer quantum Hall effect in usual conductors (figure 2.15).

In bilayer graphene, the electrons also have a chirality, but here with a Berry's phase of 2π [12]. Therefore, the Landau levels of bilayer graphene appear at values which are different from single-layer graphene (and also different from usual conductors): $E_N = \pm \hbar\omega_c \sqrt{N(N+1)}$ with $\omega_c = eB/m$. Similar to single-layer graphene, a Landau level is present at $E = 0$, where electron and hole states co-exist. However, in bilayer graphene, the degeneracy at the zeroth Landau level is equal to the degeneracy at the higher order Landau levels, giving a density of $n = 4eB/h$ per Landau level for each charge carrier type (figure 2.15c). Consequently, the quantization sequence of the Hall conductance of bilayer graphene is: $G_{xy} = \pm 4Ne^2/h$ for $N \geq 1$ (figure 2.15c). The double step in the quantization sequence, which appears at $E = 0$, is a unique property of bilayer graphene, and allows the bilayers and single-layers to be discriminated experimentally.

2.4.2 MINIMUM CONDUCTIVITY

Another fascinating transport property of graphene, is its minimum conductivity at the Dirac point (figure 2.16). When the Fermi level goes from conduction band, where electrons carry the current, to the valence band, where holes carry the current, the Fermi level needs to cross the Dirac point. Although the carrier density vanishes at the Dirac point, the conductivity remains finite at a value of $\sim 4e^2/h$. This surprising result is not completely understood and has stimulated many groups to reveal its physical origin.

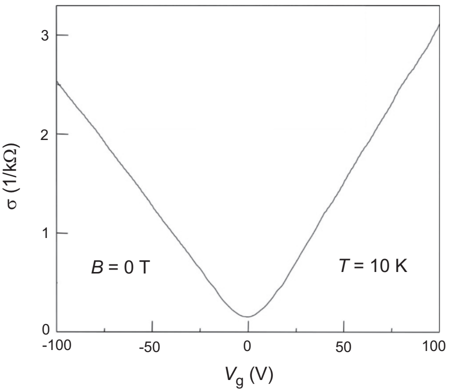

FIGURE 2.16: The conductivity σ as a function of the gate voltage V_g for a typical graphene device (note that the charge density n depends linearly on V_g). The conductivity reaches a minimum value at the charge neutrality point (i.e. Dirac point), which is $\sigma_{min} \approx 4e^2/h$. At high electron and hole density, the conductivity depends linearly on V_g or n (adapted from [5]).

A minimum conductivity has been theoretically predicted for chiral electrons in graphene in the ballistic regime [25,26]. Calculations have shown that, when the Fermi level is at the Dirac point, electron transport may still occur due to the presence of evanescent waves. Such evanescent waves should give rise to a minimum conductivity of $\sigma_{min} = \frac{4e^2}{\pi h}$. This predicted minimum value is only observed experimentally in very short graphene devices, where the assumption of ballistic transport is more closely matched [27,28]. Most often, however, values of $\sigma_{min} \gtrsim 4e^2/h$ are measured in larger devices [9,29,30].

This higher experimental value of σ_{min} can be explained by charge inhomogeneities that can play a dominant role when the Fermi energy is small. In this regime, close to the Dirac point, potential fluctuations yield charge density fluctuations and, as a result, puddles of electrons and holes are formed [31]. Puddle formation can be understood by considering potential fluctuations due to the presence of charged impurities close to the graphene sheet [32-34]. Alternatively, the presence of ripples in the graphene sheet may give rise to these potential fluctuations [35]. Although the physical origin of charge inhomogeneities is still not fully understood, it is widely believed that they dominate the transport properties close to the charge neutrality point in large devices and, consequently, affect the value of the minimum conductivity [9,29,30,34].

2.4.3 HIGH MOBILITY

Most transport measurements reported so far are done on graphene sheets placed on a SiO_2 substrate. Mobility values exceeding 10,000 cm^2/Vs are measured for electrons and holes, even up to room temperature [9]. The scattering mechanism that limits the mobility is not revealed yet. Measurements have shown that phonon scattering is very weak in graphene, because the mobility shows almost no temperature dependence. Furthermore, it is not believed that atomic defects limit the mobility in graphene, since graphene's lattice structure is of very high quality. Therefore, it is expected that other scattering mechanisms limit the mobility in graphene [29,30,35].

It is currently believed that in graphene on a SiO_2 substrate, the conductivity is mainly limited by long-range scattering mechanisms, resulting in a conductivity that depends linearly on the charge density, $\sigma \propto n$ (figure 2.16) [29,30,32,33,35]. Possibly, charged impurities close to the graphene sheet are responsible for this long-range scattering. Such charged impurities may be adatoms on the surface of graphene, atoms between graphene and the substrate or charges in the substrate. However, this has not been proven yet and, therefore, the origin of long-range scattering is still under debate [30,33,36].

In addition to long-range scattering, also short-range scattering may occur in graphene (for example due to point defects and edge disorder). Theory predicts that short-range scattering gives rise to a conductivity which is independent of the charge density. If short-range scattering occurs in combination with long-range scattering, the conductivity will exhibit a sublinear dependence on the charge density. Such a sublinear dependence has been observed in several experiments, in particular on high-mobility graphene devices [29,30,33,35].

Recently, the first experimental results on transport in annealed suspended graphene devices have been reported [37-39]. By suspending graphene, scatterers from the SiO_2 substrate are eliminated (not only charged impurities which may be present in SiO_2, but also phonons which remotely interact with charges in graphene at high temperatures [40,41]). Furthermore, by annealing graphene devices, it is ensured that the amount of adatoms on the surface (e.g. charged impurities) is reduced. This results in 'cleaner' graphene devices, which exhibit a strong enhancement of the mobility of electrons and holes: $\mu \gtrsim 100{,}000\ cm^2/Vs$, even up to room temperature (which is higher than ever reported before for a semiconducting material) [38].

2.5 QUANTUM INTERFERENCE

At room temperature, most electrical properties of macroscopic systems are well described by considering the electrons as classical particles. However, at low temperatures, the quantum mechanical wave properties of electrons come into play. Quantum interference of electronic waves gives rise to phenomena like weak localization, strong localization and the Aharonov-Bohm effect, which will be described in this section. Electronic transport in graphene is different than in usual materials, because graphene's conduction electrons have a chirality. This chirality can give rise to unique manifestations of these quantum interference phenomena, as will be explained in the final part of this section.

The quantum interference of electronic waves, that we consider here, occurs when electrons travel phase coherently through a diffusive conductor. In a diffusive medium, electrons experience many scattering events, which can be elastic or inelastic processes. Inelastic scatterers affect the energy of electrons and randomize their phase, while elastic scatterers only randomize the direction of motion. The mean free path of an electron, l_m, is defined as the average distance between elastic scatterers. This means that in the diffusive regime, the mean free path is smaller than the length of the conductor ($l_m < L$). Additionally, the phase coherence length, l_φ, is defined as the characteristic length scale on which the phase is conserved. For quantum interference effects to occur, the phase coherence length should be larger, or at least of the same order as the length of the conductor ($L \lesssim l_\varphi$). If, on the other hand, a conductor is much larger than the phase coherence length, the phase of the electrons is completely randomized and most phase coherent effects are suppressed.

2.5.1 WEAK LOCALIZATION

In the quantum diffusive regime ($l_m < L \lesssim l_\varphi$), electrons have a higher probability of backscattering than in the classical diffusive regime ($l_m, l_\varphi \ll L$). The enhanced backscattering is well understood by considering the interference of an electron with itself when it follows different trajectories (so-called Feynman paths) [15,22,42]. Figure 2.17a illustrates the presence of different trajectories between two points (r_1 and r_2) in a diffusive medium. If there are j possible trajectories, the probability to find an electron at point r_2 is the sum of the probability amplitudes associated to the different Feynman paths. For each path we write down the probability amplitude as $\psi_j = t_j e^{i\varphi_j}$. Hence, the total probability of an electron to move from point r_1 to point r_2 in a time interval t is

$$P(r_1, r_2, t) = |\psi|^2 = |\sum_j \psi_j|^2 = |\sum_j t_j e^{i\varphi_j}|^2 = \sum_j t_j^2 + \sum_{k \neq j} t_j t_k e^{i(\varphi_j - \varphi_k)} \tag{2.29}$$

The first term is simply the sum of the probabilities of the individual Feynman paths. The second term accounts for quantum interference between different paths.

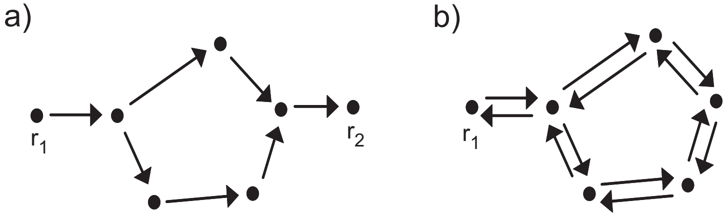

FIGURE 2.17: Schematic picture of uncorrelated trajectories contributing to forward scattering from r_1 to r_2 (a) and time reversed trajectories contributing to backward scattering (b).

In most cases, the Feynman paths are uncorrelated and the second term effectively averages out. Thus, for forward scattering from r_1 to r_2 we can write: $P_{fwd} = \sum_j t_j^2$.

However, if we consider the special case of backscattering ($r_1 = r_2$), the second term of eq. (2.29) does not completely average out. Figure 2.17b illustrates that for each trajectory j, there exists a trajectory j' which is the time reversed trajectory of j. Such pairs are called time reversal symmetric (TRS) trajectories and are fully correlated, because both trajectories correspond to exactly the same path, undergoing exactly the same scattering events (only the propagation directions are opposite). As a consequence, the partial wavefunctions of both Feynman paths are equal: $\psi_j = \psi_{j'}$ (yielding $t_j = t_{j'}$ and $\varphi_j = \varphi_{j'}$). For the total probability of backscattering we can write

$$P(r_1, r_1, t) = |\psi|^2 = \sum_j t_j^2 + \sum_{j,j'} t_j t_{j'} e^{i(\varphi_j - \varphi_{j'})} + \sum_{k \neq j,j'} t_j t_k e^{i(\varphi_j - \varphi_k)} \tag{2.30}$$

The difference between forward and backward scattering, is the second term containing the set of TRS trajectories. This term does not average out and equals $\sum_j t_j^2$. Consequently, the probability of backscattering is enhanced: $P_{back} = 2\sum_j t_j^2$ (note that P_{back} is twice as large as P_{fwd}). This quantum phenomenon of enhanced backscattering is called weak localization, because it is responsible for the fact that electrons *tend* to localize in a diffusive medium.

Time reversal symmetry can easily been broken by a magnetic field **B**. When an electron travels through a magnetic vector potential field **A** (defined by $\mathbf{B} = \nabla \times \mathbf{A}$), the electron acquires a phase:

$$\Delta\varphi = \frac{m}{\hbar}\int_{r1}^{r2} \mathbf{v} \cdot d\mathbf{r} - \frac{e}{\hbar}\int_{r1}^{r2} \mathbf{A} \cdot d\mathbf{r} \tag{2.31}$$

The first term is the usual phase evolution of an electron wave propagating from r_1 to r_2. The second term is an additional phase originating from the presence of a magnetic vector potential. If we compare two trajectories of length L, that are time reversed in the absence of the magnetic field, the acquired phase is

$$\Delta\varphi_j = k_F L - \frac{e}{\hbar}\oint_L \mathbf{A}\cdot d\mathbf{r}_j \tag{2.32}$$

for one of them, and

$$\Delta\varphi_{j'} = k_F L - \frac{e}{\hbar}\oint_L \mathbf{A}\cdot d\mathbf{r}_{j'} = k_F L + \frac{e}{\hbar}\oint_L \mathbf{A}\cdot d\mathbf{r}_j \tag{2.33}$$

for its time reversed partner (since $d\mathbf{r}_{j'} = -d\mathbf{r}_j$). This gives a phase difference between both trajectories equal to

$$|\Delta\varphi_j - \Delta\varphi_{j'}| = \frac{2e}{\hbar}\oint_L \mathbf{A}\cdot d\mathbf{r}_j = \frac{2e}{\hbar}\iint_S (\nabla\times\mathbf{A})dS = \frac{2e}{\hbar}\iint_S \mathbf{B}dS = \frac{2e}{\hbar}\Phi \tag{2.34}$$

where $\Phi = BS$ is the magnetic flux corresponding to the magnetic field penetrating the area S enclosed by the trajectories. This phase difference breaks the symmetry between the TRS trajectories. The large variation of areas S enclosed by the different time reversed pairs, results in a large variation of phase differences. Consequently, the second term in eq. (2.30), which accounts for an enhanced backscattering at zero magnetic field, averages out at high magnetic fields (i.e. $P_{back} = P_{fwd}$ at high field).

A signature of weak localization of electrons is a negative magnetoresistance. The enhanced backscattering at zero magnetic field results in a suppressed conductance (or an enhanced resistance). However, when a magnetic field is applied, the probability of backscattering decreases giving rise to an increase of the conductance. Weak localization is completely suppressed for typical magnetic fields $B \gtrsim h/(el_\varphi^2)$ [42]. The suppression of the conductance due to weak localization depends on the dimensionality of the system. The weak localization correction to the conductance is $\delta G \sim (e^2/h)(W/L)$ in a two-dimensional system ($l_\varphi < W$) [15].

2.5.2 QUANTUM INTERFERENCE IN A RING

Applying a magnetic field to a diffusive conductor does not only result in suppression of weak localization, it also gives rise to sample specific magnetoconductance fluctuations [15,22]. These fluctuations appear because of the interference of many different Feynman paths. Each path picks up a phase, dependent on the path length L and the vector potential $\mathbf{A}$. Since the paths are random, the superposition of all paths varies randomly as a function of magnetic field, yielding aperiodic magnetoconductance fluctuations ($\delta G \sim e^2/h$).

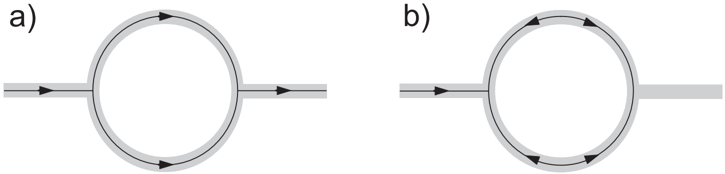

FIGURE 2.18: Schematic picture of different trajectories contributing to the AB-effect (a) and the AAS-effect (b).

These magnetoconductance oscillations become *periodic*, when the conductor has a ring-shaped structure [15,22,42]. Consider a ring with two leads (Figure 2.18a) and electrons traveling from the left to the right lead. The Feynman paths in the upper arm of the ring can be distinguished from the paths in the lower arm of the ring. In case of zero magnetic field ($\Phi = 0$), eq. (2.29) can be used to determine the probability to find an electron at the right lead. This probability changes if a magnetic field is applied ($\Phi \neq 0$), because the phase of each Feynman path is affected by the vector potential **A**. If the width of the arms of the ring is much smaller than the diameter of the ring, we can assume that all trajectories in the upper or lower arm acquire the same phase due to vector potential **A**. For trajectories in the upper arm of the ring (with length $L1$), this accumulated phase is

$$\Delta\varphi_1 = \frac{e}{\hbar}\int_{L1} \mathbf{A}\cdot d\mathbf{l}_1 \tag{2.35}$$

while in the lower arm of the ring (with length $L2$), it is

$$\Delta\varphi_2 = \frac{e}{\hbar}\int_{L2} \mathbf{A}\cdot d\mathbf{l}_2 \tag{2.36}$$

Effectively, this gives a phase difference between trajectories propagating in different arms

$$\Delta\varphi_1 - \Delta\varphi_2 = \frac{e}{\hbar}\oint_{L1+L2} \mathbf{A}\cdot d\mathbf{l} = \frac{e}{\hbar}\Phi \tag{2.37}$$

This result shows that the phase difference increases as a function of increasing magnetic field. As a consequence, the conductance oscillates as a function of Φ (or B) with a periodicity $\Delta\Phi = h/e$ (or $\Delta B = \frac{h}{eS}$ with S the area inside the ring). One often refers to these periodic conductance oscillations as to Aharonov-Bohm (AB) oscillations. We should note that also higher harmonic AB-oscillations can occur (e.g. the harmonic oscillations with periodicity $\Delta\Phi = h/2e$ due to interference of trajectories encircling the complete ring).

A second effect that gives rise to periodic conductance oscillations in a ring, is the Altshuler-Aronov-Spivak (AAS) effect [15,22,42]. The AAS-effect is directly related to weak localization. To understand the AAS-effect, we need to consider time reversal symmetric trajectories which encircle the complete ring in opposite directions (Figure 2.18b). According to eq. (2.30), the probability of backscattering $P(r_1, r_1, t)$ is enhanced when no magnetic field is penetrating the ring ($\Phi = 0$). However, when a magnetic field is present ($\Phi \neq 0$), each pair of time reversed pairs acquires a phase difference, which is

$$\Delta\varphi = \frac{2e}{\hbar}\oint_L \mathbf{A}\cdot d\mathbf{l} = \frac{2e}{\hbar}\Phi \tag{2.38}$$

Therefore, the conductance oscillates as a function of Φ (or B) with a periodicity of $\Delta\Phi = h/2e$ (or $\Delta B = \frac{h}{2eS}$). This is called the AAS-effect and occurs besides the AB-effect. Notice that the periodicity of the AAS-effect is equal to the periodicity of an harmonic of the AB-effect.

2.5.3 STRONG LOCALIZATION

In the weak localization regime, the backscattering of electrons is enhanced due to constructive interference of time reversal symmetric paths. In this regime, the electrons are not completely localized, but are still propagating diffusively. The electrons scatter inelastically to other states before they get localized. On the other hand, electrons can be completely localized in a strong disordered conductor. In this so-called strong localization regime, the electrons are locally confined and, effectively, the conductor becomes an insulator [43-45].

The length scale on which electrons are localized (i.e. the spatial distribution of the localized wave packets), is called the localization length ξ. In the weak localization regime, the electrons are not effectively localized, because the localization length is larger than the phase coherence length ($l_m < l_\varphi < \xi, L$). For strong localization to occur, the localization length should be smaller than the phase coherence length and the length of the conductor ($l_m \lesssim \xi < l_\varphi, L$). The crossover from weak to strong localization results in a metal to insulator transition. In the weak localization regime, the resistance depends linearly on the length of the conductor ($R \propto L$), but it depends exponentially on the length in the strong localized regime ($R \propto \exp(L/\xi)$) [22,45], at least in the zero temperature limit.

Although strongly localized electrons are locally confined, they can still contribute to the conduction. At finite temperatures, localized electrons are thermally activated to hop from one localized state to another [45]. If electrons hop to neighbouring sites, the transport mechanism is referred to as nearest neighbour hopping. In this transport regime, the temperature dependence of the resistance is thermally activated

$$R \propto \exp(\Delta_\xi / kT) \tag{2.39}$$

with Δ_ξ of the order of the level spacing between energy states in a localized domain. When Δ_ξ is large, it may be energetically more favourable for electrons to hop a larger distance to states with a closer energy level [45]. This is the variable range hopping regime, where the temperature dependence of the resistance is

$$R \propto \exp(T_0 / T)^{1/(d+1)} \tag{2.40}$$

with d the dimensionality of the system ($d = 1,2,3$) and T_0 a characteristic temperature related to the hopping energy (we should note that the exponent is $1/2$ if the Coulomb interactions between electrons at different sites are non-negligible, irrespective of the dimensionality of the system) [45].

In the strong localization regime, the electrons have an enhanced probability of backscattering due to time reversal symmetry. When this time reversal symmetry is broken by a magnetic field, the probability of backscattering decreases. Consequently, the localization length will increase (i.e. a larger distribution of the wave packet). The crossover to broken time reversal symmetry occurs at $B \gtrsim h/(e\xi^2)$. Contrary to the weak localization regime, there is no universal correction value (δG) of the conductance in the strong localization regime [46].

2.5.4 ANOMALOUS LOCALIZATION EFFECTS IN GRAPHENE

In graphene, the chiral nature of electrons gives rise to an additional phase: the Berry's phase (see §2.1). Electrons in conventional materials have no Berry's phase, but electrons in single layer graphene have a Berry's phase of π, which means that an electron wavefunction acquires a phase of π after a rotation of 2π in momentum space around a K-point (or a closed trajectory in real space, during which no intervalley scattering takes place). This additional phase can manifest itself in interference phenomena.

Since the band structure of graphene consists of two valleys, two different types of elastic scattering processes are possible: intervalley and intravalley scattering [47-51]. Intervalley scattering is scattering from a state in one valley to a state in the other valley (with a characteristic time τ_{inter}). This type of elastic scattering destroys the chirality, therefore the Berry's phase does not play a role if strong intervalley scattering is present. However, the chirality of electrons is conserved by intravalley scattering. Intravalley scattering is an elastic scattering process between states in a single valley (with a characteristic time τ_{intra}). If intravalley scattering is the dominant scattering mechanism ($\tau_{intra} \ll \tau_{inter}$), transport can be described effectively by only considering the single-valley Hamiltonian (eq. (2.14-2.15)).

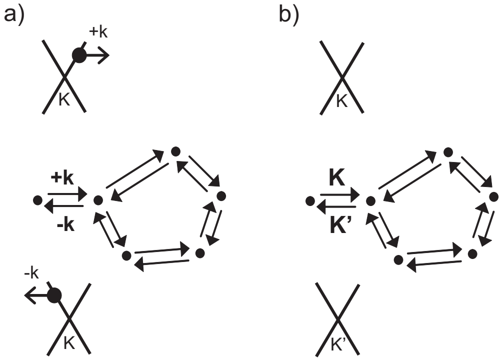

FIGURE 2.19: (a) If $\tau_{intra} \ll \tau_{inter}$, then intravalley scattering gives rise to backscattering trajectories (i.e. trajectories corresponding to states in a single valley). This picture shows that pairs of trajectories can be identified which are symmetric: the k and $-k$ states around the K point (or K' point) are effectively time reversal symmetric (note that the real time reversal symmetry is between the K and $-K$ states). This type of backscattering results in weak anti-localization in single-layer graphene. (b) If $\tau_{inter} \ll \tau_{intra}$, then intervalley scattering gives rise to backscattering trajectories (i.e. trajectories corresponding to states in both valleys). This picture shows that pairs of trajectories can be identified which are time reversal symmetric: the K and K' states are the real time reversal symmetric pairs. This type of backscattering gives rise to weak localization in single-layer graphene.

An interesting property of single-valley transport, is that the probability of backscattering is not enhanced as in usual materials, but is suppressed to zero [51]. This is a direct consequence of the single-valley Hamiltonian which has a symmetry (between k and $-k$) which is analogue to time reversal symmetry, but is not the real time reversal symmetry (which is between K and $-K$). Consequently, pairs of trajectories can be identified which are effectively time reversal symmetric (figure 2.19a). Since effective time reversal symmetric trajectories accumulate opposite Berry phases, the phase difference between each symmetric pair is π. Consequently, the reversed paths interfere destructively, resulting in a zero probability of backscattering (because the first two terms of eq. (2.30) cancel each other). The absence of backscattering leads to a suppression of resistance, which is called weak anti-localization.

If a magnetic field is present, the Aharonov-Bohm phases caused by the magnetic flux randomize the amplitudes of all trajectories, and the resistance is not suppressed anymore. This phenomenon gives rise to a positive magnetoresistance. Contrary to real time reversal symmetry, which can only be broken by a magnetic field, the effective time reversal symmetry can also be broken by long-range distortions of the lattice (e.g. dislocations), curvature of the graphene sheet (e.g. ripples), slowly varying random electric potentials (e.g. charged impurities close to the surface) and trigonal warping [50]. Such properties give rise to an effective gauge-field in the single-valley Hamiltonian, and therefore, similar to a magnetic field, break the effective time reversal symmetry. If the symmetry is already broken at zero field, a magnetic field will have no effect anymore, resulting in the absence of any (positive or negative) magnetoresistance effect.

On the other hand, weak localization is regularly observed in graphene. Weak localization occurs if intervalley scattering becomes stronger than intravalley scattering ($\tau_{inter} << \tau_{intra}$). Short-range potentials, like point defects and edge disorder, are the origin of intervalley scattering. When electrons scatter from one valley to the other, their chirality is destroyed and, consequently, the Berry's phase does not play a role in intervalley scattering processes. In this regime, the double-valley Hamiltonian needs to be considered in order to understand the electronic transport properties. In the double-valley Hamiltonian the K and K' states are the real time reversal symmetric pairs (figure 2.19b). Their symmetry is robust and can only be broken by a magnetic field. As in conventional materials, backscattering is enhanced at zero magnetic field, but is suppressed at high magnetic fields, which gives rise to a negative magnetoresistance in the regime of intervalley scattering.

When intervalley scattering becomes very strong, weak localization can turn into strong localization. Strong localization is theoretically predicted in disordered graphene nanoribbons [52-56]. The presence of strong disorder in these quasi-one-dimensional systems yields a high intervalley scattering rate and, therefore, a smaller mean free path l_m than in two-dimensional graphene. Close to the charge neutrality point, it is expected that the localization length is of the same order as the mean free path [52]. Consequently, at low charge density, the regime of strong localization will be accessible if $l_m \lesssim \xi < l_\varphi, L$. A crossover from weak to strong localization will give rise to a transition from diffusive to hopping transport [56].

In this section, we only discussed localization effects in single-layer graphene, but a similar discussion can be done for bilayer graphene, because bilayer graphene also has two valleys and supports chiral electrons. However, an important difference is that chiral electrons in bilayer graphene have a Berry's phase of 2π. In the single-valley transport regime ($\tau_{intra} << \tau_{inter}$), a Berry's phase of 2π gives rise to an enhanced backscattering. As a consequence, intravalley scattering results in weak localization (contrary to weak anti-localization in single-layer graphene). So, differently from single layers, weak anti-localization is not expected to occur in bilayers [51].

2.6 ANDREEV REFLECTION AND SUPERCURRENT

Many metals turn into superconductors below a critical temperature T_c, which is material dependent [57,58]. Below T_c, the electrons close to E_F form Cooper pairs, which consist of electrons of opposite momentum and spin. These Cooper pairs are condensed into a collective state $\psi(r) = |\psi(r)|e^{i\phi(r)}$ at E_F (with $\phi(r)$ the phase of the superconducting state). As a consequence, the normal density of states vanishes in the range $[E_F - \Delta, E_F + \Delta]$ and an energy gap appears at E_F. Remarkably, the electric current, carried by the Cooper pairs, is dissipationless. Therefore, the resistance of a superconductor drops to zero below its critical temperature.

In this section, we will consider metals which are contacted to a superconductor. We will show that a special type of electron reflection occurs at a superconductor-metal interface, the so-called Andreev reflection. If a metal is sandwiched between two closely spaced superconducting contacts, the current though the metal can also be dissipationless due to the Josephson effect. Finally, we will consider electronic transport in superconductor-graphene-superconductor junctions.

2.6.1 ANDREEV REFLECTION

In a metal-superconductor junction, electron transport occurs in a unique way. A metal has a continuous density of states at the Fermi level, while a superconductor has an energy gap at E_F. If an electron with energy $E_F + \varepsilon$ travels through a metal and arrives at the interface, it will meet the superconducting gap if $\varepsilon < \Delta$ (figure 2.20). To enter the superconductor, it needs to form a Cooper pair with another electron. Therefore, a second electron is extracted from the metal, which has opposite momentum and spin. Since charge needs to be conserved, this process leaves a hole in the metal. The process of an incoming electron which is reflected as a hole in the metal, is called Andreev reflection [42,58].

The initial electron with wavevector $k_e^{(1)}$ forms a Cooper pair with a second electron which has an opposite wavevector, $k_e^{(2)} = -k_e^{(1)}$. Since the second electron leaves a hole in the metal, the wavevector of the hole is $k_h = -k_e^{(2)} = k_e^{(1)}$. Although the wavevectors of the initial electron and the reflected hole are identical, their velocities are opposite, because the velocity and wavevector are parallel (antiparallel) for electrons (holes). Consequently, the reflected hole retraces the path of the initial electron. This is called retroreflection.

However, we should realize that $k_h \neq k_e^{(1)}$ if $\varepsilon \neq 0$. This can be understood by considering the energy states of the particles involved in the process. Before and after Andreev reflection, the values of the total energy are $E_{initial} = E_e^{(1)} + E_e^{(2)} + E_h = E_F + \varepsilon + 2E_h$ and $E_{final} = 2E_e^{(Cooper)} + E_h = 2E_F + E_h$. Since energy needs to be conserved, the energy of the hole is $E_h = E_F - \varepsilon$, and consequently, $k_h < k_e^{(1)}$ if $\varepsilon > 0$. This difference in momentum, that is absorbed by the Cooper pair, gives rise to a phase difference between the trajectories of the incoming electron and the retroreflected hole. They lose their coherence if the phase difference becomes $\Delta\varphi \gtrsim \pi$. Therefore, by considering all possible Andreev reflection processes (0 <

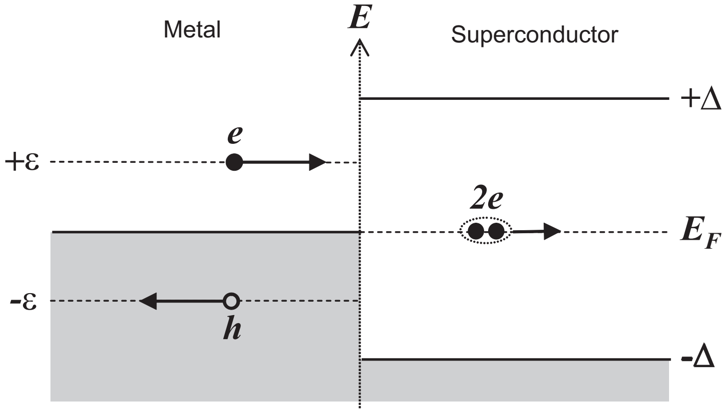

FIGURE 2.20: The process of Andreev reflection at a metal-superconductor interface. Since a Cooper pair is formed in the superconductor, the incident electron is reflected as a hole.

$\varepsilon < \Delta$), the superconducting phase coherence length can be determined, which is $\xi_0 = \frac{\hbar v_F}{\pi\Delta}$ in a ballistic metal and $\xi = \sqrt{\xi_0 l_m}$ in a diffusive metal [59].

2.6.2 JOSEPHSON SUPERCURRENT

If a normal metal is contacted by two closely spaced superconducting electrodes, forming a so-called Josephson junction, the metal can support dissipationless currents [42,58]. These proximity induced supercurrents occur in the absence of a driving voltage. This phenomenon is called the Josephson effect. If the current is smaller than a critical current I_c, there is no energy disipation (i.e. $V = 0$). On the other hand, if $I > I_c$, a dissipating current flows through the metal ($V \neq 0$). The occurrence of supercurrents for $I < I_c$ can be understood by considering multiple coherent Andreev reflections at both metal-superconductor interfaces.

Suppose an electron with energy $E_F + \varepsilon$ (and $\varepsilon < \Delta$) is travelling in the metal towards the right superconductor (figure 2.21). At the interface, the electron will enter the superconductor and a hole is Andreev reflected (with an energy $E_F - \varepsilon$). When this hole arrives at the interface with the left superconductor, it will enter the superconductor and return an Andreev reflected electron. This electron has the same state as the original electron ($E_F + \varepsilon$) and, therefore, both will interfere. Effectively, this process of multiple Andreev reflections transfers Cooper pair from one superconductor to the other. Moreover, this process gives rise to quantized bound states in the metal and no energy dissipation occurs. This results in a supercurrent I_s, which depends on the phase difference $\Delta\varphi$ between both superconductors: $I_s = I_c \sin\Delta\varphi$ [42,58]. If the spacing between the superconductors is

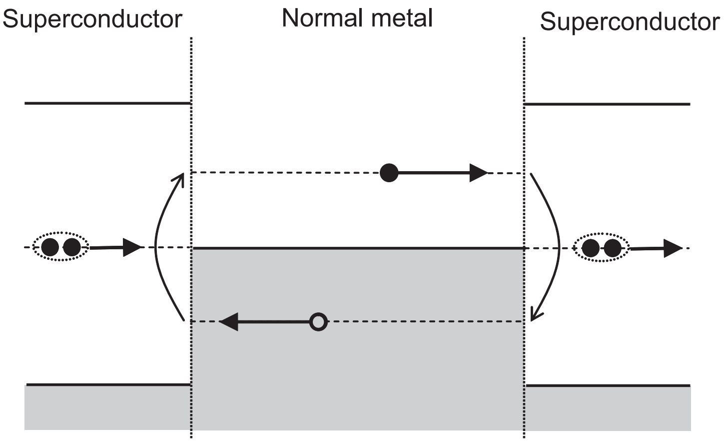

FIGURE 2.21: Schematic picture of the mechanism of the Josephson effect, which gives rise to dissipationless supercurrent. Multiple Andreev reflections yield bound states in the metal, through which Cooper pairs are transferred from the left to the right superconductor.

smaller than the superconducting phase coherence length ($L < \xi$), the critical current is $I_c = Ne\Delta/\hbar$ (with N the number of superconducting channels, including the degeneracies) [59].

While multiple Andreev reflections (MAR) give rise to bound states for $I < I_c$, they result in subgap features if $I > I_c$ [58]. If $I > I_c$, a dissipative current flows through the normal metal. This results in a voltage drop over the metal ($V > 0$). If $V > 2\Delta/e$, two different kind of paths contribute to the electric current through the metal: paths without AR and paths with single AR (figure 2.22a). However, if $V < 2\Delta/e$, paths without AR cannot occur anymore and paths with double AR arise (figure 2.22b). As a consequence, the transmission through the metal changes yielding a feature in the I-V characteristic at $V = 2\Delta/e$. More of these features appear at $V_n = 2\Delta/ne$ where paths with $(n+1)$-fold AR appear and paths with $(n-1)$-fold AR disappear (note that $V \rightarrow 0$ if $I \rightarrow I_c$, because $V = 0$ if $I < I_c$).

2.6.3 ANDREEV REFLECTION AND SUPERCURRENT IN GRAPHENE

As we have shown in previous sections, Andreev reflections are intraband processes: the electron and its Andreev reflected hole are both in the conduction band. Interband Andreev reflections cannot occur in usual metals. However, in graphene intraband as well as interband Andreev reflections can occur, dependent on the position of the Fermi level. As a consequence two different regimes are distinguished in graphene [60].

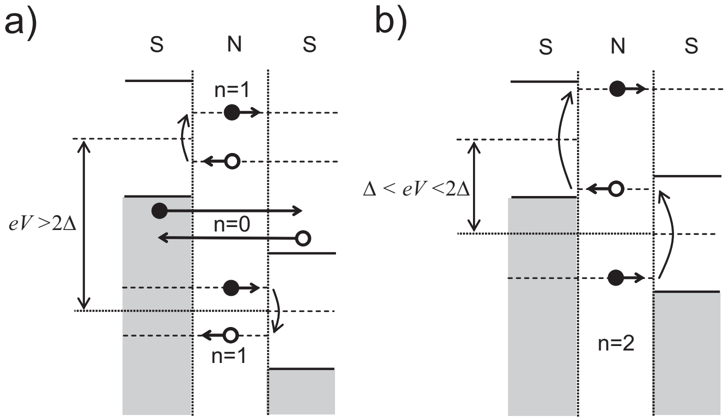

FIGURE 2.22: Multiple Andreev reflections which contribute to the normal current through the metal ($I > I_c$). (a) If $V > 2\Delta/e$, then transmissions without ($n = 0$) and with a single Andreev reflection ($n = 1$) contribute to the current. If $\Delta/e < V < 2\Delta/e$, then transmissions without Andreev reflection disappear and transmissions with two-fold Andreev reflection appear ($n = 2$).

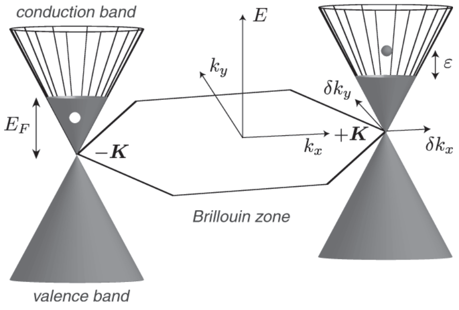

FIGURE 2.23: Andreev reflection gives rise to coupling of both valleys in graphene. The incident electron in one valley is related to the Andreev reflected hole in the other valley [60].

Consider an electron with wavevector k which travels in a graphene sheet towards a superconductor. When it arrives at the interface, it enters the superconductor and forms a Cooper pair with a second electron with wavevector $-k$. Since both electrons have opposite wavevectors, they come from two different valleys of graphene, K and K' (figure 2.23). As a consequence, Andreev reflection processes connect both valleys of graphene. If the intial electron is in the conduction band with energy $E_F + \varepsilon$ and $\varepsilon < E_F$, then the Andreev reflected hole with energy $E_F - \varepsilon$ will also be in the conduction band (figure 2.24a). The original electron moves towards the interface, while the hole moves away from the interface, therefore v_x should change sign. Furthermore, k_y should be conserved after reflection. Figure 2.24a shows that under these conditions, v_x as well as v_y change sign (i.e. $v_x^h = -v_x^e$ and $v_y^h = -v_y^e$). Consequently, the reflected hole retraces the path of the original electron . This result shows that intraband Andreev reflection in graphene leads to retroreflection (as in usual metals).

A different reflection process occurs if the initial electron has an energy $E_F + \varepsilon$ with $E_F < \varepsilon$ (and both E_F and ε smaller than Δ). In this case, the reflected hole with energy $E_F - \varepsilon$ will be in the valence band (figure 2.24b). For Andreev reflection to occur, v_x needs to change sign and k_y needs to be conserved. Since the velocity of a valence band electron is parallel to its wavevector, the velocity parallel to the interface does not change sign ($v_x^h = -v_x^e$ and $v_y^h = v_y^e$). Thus, interband Andreev reflection leads to specular reflection, which is a unique property of graphene [60].

Not only Andreev reflection is different close to the Dirac point, but also Josephson supercurrents exhibit differences with respect to usual materials. In short ballistic graphene Josephson junctions ($L < \xi$), the critical current is $I_c \cong \frac{e\Delta}{\hbar} W/\lambda_F$ if $\lambda_F < L$ (which is the high doping regime, $E_F > \hbar v_F/L$). On the other hand, the critical current is $I_c \cong \frac{e\Delta}{\hbar} W/L$ if $\lambda_F > L$ (which is in the vicinity of the Dirac point, $E_F < \hbar v_F/L$) [60,61]. This result shows that the critical current is length independent at high densities, but is length dependent close to the Dirac point. The length dependence close to the Dirac point is remarkably different from usual materials, in which the critical current is length independent if $L < \xi$.

2.7 PREPARATION AND IDENTIFICATION OF GRAPHENE

In this section, we will discuss graphene from a more practical point of view. In the first part, the most widely used preparation techniques of graphene will be discussed: from mechanical exfoliation to growing graphene. Then, in the second part, several methods for graphene identification are described, because after graphene preparation, the number of layers needs to be determined: from single-layer to n-layer graphene.

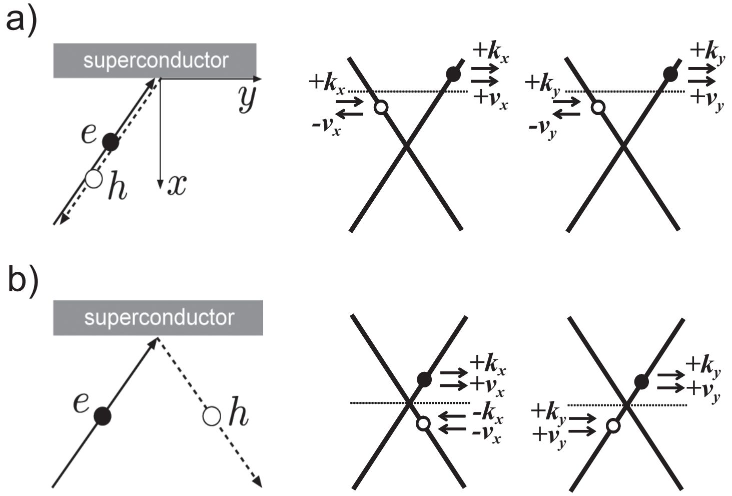

FIGURE 2.24: Andreev retroreflection (a) and specular Andreev reflection (b) in graphene (adapted from [60]). Additionally, k_x and k_y of the incident electron and the reflected hole are shown for both reflection processes.

2.7.1 HOW TO PREPARE GRAPHENE

Until recently, it was widely believed that two-dimensional crystals, like a single atomic layer of graphite, cannot exist. However, Andre Geim and Kostya Novoselov from Manchester University strongly believed that it should be possible to remove a single layer of graphite from a larger three-dimensional crystal. They used normal adhesive tape to peel graphitic layers from a piece of graphite. Subsequently, they transferred the graphitic flakes to a Si/SiO$_2$ substrate (simply by pressing the tape with peeled graphite flakes on the SiO$_2$ side of the substrate). Most susprisingly, they succeeded in transferring single atomic layers of graphite [62,63]. Their experimental discovery of graphene in 2004 opened a new branch of physics [9].

After this great discovery, many research groups, like our group in Delft, started to mechanically exfoliate graphite to prepare graphene flakes on a Si/SiO$_2$ substrate. After graphene flakes were found on a substrate, electronic graphene devices could be made by contacting the flakes with metal electrodes (figure 2.25; see appendix for technical details). For preparing graphene flakes, different types of graphite are available, ranging from natural graphite from different parts of the world (e.g. North Korea, United States, China, Madagascar, Sri Lanka, India) to synthetic graphite produced at companies (i.e. HOPG: highly ordered pyrolytic graphite). Dependent on the type of graphite that was used, different electron

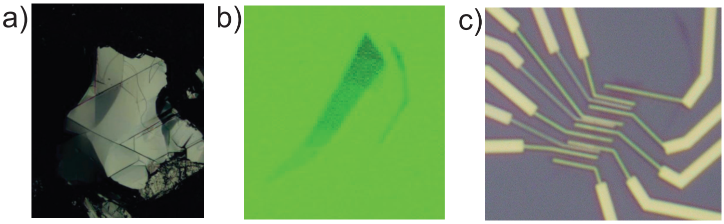

FIGURE 2.25: Optical pictures of (a) graphite, (b) graphene and (c) a typical graphene device.

mobilities were measured in graphene devices, indicating a variation of the quality of graphene flakes (possibly due to a different amount and type of disorder). However, a systematic quantitative study of the different qualities of graphene has never been done yet.

Although mechanical exfoliation of graphite by using adhesive tape is a suitable technique for preparing high-quality graphene flakes in research labs, this technique is not satisfying the requirements for massive production of graphene in industrial environments. Therefore, there is a need for a production technique which enables control of the size and quality of graphene crystals. Already before the experimental discovery of graphene in 2004, researchers were able to grow thin graphite layers on top of a substrate [9,64]. More recently, many researchers succeeded in growing single-layer graphene epitaxially on several substrates, and even to transfer these graphene layers to different substrates [65]. The most promising growing techniques so far are thermal decomposition of silicon-carbide [64] and chemical vapour deposition of graphene on nickel or other transition metal substrates [66].

2.7.2 HOW TO IDENTIFY GRAPHENE

Immediately after the discovery of graphene, there were not many reliable techniques to distinghuish single-layer graphene from multi-layers. In case the flakes were contacted by metal electrodes, the quantum Hall effect was often used for identification, because single-layer graphene exhibits a unique sequence of quantum Hall conductance steps (see figure 2.15) [9]. Although this method was successfully used to identify single-layer graphene, there was a need for alternative techniques which are less time-consuming.

Usually, an AFM (atomic force microscope) is used to determine atomic scale step heights of materials. Also, the step height from single-layer to n-layer graphene can be determined accurately by an AFM [67]. AFM-measurements have shown that the step height between different layers is a multiple of ~ 0.35 nm, which corresponds to the interlayer distance in graphite. However, the thickness of a single-

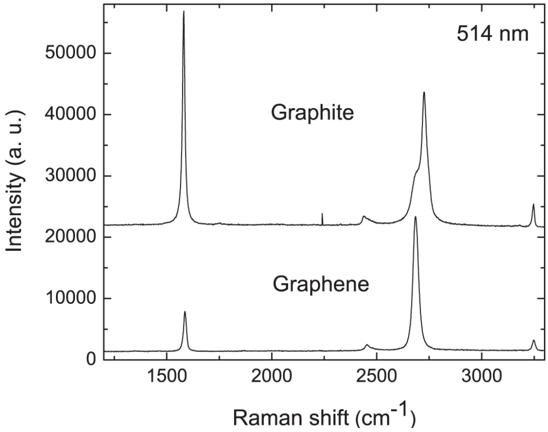

FIGURE 2.26: The Raman spectrum of graphite and graphene, showing the G-peak and the D'-peak as the most prominent features, which can be used to identify single-layer graphene [68].

layer of graphene with respect to the underlying substrate appeared to be larger (instead of a thickness of ~ 0.35 nm, values varying between 0.5 and 1 nm were regularly obtained for graphene on SiO_2). Different explanations are given for this deviation (for instance, the attraction force between the AFM-tip and graphene may differ from the force between tip and substrate, or there may be water or something else between graphene and the substrate). As a consequence, AFM is not a good technique to determine the thickness of single-layer and few-layer graphenes.

A reliable technique, which is often used to identify single-layer graphene, is Raman spectroscopy [67-69]. The Raman spectrum appears to be sensitive to the number of graphene layers. The most prominent features of the Raman spectra of graphene and graphite are the G-peak, around 1580 cm^{-1}, and the D'-peak, around 2700 cm^{-1} (figure 2.26). Since the intensities and positions of these peaks are related to the electronic structure, these peaks depend on the number of graphene layers. With respect to the Raman spectrum of graphite, the G peak of single-layer graphene is shifted upwards from ~ 1582 to ~ 1587 cm^{-1} [67], the intensity of the G-peak is decreased while the intensity of the D'-peak remains almost constant [67,69] and the FWHM-value (full width at half maximum) of the D' peak of single-layer graphene is changed from ~ 60 to ~ 30 cm^{-1} [69]. Because of these features, Raman spectroscopy is a useful technique to identify single-layer graphene (and even n-layer graphene, for $n \lesssim 5$) [67-69].

A good alternative for identification of graphene, is to make use of its visibility in an optical microscope. Graphene is visible on a Si/SiO_2 substrate, because the

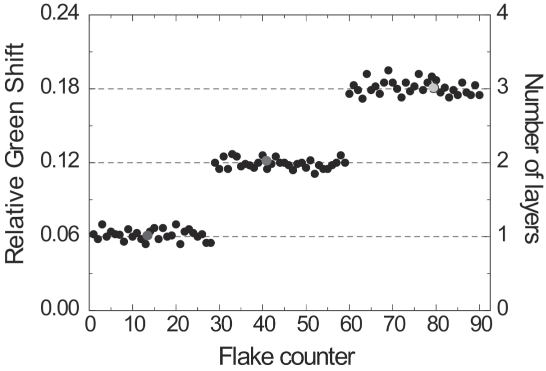

FIGURE 2.27: The relative green shift (RGS) of single-layer, bilayer and trilayer graphene with respect to a silicon substrate with 285 nm SiO_2 [72]. The flake counter shows for how many flakes the RGS-value is determined (each point in the figure represents the RGS-value of a flake).

intensity of reflected light from this substrate changes slightly if a graphene flake is present [70]. The optical wavelengths at which the difference in reflectivity between the flake and the substrate is maximum, depends on the thickness of the SiO_2 layer. For example, graphene on a 285 nm SiO_2 layer has a maximum visibility at wavelengths in the green spectrum ($\lambda \sim 550$ nm). To quantify the visibility of graphene, the intensities of the reflected green light from the graphene flake as well as the surrounding substrate need to be determined. This can be done by extracting the green component of the RGB-value from a digital color picture of the flake (G_f) and the substrate (G_s) [71,72]. Subsequently, the so-called relative green shift (RGS) can be calculated, $RGS = (G_s - G_f)/G_s$, which is a measure of the contrast. Figure 2.27 shows the determined RGS-values of a large number of single-layer, bilayer and trilayer graphene flakes on a substrate with 285 nm SiO_2 [72]. This figure clearly indicates that this optical contrast method is a reliable technique to identify the thickness of graphene flakes (up to at least three layers).

2.8 REFERENCES

1. R. Saito, G. Dresselhaus, M. S. Dresselhaus, Physical Properties of Carbon Nanotubes (Imperial College Press, London, UK, 1998).
2. P. R. Wallace, The band theory of graphite, Phys. Rev. 71 (9), 622-634 (1947).
3. J. Gonzalez, F. Guinea, M. A. H. Vozmediano, The electronic spectrum of fullerenes from the Dirac equation, Nucl. Phys. B406, 771-794 (1993).
4. C. Schönenberger, Bandstructure of graphene and carbon nanotubes: An exercise in condensed matter physics, Available at http://pages.unibas.ch/phys-meso

(April 2000).
5. A. H. Castro Neto, F. Guinea, N. M. R. Peres, K. S. Novoselov, A. K. Geim, The electronic properties of graphene, Rev. Mod. Phys. 81, 109-162 (2009).
6. J. C. Slonczewski, P. R. Weiss, Band structure of graphite, Phys. Rev. 109 (2), 272-279 (1958).
7. D. P. DiVincenzo, E. J. Mele, Self-consistent effective-mass theory for intralayer screening in graphite intercalation compounds, Phys. Rev. B 29 (4), 1685-1694 (1984).
8. P. L. McEuen, M. Bockrath, D. H. Cobden, Y.-G. Yoon, S. G. Louie, Disorder, pseudospins, and backscattering in carbon nanotubes, Phys. Rev. Lett. 83 (24), 5098-5101 (1999).
9. A. K. Geim, K. S. Novoselov, The rise of graphene, Nature Materials 6, 183-191 (2007).
10. E. McCann, V. I. Fal'ko, Landau-level degeneracy and quantum Hall effect in a graphite bilayer, Phys. Rev. Lett. 96, 086805 (2006).
11. E. McCann, Asymmetry gap in the electronic band structure of bilayer graphene, Phys. Rev. B 74, 161403 (2006).
12. K. S. Novoselov et al., Unconventional quantum Hall effect and Berry's phase of 2π in bilayer graphene, Nature Physics 2, 177-180 (2006).
13. M. S. Dresselhaus, G. Dresselhaus, Intercalation compounds of graphite, Adv. Phys. 51 (1), 1-186 (2002).
14. M. Koshino, E. McCann, Gate-induced interlayer asymmetry in ABA-stacked trilayer graphene, Phys. Rev. B 79, 125443 (2009).
15. C. W. J. Beenakker, H. van Houten, Quantum transport in semiconductor nanostructures, Solid State Physics 44, 1-228 (1991).
16. C. Berger et al., Electronic confinement and coherence in patterned epitaxial graphene, Science 312, 1191-1196 (2006).
17. K. Nakada, M. Fujita, G. Dresselhaus, M. S. Dresselhaus, Edge state in graphene ribbons: Nanometer size effect and edge shape dependence, Phys. Rev. B 54 (24), 17954 (1996).
18. L. Brey, H. A. Fertig, Electronic states of graphene nanoribbons studied with the Dirac equation, Phys. Rev. B 73, 235411 (2006).
19. Y. -W. Son, M. L. Cohen, S. G. Louie, Energy gaps in graphene nanoribbons, Phys. Rev. Lett. 97, 216803 (2006).
20. M. Fujita, K. Wakabayashi, K. Nakada, K. Kusakabe, Peculiar localized state at zigzag graphite edge, Jour. Phys. Soc. Japan 65 (7), 1920-1923 (1996).
21. Y. -W. Son, M. L. Cohen, S. G. Louie, Half-metallic graphene nanoribbons, Nature 444, 347 (2006).
22. S. Datta, Electronic Transport in Mesoscopic Systems (Cambridge Universiy Press, Cambridge, UK, 1995).

23. K. S. Novoselov et al., Two-dimensional gas of massless Dirac fermions in graphene, Nature 438, 197-200 (2005).
24. Y. Zhang, Y. -W. Tan, H. L. Stormer, P. Kim, Experimental observation of the quantum Hall effect and Berry's phase in graphene, Nature 438, 201-204 (2005).
25. M. I. Katsnelson, Zitterbewegung, chirality, and minimal conductivity in graphene, Eur. Phys. Jour. B 51, 157-160 (2006).
26. J. Tworzydlo, B. Trauzettel, M. Titov, A. Rycerz, C. W. J. Beenakker, Sub-poissonian shot noise in graphene, Phys. Rev. Let. 96, 246802 (2006).
27. F. Miao et al., Phase-coherent transport in graphene quantum billiards, Science 317, 1530-1533 (2007).
28. R. Danneau et al., Shot noise in ballistic graphene, Phys. Rev. Let. 100, 196802 (2008).
29. Y. -W. Tan et al., Measurement of scattering rate and minimum conductivity in graphene, Phys. Rev. Let. 99, 246803 (2007).
30. S. Adam, E. H. Hwang, E. Rossi, S. Das Sarma, Theory of charged impurity scattering in two-dimensional graphene, Solid State Comm. 149, 1072-1079 (2009).
31. J. Martin et al, Observation of electron-hole puddles in graphene using a scanning single-electron transistor, Nature Physics 4, 144-148 (2008).
32. J. -H. Chen et al., Charged-impurity scattering in graphene, Nat. Phys. 4, 377-381 (2008).
33. J. -H. Chen et al., Diffusive charge transport in graphene on SiO_2, Solid State Com. 149, 1080-1086 (2009).
34. S. Adam, E. H. Hwang, V. M. Galitski, S. Das Sarma, A self-consistent theory for graphene transport, PNAS 104 (47), 18392-18397 (2007).
35. S. V. Morozov et al., Giant intrinsic carrier mobilities in graphene and its bilayer, Phys. Rev. Let. 100, 016602 (2008).
36. L. A. Ponomarenko et al., Effect of a high-κ environment on charge carrier mobility in graphene, Phys. Rev. Let. 102, 206603 (2009).
37. X. Du, I. Skachko, A. Barker, E. Y. Andrei, Approaching ballistic transport in suspended graphene, Nat. Nanotech. 3, 491-495 (2008).
38. K. I. Bolotin et al., Ultrahigh electron mobility in suspended graphene, Solid State Com. 146, 351-355 (2008).
39. K. I. Bolotin, K. J. Sikes, J. Hone, H. L. Stormer, P. Kim, Temperature-dependent transport in suspended graphene, Phys. Rev. Let. 101, 096802 (2008).
40. S. Fratini, F. Guinea, Substrate-limited electron dynamics in graphene, Phys. Rev. B 77, 195415 (2008).
41. J. -H. Chen, C. Jang, S. Xiao, M. Ishigami, M. S. Fuhrer, Intrinsic and extrinsic performance limits of graphene devices on SiO_2, Nat. Nanotech. 3, 206-209 (2008).
42. C. Harmans, Mesoscopic physics - an introduction, Lecture notes Delft University of Technology (NS3521TU, form. TN3853), 1-230 (2003).

43. P. W. Anderson, Absence of diffusion in certain random lattices, Phys. Rev. 109, 1492-1505 (1958).

44. B. I. Shklovskii, A. L. Efros, Electronic properties of doped semiconductors (Springer, Heidelberg, Germany, 1984).

45. Y. Imry, Introduction to mesoscopic physics (Oxford Univ. Press, Oxford, UK, 1997).

46. M. E. Gershenson, Y. B. Khavin, A. G. Mikhalchuk, H. M. Bozler, A. L. Bogdanov, Crossover from weak to strong localization in quasi-one-dimensional conductors, Phys. Rev. Lett. 79 (4), 725-728 (1997).

47. S. V. Morozov et al., Strong suppression of weak localization in graphene, Phys. Rev. Let. 97, 016801 (2006).

48. D. V. Khveshchenko, Electron localization properties in graphene, Phys. Rev. Let. 97, 036802 (2006).

49. E. McCann et al., Weak-localization magnetoresistance and valley symmetry in graphene, Phys. Rev. Let. 97, 146805 (2006).

50. A. F. Morpurgo, F. Guinea, Intervalley scattering, long-range disorder, and effective time-reversal symmetry breaking in graphene, Phys. Rev. Let. 97, 196804 (2006).

51. K. Kechedzhi et al., Weak localization in monolayer and bilayer graphene, Eur. Phys. Jour. 148, 39-54 (2007).

52. D. Gunlycke, D. A. Areshkin, C. T. White, Semiconducting graphene nanostrips with edge disorder, App. Phys. Lett. 90, 142104 (2007).

53. A. Lherbier, B. Biel, Y. -M. Niquet, S. Roche, Transport length scales in disordered graphene-based materials: Strong localization regimes and dimensionality effects, Phys. Rev. Lett. 100, 036803 (2008).

54. M. Evaldsson, I. V. Zozoulenko, H. Xu, T. Heinzel, Edge disorder induced Anderson localization and conduction gap in graphene nanoribbons, Phys. Rev. B 78, 161407 (2008).

55. E. R. Mucciolo, A. H. Castro-Neto, C. H. Lewenkopf, Conductance quantization and transport gap in disordered graphene nanoribbons, Phys. Rev. B 79, 075407 (2009).

56. I. Martin, Y. M. Blanter, Transport in disordered graphene nanoribbons, Phys. Rev. B 79, 235132 (2009).

57. C. Kittel, Introduction to solid state physics (John Wiley & Sons, New York, USA, 1996).

58. M. Tinkham, Introduction to superconductivity (Dover Publications, New York, USA, 2004).

59. C. W. J. Beenakker, Three "universal" mesoscopic Josephson effects (published in: "Transport Phenomena in Mesoscopic Systems", ed. H. Fukuyama, T. Ando, Springer, Berlin, Germany, 1992).

60. C. W. J. Beenakker, Colloquium: Andreev reflection and Klein tunneling in graphene, Rev. Mod. Phys. 80, 1337-1354 (2008).
61. M. Titov, C. W. J. Beenakker, Josephson effect in ballistic graphene, Phys. Rev. B 74, 041401 (2006).
62. K. S. Novoselov et al., Electric field effect in atomically thin carbon films, Science 306, 666-669 (2004).
63. K. S. Novoselov et al., Two-dimensional atomic crystals, PNAS 102 (30), 10451-10453 (2005).
64. Th. Seyller et al., Epitaxial graphene: a new material, Phys. Stat. Sol. B 245 (7), 1436-1446 (2008).
65. A. K. Geim, Graphene: Status and prospects, Science 324, 1530-1534 (2009).
66. K. S. Kim et al., Large-scale pattern growth of graphene films for stretchable transparent electrodes, Nature 457, 706-710 (2009).
67. A. Gupta, G. Chen, P. Joshi, S. Tadigadapa, P. C. Eklund, Raman scattering from high-frequency phonons in supported n-graphene layer films, Nano Lett. 6 (12), 2667-2673 (2006).
68. A. C. Ferrari et al., Raman spectrum of graphene and graphene layers, Phys. Rev. Lett. 97, 187401 (2006).
69. D. Graf et al., Spatially resolved Raman spectroscopy of single- and few-layer graphene, Nano Lett. 7 (2), 238-242 (2007).
70. P. Blake et al., Making graphene visible, Appl. Phys. Lett. 91, 063124 (2007).
71. J. B. Oostinga, H. B. Heersche, X. Liu, A. F. Morpurgo, L. M. K. Vandersypen, Gate-induced insulating state in bilayer graphene devices, Nature Materials, 7 (2), 151-157 (2008).
72. M. F. Craciun, S. Russo, M. Yamamoto, J. B. Oostinga, A. F. Morpurgo, S. Tarucha, Trilayer graphene is a semimetal with gate-tunable band overlap, Nature Nanotechnology, 4 (6), 383-388 (2009).

3

GATE-TUNABLE BANDGAP IN BILAYER GRAPHENE

The potential of graphene-based materials consisting of one or a few layers of graphite for integrated electronics originates from the large room-temperature carrier mobility in these systems (∼10,000 cm^2/Vs). However, the realization of electronic devices such as field-effect transistors will require controlling and even switching off the electrical conductivity by means of gate electrodes, which is made difficult by the absence of a bandgap in the intrinsic material. Here, we demonstrate the controlled induction of an insulating state – with large suppression of the conductivity – in bilayer graphene, by using a double-gate device configuration that enables an electric field to be applied perpendicular to the plane. The dependence of the resistance on temperature and electric field, and the absence of any effect in a single-layer device, strongly suggest that the gate-induced insulating state originates from the recently predicted opening of a bandgap between valence and conduction bands.

The contents of this chapter have been published in *Nature Materials*:
J. B. Oostinga, H. B. Heersche, X. Liu, A. F. Morpurgo, L. M. K. Vandersypen, *Gate-induced insulating state in bilayer graphene devices.* Nature Materials **7** (2), 151-157 (2008).

3.1 INTRODUCTION

Graphene systems, consisting of one or a few crystalline monolayers of carbon atoms, stand out because of their unusual electronic properties and their potential for applications in nano-electronics [1-5]. Carrier mobility values as high as 10,000 cm^2/Vs at room temperature − ten times higher than in silicon − are routinely obtained in these materials, without the need for sophisticated preparation techniques [1]. Both the high mobility and the possibility of low-cost mass production provide a strong drive to explore the use of graphene for future high-speed integrated electronic circuits. To develop such 'graphene-based electronics', however, several problems need to be overcome. Perhaps the most important obstacle is the absence of an energy gap separating the valence and conduction bands of graphene − graphene is a zero-gap semiconductor [6]. As a consequence, electrical conduction cannot be switched off using control voltages [7], which is essential for the operation of conventional transistors. It was recently shown that conduction can be switched off by patterning single-layer graphene into narrow ribbons [8]. Here, we demonstrate that we can produce an insulating state and switch off electrical conduction in a bilayer graphene device, simply by applying control voltages to two on-chip gate electrodes.

3.2 THE LOW-ENERGY BANDSTRUCTURE OF SINGLE- AND BILAYER GRAPHENE

Our strategy is motivated by recent theoretical work that discusses how a bandgap can be opened in single- and bilayer graphene [9,10]. To understand the physical mechanisms underlying these predictions, we consider the basic electronic properties of graphene-based materials in some detail. Monolayer graphene has a honeycomb lattice structure with a unit cell consisting of two atoms − normally referred to as A and B atoms (Fig. 3.1a). The Hamiltonian that describes the electronic properties of graphene near the Fermi level can be approximated as [6,11]

$$H = \begin{pmatrix} \Delta & \hbar v_F(k_x - ik_y) \\ \hbar v_F(k_x + ik_y) & -\Delta \end{pmatrix}, \tag{3.1}$$

where k is the momentum and v_F is the Fermi velocity. This operator acts on spinors $\psi = (\varphi_A, \varphi_B)^T$, where φ_A and φ_B are the amplitudes of the wavefunction on sublattices A and B, and Δ is the on-site energy difference between the two sublattices. Normally $\Delta = 0$ and this Hamiltonian results in the Dirac-like linear dispersion relation $E = \pm\hbar v_F|k|$ (Fig. 3.1a). The positive and negative solutions, which correspond to conduction and valence bands respectively, meet at $k = 0$, implying the absence of a bandgap. To open a gap, the inversion symmetry in the graphene plane must be broken by making $\Delta \neq 0$. In this case, the low-energy Hamiltonian (3.1) leads to a gapped dispersion relation $E(k) = \pm\sqrt{\Delta^2 + (\hbar v_F k)^2}$ [2]. This inversion symmetry breaking can in principle be implemented experimentally. For instance, we can imagine placing graphene onto a boron nitride (BN) substrate that has the same honeycomb lattice structure and comparable lattice spacing, so that the A and B atoms experience different on-site energies [9]. In practice, however, the technological challenges that need to be met to implement such a strategy are highly non-trivial.

In bilayer graphene, in contrast, a conceptually similar strategy is within technological reach. Bilayer graphene consists of two monolayers stacked as in natural graphite (Fig. 3.1b). This so-called Bernal stacking yields a unit cell of four atoms (one atom of each of the sublattices A1, B1, A2 and B2) resulting in four electronic bands. Only two of these bands are relevant at low energy; they can be described by the effective Hamiltonian [12]

$$H = \begin{pmatrix} \Delta & -\frac{\hbar^2}{2m}(k_x - i k_y)^2 \\ -\frac{\hbar^2}{2m}(k_x + i k_y)^2 & -\Delta \end{pmatrix}. \tag{3.2}$$

This operator has a structure similar to that of equation 3.1 and, as for the monolayer, it also leads to a spectrum with zero gap between valence and conduction bands when $\Delta = 0$, but now with a quadratic dispersion relation ($E = \pm\hbar^2 k^2/2m$; Fig. 3.1b). Furthermore, and essential for our purposes, the operator (3.2) acts on spinors $\psi = (\varphi_{A1}, \varphi_{B2})^T$, which contain the amplitude of the wavefunction on atoms A1 and B2 that are located in the two different layers. This makes it possible to control the difference between the on-site energy of A1 and B2 electrostatically, simply by applying a sufficiently strong electric field E perpendicular to the carbon atom planes. In the presence of such an electric field, a gap of size 2Δ opens between conduction and valence bands [10,12,13] (Fig. 3.1c). Indeed, a bandgap originating from this mechanism has recently been observed in angle-resolved photoemission spectroscopy experiments on a chemically doped graphene bilayer, in which the electric field is associated with the charge transfer from the dopants to the carbon atoms [14] (see also ref. [15]). Here, we use a double-gate device configuration to impose a perpendicular electric field onto a graphene bilayer, which enables us to demonstrate the controlled transition from a zero-gap semiconductor to an insulator, by simply adjusting the voltages applied to the two gate electrodes.

3.3 FABRICATION OF DOUBLE-GATED GRAPHENE DEVICES

Figure 3.1d shows the device configuration that we investigate. It consists of single or double graphene layers sandwiched between two gate electrodes, and con-

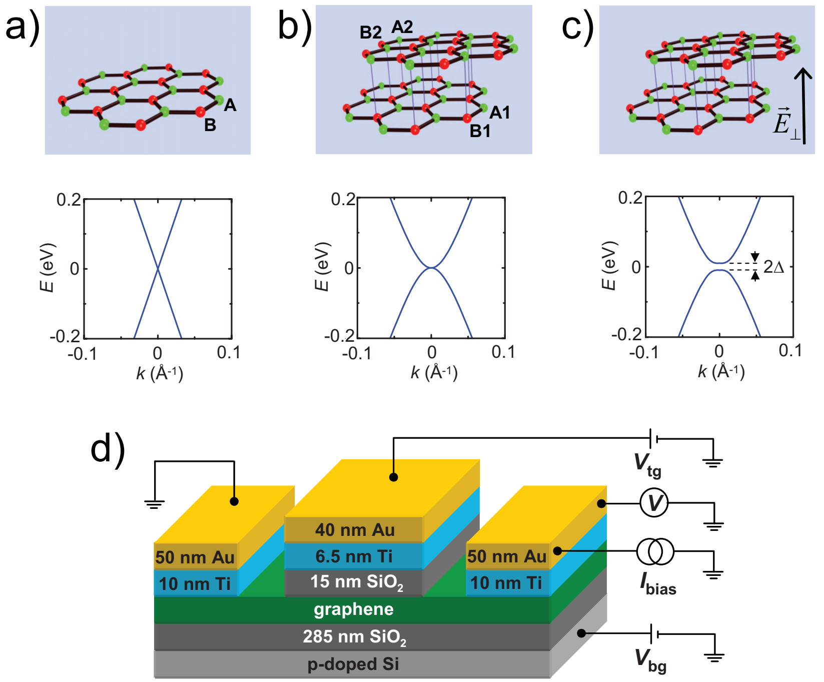

FIGURE 3.1: **Bandgap in graphene devices.** a,b, Schematic diagrams of the lattice structure of monolayer (a) and bilayer (b) graphene. The green and red coloured lattice sites indicate the A (A1/A2) and B (B1/B2) atoms of monolayer (bilayer) graphene, respectively. The diagrams represent the calculated energy dispersion relations in the low-energy regime, and show that monolayer and bilayer graphene are zero-gap semiconductors (for bilayer graphene, a pair of higher-energy bands is also present, not shown in the diagram). c, When an electric field ($E_\perp$) is applied perpendicular to the bilayer, a bandgap is opened in bilayer graphene, whose size (2Δ) is tunable by the electric field. d, Schematic diagram of a double-gated graphene device as used in our investigations. Both the Fermi level in the graphene (bi)layer and the perpendicular electric field are controllable by means of the voltages applied to the back-gate, V_{bg}, and to the top-gate, V_{tg} . We study the resistivity of the graphene (bi)layer as a function of both gate voltages by applying a current bias (I) and measuring the resulting voltage across the device, V. Note the different SiO_2 thicknesses of the dielectric layers for the top- and back-gates.

nected to metallic leads. These double-gated structures enable simultaneous and independent control of the charge density in the system (that is, the position of the Fermi level) and of the electric field perpendicular to the graphene layer. In a single layer, the presence of a perpendicular field is not expected to affect the transport properties: the conductivity of the device should never become smaller than a minimum value of the order of $4e^2/h$, irrespective of the applied gate voltages [2]. In a bilayer, on the contrary, a large applied field results in a different electrostatic potential in the two layers, which, according to theory, should cause a bandgap to open. If the Fermi level is maintained in the gap (that is, the device is operated near the charge-neutrality point), this should result in an insulating temperature dependence of the conductivity, dropping to well below $4e^2/h$ at low temperature. A unique signature of this effect is that the decrease in conductivity with lowering temperature becomes more pronounced for larger applied electric field values. This possibility to controllably induce an insulating state, which is crucial for switching devices, was missing in earlier experiments on graphene bilayers [14,15] where the gap and the carrier density could not be gate-controlled independently.

The fabrication of double-gated graphene devices is similar to what has been described elsewhere [1], and relies on micromechanical cleaving of natural graphite. The flakes used in the experiments were selected under an optical microscope and identified as single- and double-layer graphene, respectively, on the basis of their optical contrast (see §2.7; a similar method is used as previously demonstrated in refs [16,17]). Contact to the flakes was made by means of electron-beam lithography, electron-beam evaporation of a Ti/Au bilayer (10/50 nm) and lift-off. The top-gate insulating layer and electrodes were defined subsequently, by electron-beam deposition of a SiO_2 layer (15 nm) followed by deposition of a Ti/Au bilayer (6.5/40 nm), without breaking the vacuum. The comparison between single- and double-layer graphene devices is useful not only to illustrate the profound difference between them and to identify the mechanism responsible for the gate-induced insulating state, but also to rule out possible spurious effects originating from the device fabrication (for example, damage to the graphene layers or disorder introduced by the deposition of the SiO_2 gate dielectric).

3.4 CHARACTERIZATION OF SINGLE-LAYER AND BILAYER GRAPHENE DEVICES

We now proceed to discuss the systematic transport measurements that we have carried out, starting with the single-layer device shown in Fig. 3.2a. Figure 3.2b,c shows the resistance measured as a function of the voltage applied to one of the gates, with the other gate at a constant potential as indicated (we extract a car-

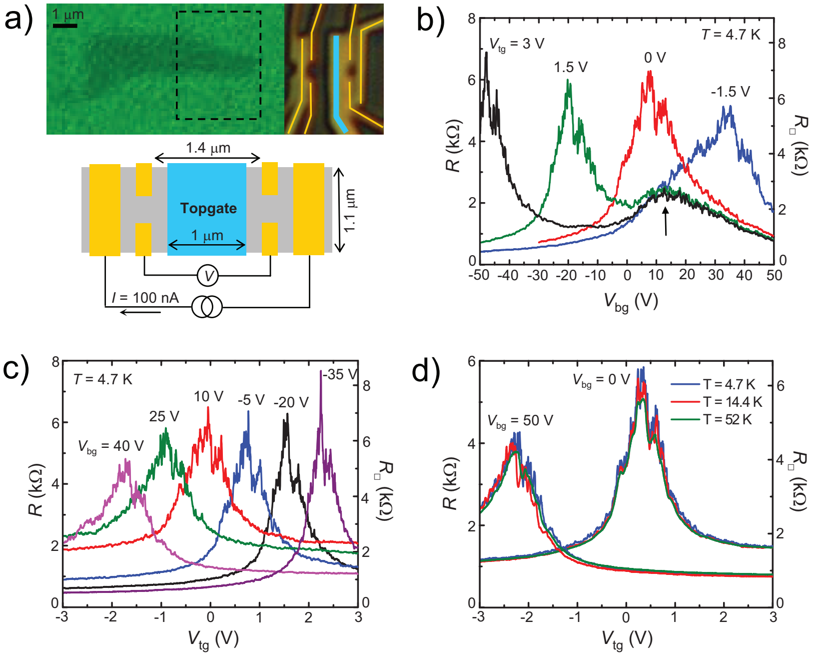

Figure 3.2: **Gate voltage and temperature dependence of transport through monolayer graphene.** a, Optical microscope images of a single-layer flake (left) and of the double-gated device fabricated on this flake (right). The yellow lines indicate metal contacts to the flake, and the blue line corresponds to the top-gate. The schematic diagram of the four-probe device configuration is also shown. b, Resistance versus back-gate voltage measured for different fixed values of the top-gate voltage showing an approximately gate voltage independent height of the charge-neutrality peak (the right axis gives an estimation of the square resistance, neglecting the contributions from the region without the top-gate and any *p*-*n* junctions to the measured resistance). The aperiodic fluctuations present near the charge-neutrality peak are reproducible and are due to quantum interference. The smaller extra peak (indicated by the arrow) is the charge-neutrality peak originating from the part of the flake that is not covered by the top-gate. c, Resistance versus top-gate voltage measured for different fixed values of back-gate voltage. Again, the height of the charge-neutrality peak is nearly gate voltage independent. The difference in the magnitude of the voltage applied to top- and back-gates (b,c) originates from the different SiO_2 thicknesses separating the two gates from the graphene flake. d, Temperature dependence of the resistance versus top-gate voltage, measured for two different back-gate voltages. Irrespective of the gate voltage configuration, the height of the charge-neutrality peak is independent of temperature in the range 4.7-52 K.

rier mobility of ~3,000 cm^2/Vs, similar to the mobility of an ungated device on the same flake). Irrespective of which gate voltage is kept constant, we always observe a peak in resistance characteristic of the behaviour of few-layer graphene and hereafter referred to as the 'charge-neutrality peak' (to be precise, we are measuring a device comprising regions of different carrier density, $n1$-$n2$-$n1$; at the resistance maximum, $n2 = 0$ only). The position of the charge-neutrality peak when sweeping one gate shifts linearly with the voltage applied to the other gate. Irrespective of the gate configuration, the height of the resistance peak remains approximately constant. From the top-gate dimensions, we can estimate a minimum conductivity value close to $4e^2/h$ (the part of the flake that is not covered by the top-gate also contributes to the resistance, but given the dimensions, this increases the conductivity estimate by at most a factor of 1.4). This is typical of graphene at the charge-neutrality point, which indicates that the device fabrication and the deposition of the top-gate dielectric have not resulted in substantial damage to the material. Note also that depending on the values of the voltages applied to both gates, p-n junctions are formed near the interfaces between the region covered by the top-gate and both uncovered regions [18]. Such p-n junctions may be the origin of the weak asymmetry seen in many of the gate sweeps in Fig. 3.2b,c. However, near the charge-neutrality point, we expect p-n junctions to give only a small contribution to the measured resistance. Finally, Fig. 3.2d shows that the gate voltage dependence of the resistance is not affected by varying the temperature between 4 and 50 K, apart from reproducible conductance fluctuations that increase in magnitude as the temperature is lowered. These observations are consistent with the expected behaviour of electrical transport through graphene monolayers [2,18-20].

The behaviour of the double-gated graphene bilayer device (Fig. 3.3a) is strikingly different. Figure 3.3b,c shows the (square) resistance of bilayer graphene as a function of the back-gate and top-gate voltages (the carrier mobility is ~1,000 cm^2/Vs, again similar to an ungated device on the same flake). Similarly to the monolayer, the position of the charge-neutrality peak shifts linearly with the respective gate voltages. Contrary to the monolayer, the charge-neutrality peaks are nearly perfectly symmetric, ruling out the possibility that the formation of p-n junctions gives a dominant contribution to the measured resistance. More importantly, the maximum resistance value now depends on the configuration of gate voltages. Specifically, when the voltage applied to both gates is close to 0 V, the height of the charge-neutrality peak corresponds to a conductivity of the order of $4e^2/h$, which is typical for zero-gap bilayers [5] (again we rely on the fact that near the charge-neutrality peak the region under the top-gate gives the largest contribution to the resistance). However, as the top- and back-gates are biased with opposite voltages of increasing magnitude, the height of the charge-neutrality peak

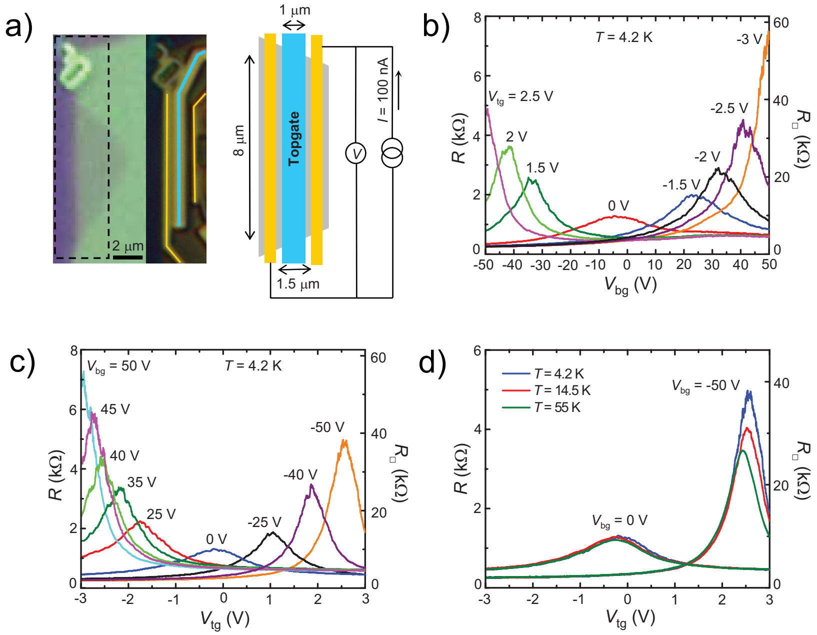

FIGURE 3.3: **Gate voltage and temperature-dependent transport through bilayer graphene.** a, Optical microscope images of a double-layer flake (left) and of the double-gated device fabricated on this flake (right). The yellow lines represent metal contacts and the blue line represents the top-gate electrode. The two-probe measurement configuration is shown in the schematic diagram (the measured resistance thus includes the contact resistance, which is smaller than $\sim 250\Omega$). b, Resistance versus back-gate voltage measured for different fixed values of the top-gate voltage (the right axis gives the square resistance, again assuming that the region under the top-gate dominates the measured resistance; this assumption is valid near the charge-neutrality peak where the resistance of the region with top-gate is relatively large). The height of the charge-neutrality peak systematically increases when both gates are biased with increasingly large opposite voltages. c, Resistance versus top-gate voltage measured for different fixed back-gate voltages showing a similar gate voltage dependence of the height of the charge-neutrality peak. d, Temperature dependence of the resistance versus top-gate voltage measured for two different values of back-gate voltage. When the voltage difference between both gates is small, the height of the charge-neutrality peak is not affected by temperature in the range 4.2-55 K. However, a clear temperature dependence is observed in this same range when both gates are biased with large opposite voltages.

exhibits a pronounced rise. In addition, the temperature dependence observed in the bilayer device is markedly different from that measured in the single-layer device (Fig. 3.3d). For small gate voltages, the resistance near the charge-neutrality peak is essentially temperature independent, characteristic of a zero-gap semiconductor. When the difference in top-gate and back-gate voltage is increased, however, the maximum resistance value also increases as the temperature is lowered. The observation of a conductivity much smaller than $4e^2/h$ exhibiting an insulating temperature dependence for oppositely biased gate electrodes is what we would expect qualitatively in a bilayer graphene device.

3.5 TRANSPORT IN THE INSULATING REGIME

To confirm that in the double-gated bilayer device large differences in voltage between the top- and back-gate do lead to an insulating state, we have carried out measurements in a dilution refrigerator, in the temperature range between 50 mK and 1.2 K, where the increase in resistance with lowering temperature should be more pronounced. Indeed, Fig. 3.4a (note the logarithmic scale) shows that when the top- and back-gates are biased asymmetrically, a very strong temperature dependence of the square resistance is observed near the charge-neutrality peak, reaching values between 10 and 100 MΩ at 55 mK. This is in stark contrast to the case of small gate voltages (Fig. 3.4a, inset), for which a temperature independent resistance near the charge-neutrality peak – corresponding to a conductivity of approximately $4e^2/h$ – persists down to the lowest temperature. The full dependence of the square resistance measured at 50 mK as function of the voltage applied to both gate electrodes is shown in Fig. 3.4b,c, from which the very fast increase in resistance near the charge-neutrality peak with increasing the electric field applied perpendicular to the layer is apparent. According to the expectations, the region of high resistance scales linearly with both top- and back-gate voltage (see the white dotted line in Fig. 3.4c) as it is required to maintain charge neutrality in the graphene bilayer. In addition, we have also measured the I-V characteristics of the device for different top- and back-gate voltage configurations (Fig. 3.4d) and observed that they evolve from exhibiting a linear ohmic behaviour far from the charge-neutrality peak, to a pronounced nonlinear behaviour near the charge-neutrality peak.

Finally, we discuss more quantitatively the insulating temperature dependence of the resistance that we observe for large oppositely biased gates. In an ideal defect-free insulator, thermally activated transport is expected, whereby the maximum resistance, R, varies with temperature as $R(T) \propto \exp(E_a/kT)$, where k is Boltzmann's constant and E_a is the activation energy, corresponding to half the bandgap. Our data, however, do not exhibit such a simple thermal activation be-

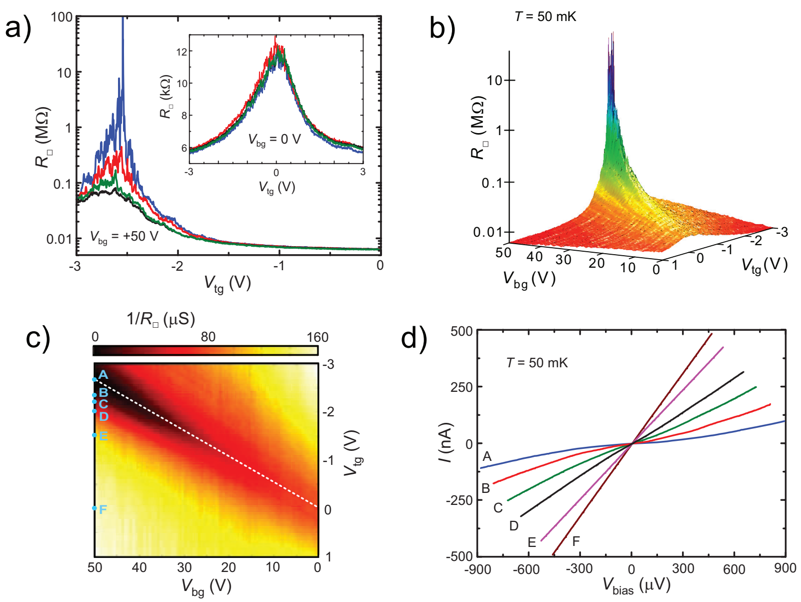

Figure 3.4: **Gate-induced insulating state in the bilayer graphene device.** a, Square resistance as a function of top-gate voltage measured at different temperatures: $T = 55$ mK (blue line), $T = 270$ mK (red line), $T = 600$ mK (green line) and $T = 1{,}200$ mK (black line) (the back-gate voltage is kept fixed at $V_{bg} = +50$ V). Here, the square resistance is plotted, because near the charge-neutrality peak the resistance is almost completely dominated by the region under the top-gate. A pronounced temperature dependence is observed when the top- and back-gates are biased asymmetrically; when both gates are symmetrically biased no temperature dependence is observed (see inset). b, Three-dimensional plot of the square resistance as a function of both top- and back-gate voltage at $T = 50$ mK, showing a sharp rise of the height of the charge-neutrality peak with electric field. c, Colour plot of the same data, showing that the position of the charge-neutrality peak shifts linearly with both gate voltages. The dark-coloured region corresponds to voltage configurations where an insulating state is observed. d, I-V characteristics measured at different gate voltage configurations (the letters correspond to the letters in c, which indicate both gate voltages). The data in a, b and c were taken with lock-in detection, using a zero-voltage bias with a 5 μV excitation voltage modulated at 17 Hz. The data in (d) were measured with a d.c. voltage bias. Note that the plotted voltage bias is corrected for the internal resistance (1.1 kΩ) of the current measurement unit used in the experiment.

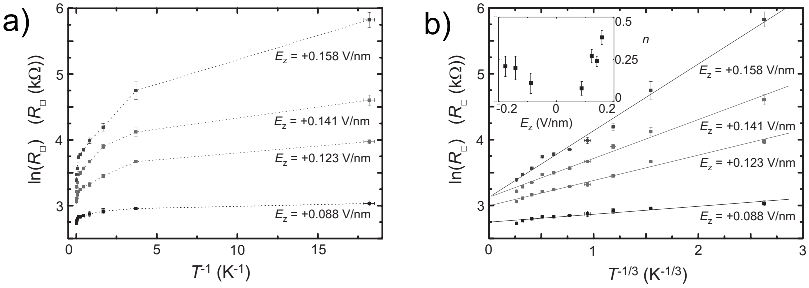

FIGURE 3.5: **Thermally activated hopping transport in biased bilayer graphene.** a, Logarithm of the square resistance at the charge-neutrality peak versus inverse temperature, for different perpendicular electric fields ($E_\perp = (V_{bg} - V_{tg})/(d_{bg} + d_{tg})$, where d_{bg} and d_{tg} are the thicknesses of the back- and top-gate oxides). These plots clearly show sublinear behaviour in the temperature range from 55 mK to 55 K (the dotted lines are a guide to the eye), implying that the data cannot be described by $R(T) \propto \exp(E_a/kT)$. b, Logarithm of the square resistance of the charge-neutrality peak as function of $T^{-1/3}$ for different perpendicular electric fields in the temperature range from 55 mK to 55 K. The linear fits to the data (solid lines) show that, at the highest fields, the data are well described by $R(T) \propto \exp(T_0/T)^{1/3}$. At lower fields, the fitted exponent, n, is smaller than 1/3 (see inset; the error bars reflect the standard deviation of the fitted values).

haviour (Fig. 3.5a). Below approximately $T = 5$ K, and at the highest applied electric fields, they are much better described by $R(T) \propto \exp(T_0/T)^{1/3}$, as seen in Fig. 3.5b, with fitted values of T_0 of ~0.5-0.8 K (note that between 5 and 55 K the resistance drops more rapidly with increasing temperature, but the range is too small to deduce an accurate value for the activation energy). Qualitatively, an $n = 1/3$ exponent is expected for transport in two dimensions of non-interacting carriers via variable-range hopping in insulating materials where transport is mediated by localized impurity sites that are present inside a gap [21,22]. Such localized states have been predicted theoretically in the case of disordered bilayer graphene [23], but drawing quantitative conclusions as to the properties of these states, for example, their density of states, spatial extension, and so on, is not straightforward from our measurements and goes beyond the scope of this article. For smaller applied perpendicular electric fields, the fitted exponent becomes smaller than 1/3 and decreases towards zero (see inset of Fig. 3.5b), and the fitted value of T_0 also decreases. This indicates clearly that the insulating temperature dependence of the resistance that we measure becomes stronger when the applied perpendicular electric field is higher.

3.6 CONCLUSIONS AND DISCUSSION

We conclude that the data unambiguously show the occurrence of an insulating state in bilayer graphene in the presence of a perpendicular electric field, which has not been reported earlier. Our observation that the insulating state occurs only in bilayers and not in monolayers, and that the increase in resistance with lowering temperature is more pronounced for larger values of the electric field applied perpendicular to the material, is in agreement with the predicted controlled opening of a bandgap. In contrast, these two very specific observations cannot be accounted for simply by an increase in the amount of disorder, for instance caused by the presence of the top-gate. Furthermore, as pointed out earlier, carrier mobilities were comparable in devices with and without top-gates, actually suggesting equal amounts of disorder. Although we cannot rule out that mechanisms other than the formation of a bandgap could lead to the same striking observations, we believe this explanation is the most plausible.

It is clear from the experiments that a possible gap induced in the bilayer device is rather small. This is consistent with recent theoretical calculations [10,13], which, for zero carrier density and for electric field values of the order of those achieved in our experiments, predict a gap size below approximately 10 meV depending on, for instance, the way in which screening effects in the bilayer are modelled (note that in refs [14,15], measurements were done at very high charge density, where much larger gap sizes were expected and observed). In comparison, the energy scale of disorder can be estimated to be of the order of a few milli-electron volts from measurements of the spin splitting in the quantum Hall regime [24], and larger from scanning single-electron transistor experiments [25]. Altogether, it seems that a gap of below 10 meV in conjunction with the presence of subgap states originating from disorder can account for the observed $\exp(T^{-1/3})$ dependence of the resistance in the temperature range between 50 mK and 4.2 K. However, this does not well explain the steep dependence on electric field at 55 K and on temperature above 4.2 K. It is possible that the gap is in fact larger than predicted, or alternatively there may be other mechanisms also contributing to the observed resistance increase in this $n1$-$n2$-$n1$ device.

The possibility to use double-gated structures to suppress the conductivity of bilayer graphene to values much lower than $4e^2/h$ represents an important proof-of-principle for the feasibility of future graphene-based electronic devices. Obviously the development of practical devices will require further innovations, which are needed to switch off electrical conduction at room temperature. Nevertheless, the operation of devices at cryogenic temperatures that we have demonstrated here will already enable new fundamental studies of quantum transport in bilayer graphene, through the fabrication of structures such as quantum point contacts based on split gates and electrostatically tunable quantum dots.

3.7 REFERENCES

1. Novoselov, K. S. et al., Electric field effect in atomically thin carbon films, Science 306, 666-669 (2004).
2. Novoselov, K. S. et al., Two-dimensional gas of massless Dirac fermions in graphene, Nature 438, 197-200 (2005).
3. Zhang, Y. B., Tan, Y.W., Stormer, H. L. & Kim, P., Experimental observation of the quantum Hall effect and Berry's phase in graphene, Nature 438, 201-204 (2005).
4. Novoselov, K. S. et al., Unconventional quantum Hall effect and Berry's phase of 2π in bilayer graphene, Nature Phys. 2, 177-180 (2006).
5. Geim, A. K. & Novoselov, K. S., The rise of graphene, Nature Mater. 6, 183-191 (2007).
6. Wallace, P. R., The band theory of graphite, Phys. Rev. 71, 622-634 (1947).
7. Katsnelson, M. I., Novoselov, K. S. & Geim, A. K., Chiral tunnelling and the Klein paradox in graphene, Nature Phys. 2, 620-625 (2006).
8. Han, M. Y., Özyilmaz, B., Zhang, Y. & Kim, P., Energy band-gap engineering of graphene nanoribbons, Phys. Rev. Lett. 98, 206805 (2007).
9. Giovannetti, G., Khomyakov, P. A., Brocks, G., Kelly, P. J. & Van den Brink, J., Substrate-induced bandgap in graphene on hexagonal boron nitride: Ab initio density functional calculations, Phys. Rev. B 76, 073103 (2007).
10. McCann, E., Asymmetry gap in the electronic band structure of bilayer graphene, Phys. Rev. B 74, 161403 (2006).
11. Semenoff, G. W., Condensed matter simulation of a three-dimensional anomaly, Phys. Rev. Lett. 53, 2449-2452 (1984).
12. McCann, E. & Fal'ko, V. I., Landau-level degeneracy and quantum Hall effect in a graphite bilayer, Phys. Rev. Lett. 96, 086805 (2006).
13. Min, H., Sahu, B. R., Banerjee, S. K. & MacDonald, A. H., Ab initio theory of gate induced gaps in graphene bilayers, Phys. Rev. B 75, 155115 (2007).
14. Ohta, T., Bostwick, A., Seyller, T., Horn, K. & Rotenberg, E., Controlling the electronic structure of bilayer graphene, Science 313, 951-954 (2006).
15. Castro, E. V. et al., Biased bilayer graphene: Semiconductor with a gap tunable by electric field effect, Phys. Rev. Lett. 99, 216802 (2007).
16. Blake, P. et al., Making graphene visible, Appl. Phys. Lett. 91, 063124 (2007).
17. Abergel, D. S. L., Russell, A. & Fal'ko, V. I., Visibility of graphene flakes on a dielectric substrate, Appl. Phys. Lett. 91, 063125 (2007).
18. Huard, B. et al., Transport measurements across a tunable potential barrier in graphene, Phys. Rev. Lett. 98, 236803 (2007).
19. Williams, J. R., DiCarlo, L. & Marcus, C. M., Quantum Hall effect in a gate-

controlled p-n junction of graphene, Science 317, 638-641 (2007).
20. Özyilmaz, B. et al., Electronic transport and quantum Hall effect in bipolar graphene p-n-p junctions, Phys. Rev. Lett. 99, 166804 (2007).
21. Madelung, O., Introduction to Solid-State Theory (Springer, Berlin, Heidelberg, 1978).
22. Shklovskii, B. I. & Efros, A. L., Electronic Properties of Doped Semiconductors (Springer, Berlin, Heidelberg, 1984).
23. Nilsson, J. & Castro Neto, A. H., Impurities in a biased graphene bilayer, Phys. Rev. Lett. 98, 126801 (2007).
24. Zhang, Y. et al., Landau-level splitting in graphene in high magnetic fields, Phys. Rev. Lett. 96, 136806 (2007).
25. Martin, J. et al., Observation of electron-hole puddles in graphene using a scanning single electron transistor, Nature Phys. 4, 144-148 (2008).

4

GATE-INDUCED BAND OVERLAP IN TRILAYER GRAPHENE

Graphene-based materials are promising candidates for nano-electronic devices [1-14] because very high carrier mobilities can be achieved without the use of sophisticated material preparation techniques [1]. However, the carrier mobilities reported for single-layer and bilayer graphene are still less than those reported for graphite crystals at low temperatures, and the optimum number of graphene layers for any given application is currently unclear, because the charge transport properties of samples containing three or more graphene layers have not yet been investigated systematically [1]. Here, we study charge transport through trilayer graphene as a function of carrier density, temperature, and perpendicular electric field. We find that trilayer graphene is a semimetal with a resistivity that decreases with increasing electric field, a behaviour that is markedly different from that of single-layer and bilayer graphene. We show that the phenomenon originates from an overlap between the conduction and valence bands that can be controlled by an electric field, a property that had never previously been observed in any other semimetal. We also determine the effective mass of the charge carriers, and show that it accounts for a large part of the variation in the carrier mobility as the number of layers in the sample is varied.

The contents of this chapter have been published in *Nature Nanotechnology*:
M. F. Craciun, S. Russo, M. Yamamoto, J. B. Oostinga, A. F. Morpurgo, S. Tarucha, *Trilayer graphene is a semimetal with gate-tunable band overlap.* Nature Nanotechnology **4** (6), 383-388 (2009).

4.1 INTRODUCTION

Electron and hole mobilities as high as $1 \cdot 10^4$ cm^2/Vs are routinely observed in single and bilayer graphene on substrates [2-7,9-12], and values as high as $2 \cdot 10^5$ cm^2/Vs have been reported for suspended graphene [15]. However, carrier mobilities in excess of $1 \cdot 10^6$ cm^2/Vs have been measured in graphite at low temperature [16-18], and it is natural to ask if the carrier mobility can be increased by simply increasing the number of graphene layers in the material. It is also important to understand how the general electronic properties of graphene-based materials evolve from those of graphene to those of graphite as the number of layers is increased. Note that the low-energy electronic properties of samples containing three or more graphene layers depend on a large number of parameters, and theorists have been unable to agree about the details of the electronic structure (see, for example, refs. [19-23]). Here, as a first step to address these issues, we investigate charge transport through trilayer graphene, which is the thinnest graphene-based system with a tight-binding Hamiltonian that includes all the transfer integrals that are needed to describe the band structure of graphite [19-23].

4.2 DEVICE FABRICATION

The fabrication of trilayer-based nano-electronic devices relies on micromechanical cleaving of graphite crystals (see ref. [1] and the footnote [†] for details), which enables the deposition of few-layer graphene on top of an oxidized silicon substrate. The layer thickness was identified by analysing the shift in green intensity under an optical microscope [10] (see §2.7). Care was taken to select flakes formed by regions of different thickness, and to fabricate devices on each region (Fig. 4.1a), only a few micrometres apart. The spatial proximity of devices fabricated on the same flake ensures that the disorder induced by the substrate has comparable magnitude, which facilitates a direct comparison of the electrical properties of single-layer, bilayer and trilayer graphene.

[†] Few-layer graphene was obtained by means of mechanical exfoliation of bulk graphite and transferred onto the surface of a highly doped silicon substrate covered by a 285 nm thick layer of thermally grown SiO$_2$. The highly doped silicon substrate was used as the back-gate, and the top-gate was defined by means of electron-beam lithography and lift-off of electron-beam evaporated SiO$_2$ and of a titanium/gold bilayer (the thicknesses of the SiO$_2$, titanium, and gold were 15, 10 and 100 nm, respectively). To maximize the contribution of the gated regions to the total resistance measured in a two-probe configuration, two ohmic contacts (made of titanium and gold, of thicknesses 10 and 100 nm) were fabricated (again by electron-beam evaporation and lift-off) within 50 nm from the edge of the 1 μm wide top-gate. Less than 5 % of the overall resistivity was therefore due to the non-gated region.

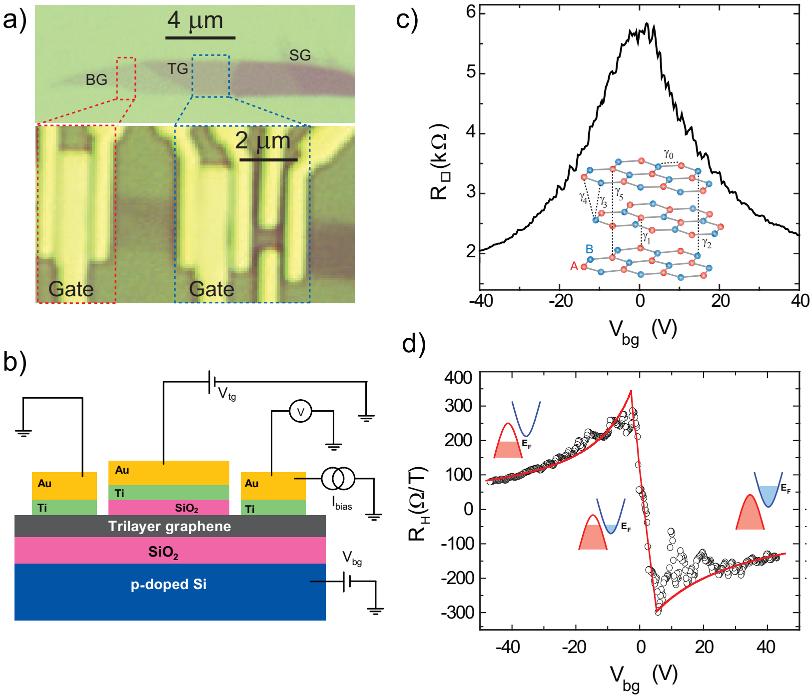

FIGURE 4.1: **Characterization of trilayer graphene.** a, Optical microscope images of an exfoliated graphite flake (top) containing single-layer graphene (SG), bilayer graphene (BG) and trilayer graphene (TG), and of the devices (bottom) fabricated on the bilayer and trilayer parts of the same flake. b, Schematic of a double-gated device. The position of the Fermi level in trilayer graphene and the applied perpendicular electric field are controlled by the voltages applied to the back-gate (V_{bg}) and the top-gate (V_{tg}). We study the resistance of the layers as a function of these gate voltages by applying an a.c. (f = 13 Hz) current bias I and measuring the resulting voltage V across the device with a lock-in amplifier. c, Square resistance as a function of V_{bg} at 50 mK. The inset shows the crystal structure of a trilayer graphene. The parameters γ_0 to γ_5 label the tight-binding transfer integrals between the different pairs of atoms. d, Measured Hall coefficient as a function of V_{bg} (open circles) for a fixed perpendicular magnetic field of 9 T at 50 mK. The red curve is a fit (see the footnote ‡). The three insets schematically depict the position of the Fermi level (E_F) at different values of V_{bg}.

4.3 ELECTRIC FIELD-EFFECT IN TRILAYER GRAPHENE

The field-effect behaviour in trilayer graphene devices manifests itself in the dependence of the square resistance ($R_\square$) and the Hall coefficient (R_H) on the voltage V_{bg} applied to the silicon back-gate (these measurements were carried out in devices without a top-gate, in a four-probe configuration, using a Hall-bar geometry). Specifically, $R_\square$ shows a peak (see Fig. 4.1c and inset of Fig. 4.5a) that is broader and less pronounced than the peaks for single-layer and bilayer graphene. R_H displays a non-monotonous behaviour as a function of V_{bg}, with a characteristic sign reversal at the position of the maximum resistance, V_{bg}^{max} (see Fig. 4.1d). In trilayer graphene the range of V_{bg} over which R_H decreases and changes sign is much wider ($\Delta V_{bg} \approx 8$ V) than in single-layer and bilayer graphene, which are zero-gap semiconductors ($\Delta V_{bg} \approx 1$ V for single-layer and bilayer graphene present on the same flake of the trilayer). Such a large ΔV_{bg}, as well as the broader and shallower peak in resistivity, should be expected if trilayer graphene is a semimetal, due to the finite overlap ($\delta\varepsilon$) of the conduction and valence bands. Indeed, under the assumption that trilayer graphenes are semimetals, we can satisfactorily fit R_H over the whole range of V_{bg} with a $\delta\varepsilon \approx 28$ mV (see the footnote [‡] for details).

Our experiments on trilayer graphene heavily rely on the application of a tunable, static electric field perpendicular to the layer, which provides a unique tool to investigate the electronic properties of graphene-based materials [10-12,24,25]. To generate such a perpendicular field we use double-gated devices (see Fig. 4.1b) that also provide independent control of the carrier density in the material (that is, the position of the Fermi level). Figure 4.2a,b shows $R_\square$ for a double-gated trilayer graphene device measured at $T = 50$ mK as a function of the voltage applied to one of the gates, while the other gate is kept at a constant potential. These measurements on double-gated devices were mainly carried out in a two-terminal con-

---

[‡] The dependence of the Hall coefficient R_H on the back-gate voltage V_{bg} indicates the semimetallic nature of trilayer graphene, and can be used to extract an estimate of the band overlap. To fit the data in Fig. 4.1d we used the fact that, when the Fermi level is located deep in the conduction or valence bands (so that only electrons or holes are present, $V_{bg} \gg 6$ V and $V_{bg} \ll -2$ V), $R_H = 1/en_{e,h}$, with $n_{e,h}$ being the electron/hole carrier concentration. In the mixed charge carrier regime, when both electrons and holes are present simultaneously, R_H is a function of both carrier charge densities and mobility $\mu_{e,h}$: $R_H = (n_h\mu_h^2 - n_e\mu_e^2)/e(n_e\mu_e + n_h\mu_h)^2$. Using these formulae, we can fit $R_H(V_{bg})$ over the entire V_{bg} range. In doing this, the total charge density of carriers is calculated from the known capacitance to the gate ($n = \varepsilon_0\varepsilon V_{bg}/d_{bg}e$) and $\mu_{e,h}$ are taken to be constant (that is, V_{bg}-independent) and equal to the values obtained from the gate voltage dependence of the conductivity at high V_{bg} values (that is, far outside the mixed charge carrier regime). The only fitting parameter is the band overlap $\delta\varepsilon$, which is related to the V_{bg} width of the mixed state through the density of states of the quadratically dispersing electron and hole bands. Note that the Hall effect measurements were carried out on samples with back-gate only (that is, no top-gate) and so only the value of $\delta\varepsilon$ at zero perpendicular electric field can be obtained in this way.

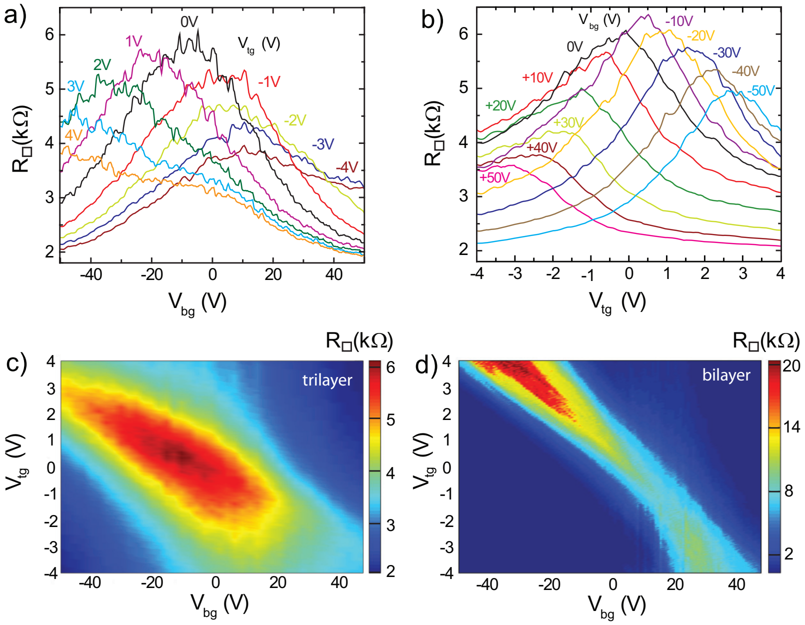

FIGURE 4.2: **Transport in the presence of a perpendicular electric field.** a, Square resistance of a trilayer device versus back-gate voltage V_{bg} for different values of the top-gate voltage V_{tg} at 50 mK. V_{bg} is an order of magnitude larger than V_{tg} because the bottom-gate insulator is an order of magnitude thicker than the top-gate insulator. The value of $R_{\square}^{max}$ systematically decreases when the perpendicular electric field applied is increased. b, Square resistance of a trilayer device versus V_{tg} for different values of V_{bg} at 50 mK. Again, the value of $R_{\square}^{max}$ systematically decreases as the electric field is increased. c,d, Colour plots of the square resistance of trilayer graphene at 50 mK (c) and bilayer graphene at 300 mK (d) as a function of both V_{bg} and V_{tg}. Whereas the applied electric field enhances the overlap between valence and conduction bands in trilayer graphene (leading to an increase in conductance), it opens up a gap in bilayer graphene (leading to an increase in resistance).

figuration, which allowed the fabrication and comparison of a larger number of devices on flakes containing layers of different thickness. Measurements in a four-terminal configuration were also performed on several devices to ensure that the effect of the contact resistance – present in two-terminal measurements – did not influence significantly the results (see ref. [26] and the footnote [§] for details).

Irrespective of which gate voltage is being swept, we always observe a maximum in the resistance $R_{\Box}^{max}$, which is attained at the charge neutrality point where the electron and hole density in the system are the same. As expected, the position of $R_{\Box}^{max}$ that is observed when sweeping one gate shifts as a function of the voltage applied to the other gate, reflecting the change in charge density induced by the two gates. More importantly, we observe that the maximum resistance value at the charge neutrality point depends on the configuration of the gate voltages, (Fig. 4.2a,b). In particular, the height of $R_{\Box}^{max}$ decreases as the top- and back-gates are biased with voltages of opposite polarity and of increasing magnitude (that is, $R_{\Box}^{max}$ decreases when the applied perpendicular electric field increases).

The electric field response of $R_{\Box}^{max}$ measured at 50 mK for trilayer graphene is summarized in the colour plot of $R_{\Box}^{max}$ in Fig. 4.2c. The systematic decrease of $R_{\Box}^{max}$ as a function of electric field, which is observed in all the measured devices, is different from the behaviour of other few-layer graphenes studied in the past and appears to be unique to trilayer graphene. Specifically, it has been shown that a perpendicular electric field applied on single-layer graphene does not affect the value of the resistance maximum $R_{\Box}^{max}$, and that on double-gated bilayer graphene $R_{\Box}^{max}$ increases when increasing the electric field, consistent with the opening of a gap in the density of states [10-12,24,25] (see also Fig. 4.2d). We therefore conclude that the observed decrease of $R_{\Box}^{max}$ with external electric field is a characteristic

---

[§] Longitudinal and transverse magnetoresistance were measured in a Hall-bar geometry, in devices containing only a back-gate and no top-gate. In this case measurements could be performed in a four-terminal configuration, where the contact resistance between metal electrodes and trilayer graphene plays no role. On the contrary, in double-gated devices, the introduction of voltage probes under the top-gate proved to be technically very difficult (due to the failure of the SiO_2 layer insulating the trilayer graphene from the top-gate). Therefore, although we also investigated devices where measurements were carried out in a four-terminal configuration, we opted to investigate the dependence of $R_{\Box}$ on the perpendicular electric field mostly by means of two-terminal measurements. In such a two-terminal geometry the influence of the contact resistance needs to be considered. We have successfully measured the contact resistance in different ways (by comparing the results of two terminal measurements performed on devices fabricated on the same flake, by comparing two- and four-terminal measurements and by scaling experiments as a function of the contact separation). We found that the contact resistance is always weakly gate-voltage dependent and in all cases less than 20 % than the total resistance measured at high gate voltage. Close to the charge neutrality point, where $R_{\Box}$ is larger, the relative effect of the contact resistance is even smaller (typically less than 10 %). We conclude that the presence of a contact resistance does not significantly affect our results and their interpretation. Note, finally, that in the samples where we performed four-terminal measurements, the results for $\delta\varepsilon$ were fully consistent with those obtained from two-terminal measurements.

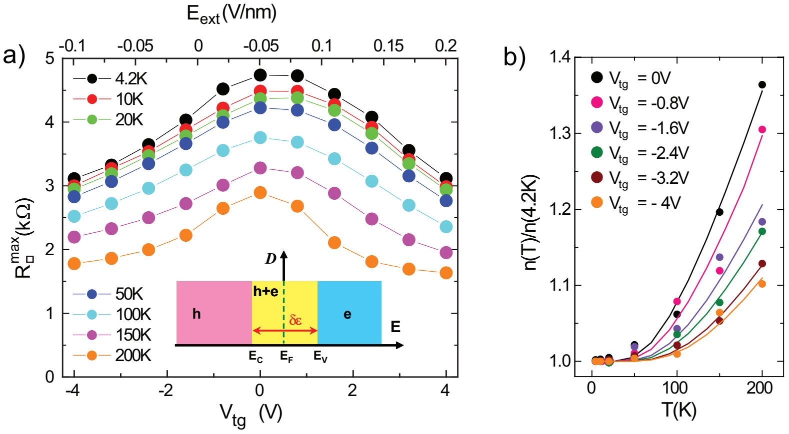

FIGURE 4.3: **Temperature-dependent transport through trilayer graphene.** a, Maximum square resistance $R_\square^{max}$ versus top-gate voltage V_{tg} at different temperatures. For each value of V_{tg}, the back-gate voltage V_{bg} is chosen so that the device is at the charge neutrality point; different values of V_{bg} correspond to different values of the applied electric field E_{ext}. The inset shows a schematic view of the density of states of the quadratic bands that are responsible for the semimetallic behaviour of trilayer graphene. At the charge neutrality point, where the resistance reaches its maximum, the Fermi level E_F lies between the bottom of conduction band E_c and the top of the valence band E_v. b, Temperature dependence of the carrier concentration n in the mixed state determined from the value of $R_\square^{max}$ measured at different values of V_{tg} (or E_{ext}). The solid curves represent the fitted dependence using the expression $n(T)/n(4.2K) = (T/4.2)\ln(1+e^{\delta\varepsilon/2k_BT})/\ln(1+e^{\delta\varepsilon/2k_B4.2})$, from which we extract the band overlap $\delta\varepsilon$.

fingerprint of trilayer graphene. Note that, for trilayer graphene, the same electric field dependence of $R_{\square}^{max}$ is preserved over the entire experimentally investigated temperature range (up to 200 K). This is clearly summarized in Fig. 4.3a, which shows $R_{\square}^{max}$ measured as a function of V_{tg} (with V_{bg} chosen correspondingly at each point, to maintain the device charge neutral), for different temperatures. The temperature-dependent measurements also show that $R_{\square}^{max}$ decreases when raising the temperature.

4.4 DETERMINATION OF THE BAND OVERLAP

As we will now show, all our experimental observations can be consistently interpreted quantitatively in terms of the semimetallic behaviour of trilayer graphene, if the overlap between the valence and conduction bands progressively increases with increasing applied perpendicular electric field. To understand the details of our analysis, it is important to recall the basic aspects of the electronic structure of trilayer graphene. At low energy, Bernal-stacked trilayer graphene (see inset of Fig. 4.1c), which is the thermodynamically stable form, has two valence and two conduction bands. Within a tight-binding scheme analogous to the Slonczewski-Weiss-McClure model used to describe graphite [27,28], the precise details of these bands depend on the values of all the transfer integrals introduced. However, if in a first approximation these details are disregarded, for both valence and conduction bands, one band disperses linearly and the other quadratically. Because the density of states of linearly dispersing bands goes to zero at zero energy, the bands that are relevant to understand the low-energy transport properties are the ones dispersing quadratically, which give the dominant contribution to the total density of states. In interpreting our data, therefore, we will consider only the low-energy valence and conduction bands with quadratic dispersion relation, and we will assume the presence of a finite band overlap $\delta\varepsilon$ [♯]. In addition, as is predicted theoretically by the simplest tight-binding models for trilayer graphene [30], we will take the effective mass in the valence and conduction (quadratically dispersing) bands to be equal ($m_e^* = m_h^* = m^*$).

[♯] In our analysis we have assumed that the low energy trilayer bandstructure is described by two quadratic bands wich have an overlap $\delta\varepsilon$. This approximation disregards the detailed low energy trilayer bandstructure, and it will be important to check if an analysis of the data in terms of the precise band structure of trilayer graphene (i.e., not relying on the two parabolic bands only) is consistent with our observations. Theoretical results based on tight binding model -containing the detailed low energy electronic properties- appear to confirm that also when the fully detailed low energy trilayer graphene band structure is taken into account, good agreement with our experimental results is obtained [29]. These calculations also shed light on the origin of the band overlap, which is due to the non-zero value of the transfer integrals γ_2 and γ_5, rationalizing why a sizable band overlap appears in trilayers, but not in single- and bi-layers.

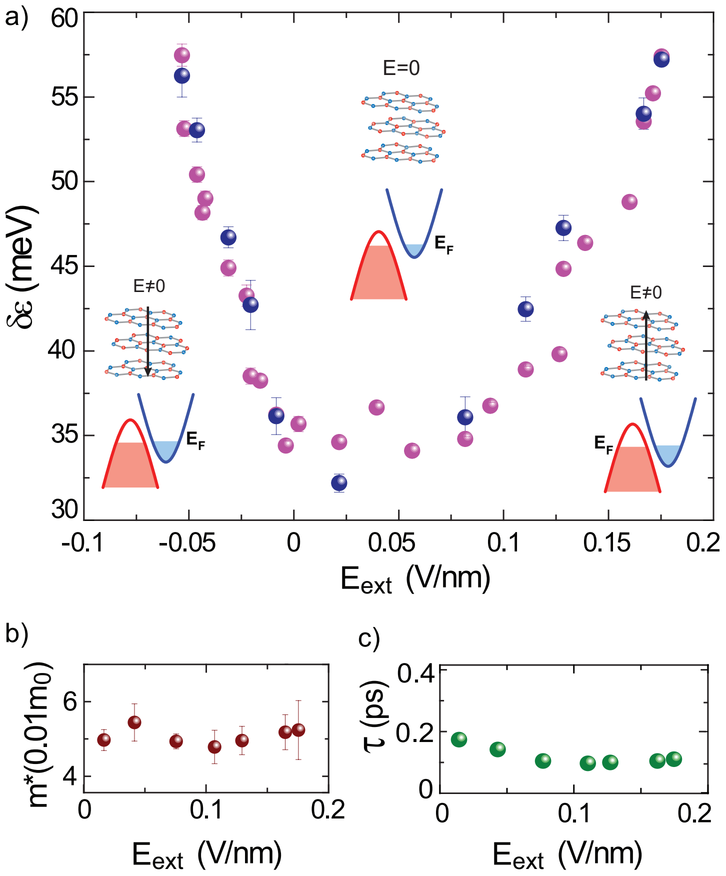

FIGURE 4.4: **Electric field dependence of the band overlap in trilayer graphene.** a, Band overlap $\delta\varepsilon$ versus applied electric field E_{ext}. The dark blue dots represent the values estimated from the temperature dependence of the charge density in the mixed state (see Fig. 4.3b). The purple dots are the values estimated from the maximum resistivity measured at 50 mK, using the theoretical value of the effective mass for the quadratic bands ($m^* = 0.052 m_0$). The inset shows a schematic view of the band structure, showing that the band overlap increases when E_{ext} is nonzero. b, Effective mass (derived from experimental data; see main text) versus E_{ext}. c, The scattering time τ extracted from the measured conductivity and effective electron mass using the Drude formula together with the experimentally determined m^*.

We first analyse the temperature dependence of $R_{\square}^{max}$, which allows the direct determination of the band overlap $\delta\varepsilon$ for all values of the applied perpendicular electric field. Within the scenario introduced above (and along the lines of the discussion of Ref. [1]), $R_{\square}^{max}$ is related to the total carrier density (that is, electron plus hole density) in the mixed state through the relation $n = 2/[e(\mu_e + \mu_h)R_{\square}^{max}]$ (note that $n_e = n_h = n/2$). The decrease in $R_{\square}^{max}$ with increasing temperature originates from the increase in the number of thermally excited carriers around the Fermi energy, which, for a semimetal, can be written as $n(T) = (16\pi m^*/h^2 c)k_B T \ln[1 + e^{\delta\varepsilon/2k_B T}]$ (with c equal to twice the layer spacing) [31]. By normalizing $n(T)$ to the value at $T = 4.2$ K, $n(T)/n(4.2K) = (T/4.2)\ln(1+e^{\delta\varepsilon/2k_B T})/\ln(1+e^{\delta\varepsilon/2k_B 4.2})$, the band overlap $\delta\varepsilon$ can be directly obtained through a one-parameter fit to the experimental data. Figure 4.3b shows that an excellent quality of the fit is obtained for all values of the applied perpendicular electric field E_{ext} ($E_{ext} = (V_{tg} - V_{bg}^{m})/(d_{tg} + d_{bg})$, where V_{bg}^{m} is the value of V_{bg} for which the resistance is maximum and $d_{bg,tg}$ are the thicknesses of the dielectrics for the back- and top-gates). The values of the band overlap obtained in this way are plotted in Fig. 4.4a as a function of field: it is apparent that the band overlap changes as a function of the external electric field, and $\delta\varepsilon$ increases with increasing E_{ext} from ~30 to 60 meV, independent of the electric field polarity.

The band overlap and its electric field dependence can also be extracted by looking only at the low-temperature (50 mK) measurements. In fact, at such a low temperature, $\delta\varepsilon = n/D$, with $D = 2m^*/\pi\hbar^2$ the total low-energy two-dimensional density of states. Because $\delta\varepsilon$ and $n = 2/[e(\mu_e+\mu_h)R_{\square}^{max}]$ are experimentally known, we can use this relation to extract the effective mass of the charge carriers: $m^* = \pi\hbar^2/[e(\mu_e + \mu_h)R_{\square}^{max}\delta\varepsilon]$. We find that at $E_{ext} = 0$ the estimated effective mass is $m^* = (0.054 \pm 0.005)m_0$, and that m^* remains constant when E_{ext} is increased (see Fig. 4.4b; m_0 is the free electron mass). This value of the effective mass is consistent with theoretical predictions based on tight-binding calculations, which give $m^* = (2\sqrt{2}/3)\hbar^2\gamma_1/(a^2\gamma_0^2) = 0.052m_0$ (ref. [30]) ($a = 0.246$ nm, the monolayer lattice constant, $\gamma_0 = 3.16$ eV (ref. [17]), $\gamma_1 = 0.44$ eV (ref. [32])). Having determined the effective mass, and with the carrier density and the conductivity known, we can use the Drude formula for conductivity to extract the scattering time τ. As shown in Fig. 4.4c, we find that τ decreases with increasing applied electric field. These observations confirm that the overall electric field dependence of the resistance with increasing electric field is due to a relative shift of valence and conduction band, leading to an increase in band overlap, and not to changes in effective mass (which are negligible) or in scattering time (which would tend to increase, rather than to decrease, the resistance; see Fig. 4.4c). This electric field tunable band overlap is a unique property of trilayer graphene, which has never been previously

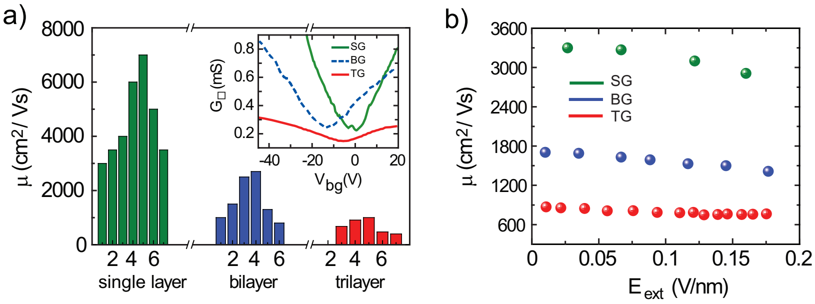

FIGURE 4.5: **Comparison of carrier mobility in few-layer graphene.** a, Statistics of mobility values in single-layer, bilayer and trilayer graphene, estimated from the dependence of the conductivity σ on the back-gate voltage V_{bg}. Trilayers systematically exhibit lower mobility, and the ratio between the average mobility in bilayer and trilayer graphene is approximately consistent with the ratio of the effective mass of the charge carriers in the two materials. The inset shows the conductivity versus V_{bg}: the finite band overlap in trilayer graphene results in a lower minimum conductivity compared with bilayer and trilayer graphene. b, Mobility versus applied electric field E_{ext}, also showing a different behaviour for different layer thickness. In particular, the decrease in the mobility with increasing E_{ext} becomes less pronounced as the number of layers increases.

found in other semimetallic systems.

An alternative – but fully equivalent – way to look at our data, which better illustrates the comparison between experiment and theory as a function of perpendicular electric field, is to take the theoretical value for the effective mass $m^* = 0.052m_0$ and plot together the values obtained for $\delta\varepsilon$ in the two different ways (that is, by looking at the temperature dependence of the maximum resistance, or by simply looking at its value at 50 mK). The result of this comparison as a function of E_{ext} is presented in Fig. 4.4a, which shows a remarkable agreement throughout the entire E_{ext} range. Note that, at $E_{ext} = 0$ we obtain $\delta\varepsilon = 32$ meV from the temperature dependence and $\delta\varepsilon = 34$ meV from the data at 50 mK, close to the value $\delta\varepsilon \approx 28$ meV already obtained earlier by analysing the gate voltage dependence of the Hall resistance (Fig. 4.1d; the error on the values for $\delta\varepsilon$ obtained with the different methods is between 10 and 20 %).

4.5 CONCLUSIONS AND DISCUSSION

Finding that three different methods used to estimate the band overlap result in values that are in quantitative agreement with each other provides a clear indication of the validity of our analysis, and confirms that the experiments are probing the intrinsic electronic properties of trilayer graphene. This conclusively demonstrates that the low-energy band structure of trilayer graphene can be tuned by a large amount through the application of an external perpendicular electric field, achieving a 100 % change in band overlap. A similar electric field tunable $\delta\varepsilon$ was experimentally observed in all devices investigated, albeit with a spread (about 30 %) in the value of external field needed to induce a same shift of the band overlap in different devices. We attribute these differences in the precise electric field value to screening due to unwanted adsorbed layers present at the SiO_2/graphene interfaces (for example, water or hydrocarbons).

Having established that the band structure of trilayer graphene differs significantly from that of single and double layers due to the presence of an overlap between valence and conduction band, it is also interesting to look at the evolution of the carrier mobility in these materials. A comparison of the mobility values measured in graphene layers of different thickness is shown in Fig. 4.5a. It is apparent that trilayer graphene systematically exhibits lower mobility (typically ~800 cm^2/Vs at 4.2 K) than single-layer and bilayer graphene. The trend originates in large part from the difference in the effective mass in the different materials, which increases with increasing layer thickness ($m^*_{SG} = 0$, $m^*_{BG} = 0.037m_0$, and $m^*_{TG} = 0.052m_0$) (ref. [30]). The observation of this trend, together with the different response to a perpendicular electric field and the differences in the low-energy band structure discussed above, show that every individual graphene multilayer sequence is a new material in its own right. Regarding the low-energy electronic properties it is unclear whether a 'smooth' evolution from graphene to graphite can be expected as the number of layers is increased. Our results suggest that for systems consisting of only a few layers, this evolution with thickness may be dominated by unique aspects specific to each layer thickness. In trilayer graphene, one such unique property is the possibility to tune the band overlap electrostatically, over a large range.

4.6 REFERENCES

1. Novoselov, K. S. et al., Electric field effect in atomically thin carbon films, Science 306, 666-669 (2004).
2. Novoselov, K. S. et al., Two-dimensional gas of massless Dirac fermions in graphene, Nature 438, 197-200 (2005).
3. Zhang, Y. B. et al., Experimental observation of the quantum Hall effect and Berry's phase in graphene, Nature 438, 201-204 (2005).
4. Geim, A. K. & Novoselov, K. S., The rise of graphene, Nature Mater. 6, 183-191 (2007).
5. Tombros, N. et al., Electronic spin transport and spin precession in single graphene layers at room temperature, Nature 448, 571-574 (2007).
6. Williams, J. R., DiCarlo, L. & Marcus, C. M., Quantum Hall effect in a gate-

controlled p-n junction of graphene, Science 317, 638-641 (2007).
7. Ponomarenko, L. A. et al., Chaotic Dirac billiard in graphene quantum dots, Science 320, 356-358 (2008).
8. Meric, I. et al., Current saturation in zero-bandgap, top-gated graphene field-effect transistors, Nature Nanotech. 3, 654-659 (2008).
9. Novoselov, K. S. et al., Unconventional quantum Hall effect and Berry's phase of 2π in bilayer graphene, Nature Phys. 2, 177-180 (2006).
10. Oostinga, J. B. et al., Gate-induced insulating state in bilayer graphene devices, Nature Mater. 7, 151-157 (2008).
11. Castro, E. V. et al., Biased bilayer graphene: Semiconductor with a gap tunable by the electric field effect, Phys. Rev. Lett. 99, 216802 (2007).
12. Ohta, T., Bostwick, A., Seyller, T., Horn, K. & Rotenberg, E., Controlling the electronic structure of bilayer graphene, Science 313, 951-954 (2006).
13. Guettinger, J. et al., Coulomb oscillations in three-layer graphene nanostructures, New J. Phys. 10, 125029 (2008).
14. Schedin, F. et al., Detection of individual gas molecules adsorbed on graphene, Nature Mater. 6, 652-655 (2007).
15. Bolotin, K. I. et al., Ultrahigh electron mobility in suspended graphene, Solid State Commun. 146, 351-355 (2008).
16. Sugihara, K., Kawamura, K. & Tsuzuku, T., Temperature dependence of the average mobility in graphite, J. Phys. Soc. Jpn 47, 1210-1215 (1979).
17. Dreselhaus, M. S. & Dresselhaus, G., Intercalation compounds of graphite, Adv. Phys. 30, 139-326 (1981).
18. Chen, J. H., Jang, C., Xiao, S., Ishigami, M. & Fuhrer, M. S., Intrinsic and extrinsic performance limits of graphene devices on SiO_2, Nature Nanotech. 3, 206-209 (2008).
19. Guinea, F., Castro Neto, A. H. & Peres, N. M. R., Electronic states and Landau levels in graphene stacks, Phys. Rev. B 73, 245426 (2006).
20. Latil, S. & Henrard, L., Charge carriers in few-layer graphene films, Phys. Rev. Lett. 97, 036803 (2006).
21. Partoens, B. & Peeters, F. M., From graphene to graphite: Electronic structure around the K point, Phys. Rev. B 74, 075404 (2006).
22. Lu, C. L. et al., Influence of an electric field on the optical properties of few-layer graphene with AB stacking, Phys. Rev. B 73, 144427 (2006).
23. Aoki, M. & Amawashi, H., Dependence of band structures on stacking and field in layered graphene, Solid State Commun. 142, 123-127 (2007).
24. McCann, E., Asymmetry gap in the electronic band structure of bilayer graphene, Phys. Rev. B 74, 161403 (2006).
25. Min, H., Sahu, B. R., Banerjee, S. K. & MacDonald, A. H., Ab initio theory of gate induced gaps in graphene bilayers, Phys. Rev. B 75, 155115 (2007).

26. Russo, S., Craciun, M. F., Yamamoto, M., Morpurgo, A. F. & Tarucha, S., Contact resistance in graphene-based devices, arXiv:0901.0485 (2009).
27. McClure, J. W., Band structure of graphite and de Haas-van Alphen effect, Phys. Rev. 108, 612-618 (1957).
28. Slonczewski, J. C. & Weiss, P. R., Band structure of graphite, Phys. Rev. 109, 272-279 (1958).
29. Koshino, M. & McCann, E., Gate-induced interlayer asymmetry in ABA-stacked trilayer graphene, Phys. Rev. B 79, 125443 (2009).
30. Koshino, M. & Ando, T., Orbital diamagnetism in multilayer graphenes: Systematic study with the effective mass approximation, Phys. Rev. B 76, 085425 (2007).
31. Klein, C. A., STB model and transport properties of pyrolytic graphite, J. Appl. Phys. 35, 2947-2957 (1964).
32. Ohta, T. et al., Interlayer interaction and electronic screening in multilayer graphene investigated with angle-resolved photoemission spectroscopy, Phys. Rev. Lett. 98, 206802 (2007).

5

BIPOLAR SUPERCURRENT IN GRAPHENE

Graphene – a recently discovered form of graphite only one atomic layer thick [1] – constitutes a new model system in condensed matter physics, because it is the first material in which charge carriers behave as massless chiral relativistic particles. The anomalous quantization of the Hall conductance [2,3], which is now understood theoretically [4,5], is one of the experimental signatures of the peculiar transport properties of relativistic electrons in graphene. Other unusual phenomena, like the finite conductivity of order $4e^2/h$ *(where* e *is the electron charge and* h *is Planck's constant) at the charge neutrality (or Dirac) point [2], have come as a surprise and remain to be explained [5-13]. Here we experimentally study the Josephson effect [14] in mesoscopic junctions consisting of a graphene layer contacted by two closely spaced superconducting electrodes [15]. The charge density in the graphene layer can be controlled by means of a gate electrode. We observe a supercurrent that, depending on the gate voltage, is carried by either electrons in the conduction band or by holes in the valence band. More importantly, we find that not only the normal state conductance of graphene is finite, but also a finite supercurrent can flow at zero charge density. Our observations shed light on the special role of time reversal symmetry in graphene, and demonstrate phase coherent electronic transport at the Dirac point.*

The contents of this chapter have been published in *Nature*
H. B. Heersche, P. Jarillo-Herrero, J. B. Oostinga, L. M. K. Vandersypen, A. F. Morpurgo, *Bipolar supercurrent in graphene.* Nature **446** (7131), 56-59 (2007).

5.1 INTRODUCTION

Owing to the Josephson effect [14,16], a supercurrent can flow through a normal conductor placed between two closely spaced superconducting electrodes. For this to happen, transport in the normal conductor must be phase coherent and time reversal symmetry (TRS) must be present. In graphene, the Josephson effect can be investigated in the ’relativistic’ regime [15], where the supercurrent is carried by Dirac electrons. However, it is not clear a priori that graphene can support supercurrents, because other quantum interference phenomena that require both phase coherence and TRS were found to be absent or strongly suppressed in previous experiments [17]. Below we show experimentally that the Josephson effect in graphene is a robust phenomenon, and argue that its robustness is intimately linked to graphene’s unique electronic structure.

5.2 DEVICE FABRICATION AND CHARACTERIZATION

Single- and few-layer graphene Josephson junctions are fabricated on oxidized Si substrates by mechanical exfoliation of bulk graphite [1], followed by optical microscope inspection to locate the thinnest graphitic flakes, and electron beam lithography to define electrical contacts. Figure 5.1a shows an atomic force microscope image of a typical device. We use as superconducting contacts a Ti/Al bilayer (10/70 nm). Titanium ensures good electrical contact to graphene, and Al establishes a sufficiently high critical temperature to enable the observation of supercurrents in a dilution refrigeration set-up [18]. Before discussing their superconducting properties, we first characterize the devices with the superconducting electrodes in the normal state. Figure 5.1c shows the two-terminal resistance, R, versus gate voltage, V_G, for one of our samples. The strong V_G-dependence of R provides a first indication that the device consists of at most a few layers of graphene [1], since, owing to screening, V_G affects the carrier density only in the bottom one or two layers. For single layers, the position of the resistance maximum corresponds to the gate voltage at which the Fermi energy is located at the Dirac point, V_D, and we typically find that $|V_D| < 20$ V. We unambiguously determine the single layer character of a device by quantum Hall effect (QHE) measurements. Because the superconducting proximity effect requires two closely spaced electrodes, we can only perform magnetoconductance measurements in a two terminal configuration. In general, the conductance, G, measured in this way is a mixture of longitudinal and Hall signals, but at high fields $G \approx |G_{Hall}|$ (this approximation is exact at the Hall plateaus [19]). Indeed, the measurement of G versus V_G at $B = 10$ T shows clearly identifiable Hall plateaus at half-integer multiples of $4e^2/h$ (Fig. 5.1d), characteristic of the QHE in single layer graphene [2,3]. This demonstrates that, even in mesoscopic samples, the QHE can be used to identify single layer

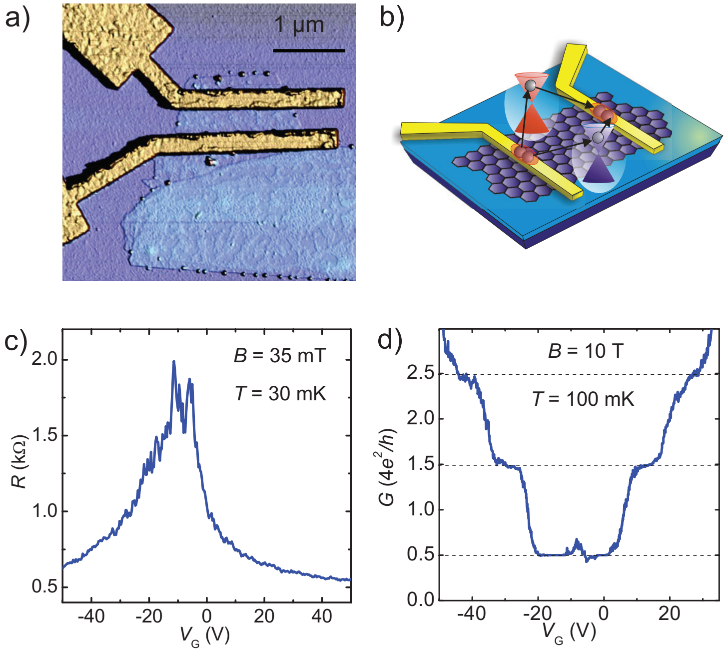

FIGURE 5.1: **Sample characterization.** a, Atomic force microscope image of a single layer graphene device between two superconducting electrodes. We have fabricated devices with electrode separations in the range 100-500 nm. b, Schematic representation of graphene between superconducting electrodes. The two electrons in a Cooper pair entering graphene go into different K-valleys, represented by the red and blue cones (see text). c, Two-terminal resistance versus gate voltage, V_G, at $T = 30$ mK and a small magnetic field, $B = 35$ mT, to drive the electrodes into the normal state. The aperiodic conductance fluctuations are due to random quantum interference of electron waves (see also Fig. 5.5). d, Two terminal conductance, G, versus V_G at high magnetic field, $B = 10$ T, and $T = 100$ mK, showing a series of steps at half-integer values of $4e^2/h$, characteristic of the anomalous QHE in single layer graphene.

devices.

5.3 OBSERVATION OF INDUCED SUPERCONDUCTIVITY

Cooling down the devices below the critical temperature of the electrodes ($T_c \approx 1.3$ K) leads to proximity-induced superconductivity in the graphene layer. A direct proof of induced superconductivity is the observation of a Josephson supercurrent [20]. Figure 5.2a shows the current-voltage (I-V) characteristics of a single layer device. The current flows without resistance (no voltage drop at finite current) below the critical current, I_c (what we actually measure is the switching current; the intrinsic I_c may be higher [20,21]). In our devices, I_c ranged from ~10 nA to more than 800 nA (at high V_G). Remarkably, we have measured proximity-induced supercurrents in all the devices that we tested (17 flakes in total, with several devices on some flakes), including four flakes that were unambiguously identified as single layer graphene via QHE (the rest being probably two to four layers thick). This clear observation demonstrates the robustness of the Josephson effect in graphene junctions. (The data shown are representative of the general behaviour observed; the measurements shown in Figs 5.1, 5.2a,c,d and 5.4 have been taken on the same device, whereas those in Figs 5.2b and 5.5 correspond to a different single layer device, shown in Fig. 5.1a.)

To investigate further the superconducting properties of our devices, we measured the dependence of I_c on magnetic field (Fig. 5.2b). The critical current exhibits an oscillatory Fraunhofer-like pattern, with at least six visible side lobes, which is indicative of a uniform supercurrent density distribution [22]. The periodicity of the oscillations is in the ideal case expected to be equal to a flux quantum Φ_0 divided by the junction area. The area that corresponds to the 2.5 ± 0.5 mT period is $0.8 \pm 0.2\ \mu\text{m}^2$, which is in good agreement with the measured device area ($0.7 \pm 0.2\ \mu\text{m}^2$) determined from the atomic force microscope image. Applying a radio-frequency field to the sample results in the observation of quantized voltage steps, known as Shapiro steps, in the I-V characteristics [20]. The voltage steps, of amplitude $\hbar\omega/2e$ (ω is the microwave frequency), are a manifestation of the a.c. Josephson effect, and are evident in Fig. 5.2d.

The induced superconductivity manifests itself also at finite bias in the form of subgap structure in the differential resistance due to multiple Andreev reflections [23], as shown in Fig. 5.2c. This subgap structure consists of a series of minima at source-drain voltages $V = 2\Delta/en$ ($n = 1,2...$), which enables us to determine the superconducting gap, Δ. We find Δ = 125 meV, as expected for our Ti/Al bilayers [18]. Figure 5.3 shows that the position of the minima is essentially independent of the gate voltage. The sharpness of the features associated to multiple Andreev reflection, on the contrary, does depend on gate voltage. Although we have not

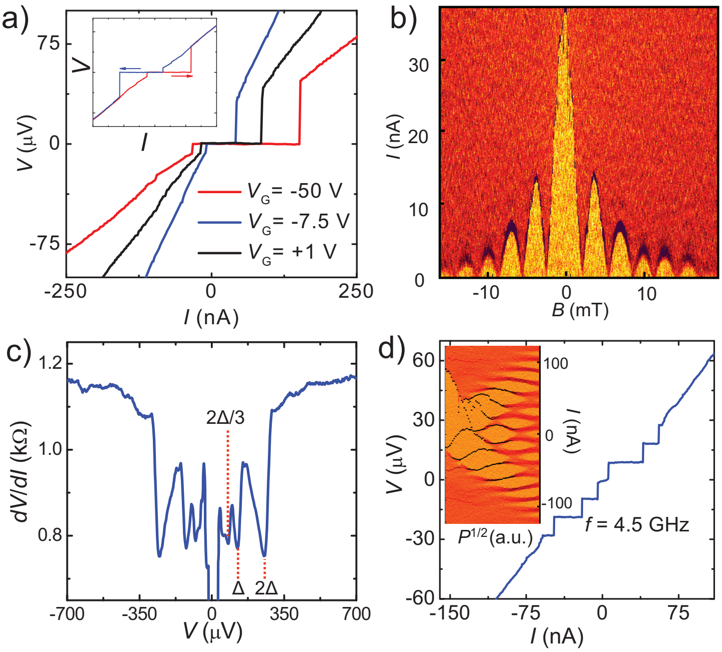

FIGURE 5.2: **Josephson effect in graphene.** a, Voltage, V, versus current bias, I, characteristics at various V_G, showing a modulation of the critical current. Inset, current bias sweeps from negative to positive (red) and vice versa (blue), showing that the asymmetry in the main panel is due to hysteretic behaviour (the retrapping current is smaller than the switching current, as is typical for an underdamped junction). b, Colour-scale representation of $dV/dI(I,B)$ at $T = 30$ mK (yellow-orange is zero, that is, the supercurrent region, and red corresponds to finite dV/dI). The critical current exhibits a series of oscillations described by a Fraunhofer-like pattern. c, Differential resistance, dV/dI, versus V, showing multiple Andreev reflection dips below the superconducting energy gap. The dips in dV/dI occur at values of $V = 2\Delta/en$, where n is an integer number. d, a.c. Josephson effect. The Shapiro steps in the I-V characteristics appear when the sample is irradiated with microwaves. In the example, we applied 4.5 GHz microwaves, resulting in 9.3 mV voltage steps. Inset, colour-scale plot showing the characteristic microwave amplitude ($P^{1/2}$; a.u., arbitrary units) dependence of the a.c. Josephson effect (orange and red correspond respectively to zero and finite dV/dI).

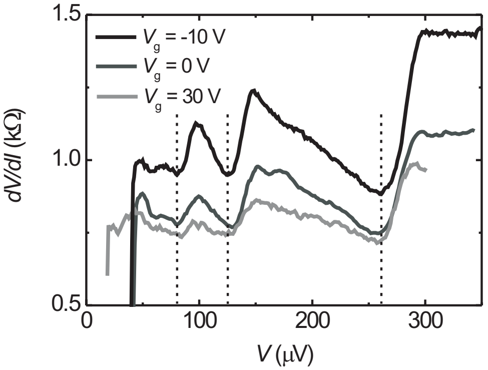

FIGURE 5.3: **Subgap structure.** The differential resistance, dV/dI, versus the voltage bias measured at different gate voltages (the charge neutrality point is around V_g = -10 V). The traces show multiple Andreev reflection dips at voltages below twice the superconducting gap (T = 30 mK).

performed a fully quantitative analysis, it appears that these features are sharper when the gate voltage is close to the charge neutrality point, in qualitative agreement with recent theoretical calculations [24]. For $V > 2\Delta/e$, the differential resistance returns to the normal state value. From the suppression of the differential resistance observed while changing the bias from above to below the gap, we can estimate that the average transparency of the superconductor–graphene interface is ~0.7-0.8.

5.4 BIPOLAR SUPERCURRENT

Having established the existence of the Josephson effect in graphene, we analyse the gate voltage dependence of the critical current. Figure 5.2a shows several I-V traces taken at different V_G, where it can already be seen that varying the gate voltage has a strong effect on the maximum supercurrent flowing through the device. This behaviour can be more readily seen in Fig. 5.4a, where the differential resistance is plotted as a function of current bias and gate voltage. By changing V_G we can continuously shift the Fermi energy from the valence band ($V_G < V_D$) to the conduction band ($V_G > V_D$): irrespective of the sign of V_G, we find a finite supercurrent. This demonstrates that the devices operate as bipolar supercurrent transistors: the supercurrent is carried by hole Cooper pairs when the Fermi level is in the valence band and by electron Cooper pairs when it is in the conduction band. Note that in going from valence to conduction band, we sweep the posi-

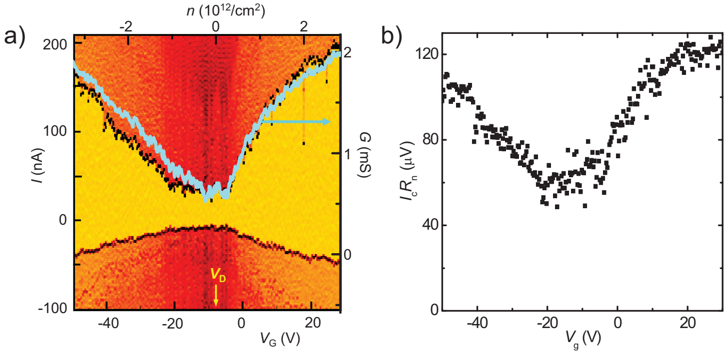

FIGURE 5.4: **Bipolar supercurrent transistor behaviour and finite supercurrent at the Dirac point.** a, Colour-scale plot of $dV/dI(V_G, I)$. Yellow means zero, that is, the supercurrent region, and finite dV/dI increases via orange to dark red. The current is swept from negative to positive values, and is asymmetric owing to the hysteresis associated with an underdamped junction (see also Fig. 5.2a inset). The top axis shows the electron density, n, as obtained from geometrical considerations [1]. For large negative (positive) V_G the supercurrent is carried by hole (electron) Cooper pairs. The supercurrent at the Dirac point (V_D) is finite. Note that the critical current is not symmetric with respect to V_D. The origin of this asymmetry is not known, but a similar asymmetry is seen in the normal state conductance (blue curve). b, Product of the critical current times the normal state resistance versus V_G. The normal state resistance is measured at zero source-drain bias, at $T = 30$ mK and with a small magnetic field to drive the electrodes into the normal state. The I_cR_n product exhibits a dip around the Dirac point (see main text).

tion of the Fermi level through the Dirac point. Strikingly, even then the supercurrent remains finite, despite the fact that for perfect graphene theory predicts [25] a vanishing density of states at $V_G = V_D$. This behaviour has been observed in all samples, and demonstrates that electronic transport in graphene is phase coherent irrespective of the gate voltage, including when the Fermi level is located at the Dirac point.

In conventional Josephson junctions, the critical current correlates with the normal state conductance, G_n (ref. [26]). In graphene this correlation can be observed directly, as shown in Fig. 5.4a, because both I_c and G_n depend on V_G. To analyse this correlation, we plot the product of the measured critical current and the normal state resistance ($R_n = 1/G_n$), or I_cR_n product (see Fig. 5.4b). We find that at high gate voltage $I_cR_n \approx \Delta/e$, and that I_cR_n is suppressed by a factor of 2-3 around the Dirac point. The observed I_cR_n product is thus close to the theoretical value of $\sim 2.5\Delta/e$ for a model system of graphene in the ballistic regime [15]. The remaining discrepancy may be accounted for by the difference between the measured critical current (or switching current) and the intrinsic critical current [20,21]. This difference is in general hard to quantify and depends on the electro-

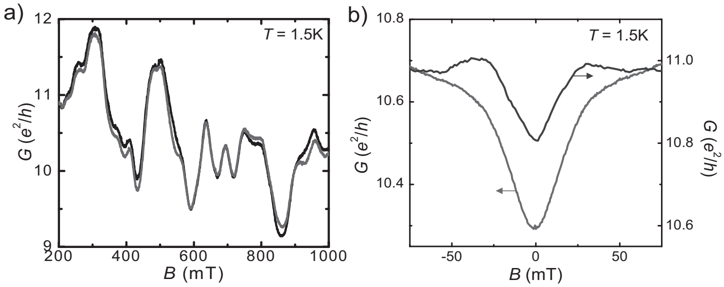

FIGURE 5.5: **Magnetoconductance measurements.** a, Conductance versus magnetic field at $T \approx 1.5$ K for a single layer device at $V_G = V_D$. The gray and black traces are two subsequent measurements, showing reproducible conductance fluctuations, whose root mean square amplitude is e^2/h. b, Low field magnetoconductance measured at $T \approx 1.5$ K (electrodes in the normal state) for two different single layer devices (the gray trace corresponds to the device measured in (a), showing that the amplitude of the weak localization effect is sample dependent and suppressed as compared to the expected value, $\sim e^2/h$. Each curve results from an ensemble average of 66 individual magnetoresistance measurements taken at different gate voltages near the Dirac point.

magnetic environment of the sample, but it is expected to be more pronounced when I_c itself is smaller (that is, at low V_G), and could thus well explain the observed V_G dependence of $I_c R_n$.

5.5 PHASE COHERENCE AND TIME REVERSAL SYMMETRY

An interesting aspect of supercurrent in graphene is the special role of time reversal symmetry in the Josephson effect compared to that in phase coherent transport in the normal state. At low energy, the band structure of graphene consists of two identical, independent valleys centred on the so-called K and K' points [25], which transform into each other under time reversal. As Cooper pairs are made out of time reversed electron states, the two electrons in Cooper pairs that are injected from the superconducting electrodes into graphene go to opposite K-points [15] (see Fig. 5.1b). In this way, the presence of a superconducting electrode provides an intrinsic mechanism that couples phase coherently electronic states belonging to opposite valleys. The dynamics of electrons is then described by the full (two-valley) Hamiltonian of graphene that is time reversal symmetric.

The situation is very different for normal-state transport where the dynamics of the electrons is determined by a 'one-valley' Hamiltonian. This has important consequences not only for the QHE [4,5], but also for quantum interference. When the two valleys are fully decoupled, interference originating from coherent propagation of electrons along time reversed trajectories cannot occur, as these trajectories

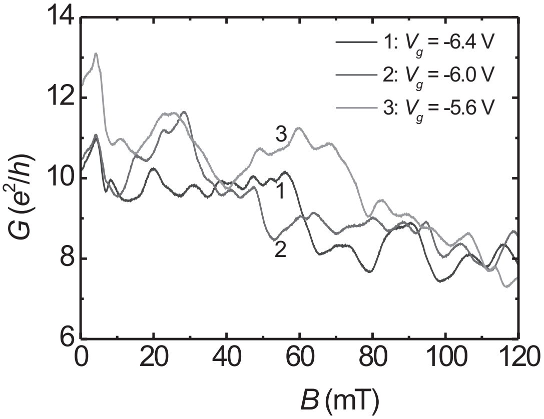

FIGURE 5.6: **Aperiodic conductance fluctuations.** Two-terminal magnetoconductance measured at T = 1.6 K, for small values of the applied magnetic field B, exhibiting aperiodic conductance fluctuations for different values of the gate voltage near the Dirac point. The features of these conductance fluctuations, which depend on the applied gate voltage, are reproducible at fixed gate voltage.

involve quantum states from opposite K-points. As a consequence, quantum corrections to the conductivity, like weak localization, would be absent (note that for the single-valley Hamiltonian there exists an effective TRS in the long wavelength limit, but in real samples this symmetry is easily broken [27-29]). The contribution of time-reversed trajectories to quantum interference can be restored only up to the extent that there exists a coupling mechanism between the two valleys, such as short-range scattering at impurities or at the graphene edges [27-29]. This makes the occurrence of weak localization dependent on extrinsic defects, which explains why both in our own samples (see Fig. 5.5b) and other recent measurements [17,30] weak localization is found to exhibit a surprising sample dependent behaviour and is often suppressed (while, at the same time, we observe a supercurrent in all samples investigated). This interpretation, which illustrates the unique electronic properties of graphene, is consistent with the observation of aperiodic conductance fluctuations [31] of amplitude e^2/h (see Fig. 5.5a), whose occurrence requires phase coherence but not time reversal symmetry.

Figure 5.6 shows the magnetoresistance of one of our devices for different values of gate voltage in the range (-5 V, -7 V), which corresponds to sweeping the Fermi level across the Dirac point. The presence of aperiodic conductance fluctuations is apparent. The characteristic correlation field is approximately 5-10 mT, that compares well to the expected value of h/eS (where S is the area of the device). At this temperature (T = 1.3 K), the root mean square amplitude of these fluctuations is smaller than e^2/h, but we also observed that the amplitude of the aperiodic conductance fluctuations increases with lowering T (at $T = 20$ mK, we measured aperiodic conductance fluctuations by applying a magnetic field larger than the critical field of the superconducting electrodes), resulting in root mean square values $\approx e^2/h$ at $T = 20$ mK. Similar measurements performed in a few different samples gave comparable, consistent results. Although a more systematic study as a function of gate voltage and temperature remains to be done, the results of our experiments allow us to conclude that aperiodic conductance fluctuations are indeed present in graphene even when the Fermi level is at or near the Dirac point, and that their magnitude is close to what one would expect for conventional mesoscopic conductors. The comparative study of Josephson supercurrent, weak localization, and aperiodic conductance fluctuations consistently point to the fact that transport in graphene is phase coherent irrespective of the position of the Fermi level, i.e. whether the Fermi level is near or far away from the Dirac point.

5.6 REFERENCES

1. Novoselov, K. S. et al., Electric field effect in atomically thin carbon films, Science 306, 666-669 (2004).
2. Novoselov, K. S. et al., Two-dimensional gas of massless Dirac fermions in graphene, Nature 438, 197-200 (2005).
3. Zhang, Y. B., Tan, Y. W., Stormer, H. L. & Kim, P., Experimental observation of the quantum Hall effect and Berry's phase in graphene, Nature 438, 201-204 (2005).
4. Gusynin, V. P. & Sharapov, S. G., Unconventional integer quantum Hall effect in graphene, Phys. Rev. Lett. 95, 146801 (2005).
5. Peres, N. M. R., Guinea, F. & Castro Neto, A. H., Electronic properties of disordered two-dimensional carbon, Phys. Rev. B 73, 125411 (2006).
6. Fradkin, E., Critical-behavior of disordered degenerate semiconductors. II. Spectrum and transport properties in mean-field theory, Phys. Rev. B 33, 3263-3268 (1986).
7. Ludwig, A. W. W., Fisher, M. P. A., Shankar, R. & Grinstein, G., Integer quantum Hall transition - an alternative approach and exact results, Phys. Rev. B 50, 7526-7552 (1994).
8. Nersesyan, A. A., Tsvelik, A. M. & Wenger, F., Disorder effects in 2-dimensional d-wave superconductors, Phys. Rev. Lett. 72, 2628-2631 (1994).
9. Altland, A., Simons, B. D. & Zirnbauer, M. R., Theories of low-energy quasiparticle states in disordered d-wave superconductors, Phys. Rep. 359, 283-354 (2002).
10. Katsnelson, M. I., Zitterbewegung, chirality, and minimal conductivity in gra-

phene, Eur. Phys. J. B 51, 157-160 (2006).
11. Nomura, K. & MacDonald, A. H., Quantum transport of massless Dirac fermions in graphene, Phys. Rev. Lett 98, 076602 (2007).
12. Aleiner, I. L. & Efetov, K. B., Effect of disorder on transport in graphene, Phys. Rev. Lett. 97, 236801 (2006).
13. Altland, A., Low energy theory of disordered graphene, Phys. Rev. Lett. 97, 236802 (2006).
14. Josephson, B. D., Possible new effects in superconductive tunnelling, Phys. Lett. 1, 251-253 (1962).
15. Titov, M. & Beenakker, C. W. J., The Josephson effect in ballistic graphene, Phys. Rev. B 74, 041401(R) (2006).
16. Degennes, P. G., Boundary effects in superconductors, Rev. Mod. Phys. 36, 225-237 (1964).
17. Morozov, S. V. et al., Strong suppression of weak localization in graphene, Phys. Rev. Lett. 97, 016801 (2006).
18. Jarillo-Herrero, P., van Dam, J. A. & Kouwenhoven, L. P., Quantum supercurrent transistors in carbon nanotubes, Nature 439, 953-956 (2006).
19. Datta, S., Electronic Transport in Mesoscopic Systems (Cambridge Univ. Press, Cambridge, UK, 1995).
20. Tinkham, M., Introduction to Superconductivity (McGraw-Hill, Singapore, 1996).
21. Joyez, P., Lafarge, P., Filipe, A., Esteve, D. & Devoret, M. H., Observation of parity induced suppression of Josephson tunneling in the superconducting single electron transistor, Phys. Rev. Lett. 72, 2458-2461 (1994).
22. Barone, A. & Paterno, G., Physics and Applications of the Josephson Effect (Wiley & Sons, New York, 1982).
23. Octavio, M., Tinkham, M., Blonder, G. E. & Klapwijk, T. M., Subharmonic energy-gap structure in superconducting constrictions, Phys. Rev. B 27, 6739-6746 (1983).
24. Cuevas, J. C. & Yeyati, A. L., Subharmonic gap structure in short ballistic graphene junctions, Phys. Rev. B 74, 180501 (2006).
25. Dresselhaus, M. S., Dresselhaus, G. & Eklund, P. C., Science of Fullerenes and Carbon Nanotubes (Academic, San Diego, 1996).
26. Likharev, K. K., Superconducting weak links, Rev. Mod. Phys. 51, 101-159 (1979).
27. Morpurgo, A. F. & Guinea, F., Intervalley scattering, long-range disorder, and effective time reversal symmetry breaking in graphene, Phys. Rev. Lett. 97, 196804 (2006).
28. Suzuura, H. & Ando, T., Crossover from symplectic to orthogonal class in a two-dimensional honeycomb lattice, Phys. Rev. Lett. 89, 266603 (2002).
29. McCann, E. et al., Weak localisation magnetoresistance and valley symmetry in graphene, Phys. Rev. Lett. 97, 146805 (2006).

30. Berger, C. et al., Electronic confinement and coherence in patterned epitaxial graphene, Science 312, 1191-1196 (2006).
31. Lee, P. A. & Stone, A. D., Universal conductance fluctuations in metals, Phys. Rev. Lett. 55, 1622-1625 (1985).

6

AHARONOV-BOHM EFFECT IN GRAPHENE

We investigate experimentally transport through ring-shaped devices etched in graphene and observe clear Aharonov-Bohm conductance oscillations. The temperature dependence of the oscillation amplitude indicates that below 1 K, the phase coherence length is comparable to or larger than the size of the ring. An increase in the amplitude is observed at high magnetic field, when the cyclotron diameter becomes comparable to the width of the arms of the ring. By measuring the dependence on gate voltage, we find that the Aharonov-Bohm effect vanishes at the charge neutrality point, and we observe an unexpected linear dependence of the oscillation amplitude on the ring conductance.

The contents of this chapter have been published in *Physical Review B*:
S. Russo, J. B. Oostinga, D. Wehenkel, H. B. Heersche, S. Shams Sobhani, L. M. K. Vandersypen, A. F. Morpurgo, *Observation of Aharonov-Bohm conductance oscillations in a graphene ring*. Physical Review B **77** (8), 085413 (2008).

6.1 INTRODUCTION

The investigation of transport phenomena originating from quantum interference of electronic waves has proven to be a very effective probe of the electronic properties of conducting materials. Recent work has shown that this is also the case for graphene, a novel material consisting of an individual layer of carbon atoms, in which the electron dynamics is governed by the Dirac equation [1]. The anomalous behavior of the weak-localization correction to the conductivity that is observed in the experiments [2], for instance, is directly related to the presence of two independent valleys in the band structure of graphene [3,4] and can be used to extract the intervalley scattering time [5]. Another example is provided by the observation of a Josephson supercurrent in graphene superconducting junctions, which permits to conclude that transport through graphene is phase coherent even when the material is biased at the charge neutrality point (i.e., where nominally no charge carriers are present) [6].

Possibly, the phenomenon that most directly illustrates electronic interference in solid-state devices is the occurrence of periodic oscillations in the conductance of ring-shaped devices, measured as a function of magnetic field [7]. This phenomenon, which is a direct consequence of the Aharonov-Bohm (AB) effect, has been investigated extensively in the past in rings made with metallic films or with semiconducting heterostructures, and its study has contributed significantly to our understanding of mesoscopic physics. For example, the analysis of h/e and $h/2e$ AB conductance oscillations has clarified the difference between sample-specific and ensemble-averaged phenomena [7]. The investigation of the temperature and magnetic field dependences of the oscillation amplitudes has been used to investigate processes leading to decoherence of electron waves, such as electron-electron interaction [7,8], or the interaction with magnetic impurities [9]. In graphene, however, no experimental observation of AB conductance oscillations has been reported so far, although there is an emerging interest in the problem from the theoretical side [10,11]. In the course of recent experiments, we have observed AB conductance oscillations experimentally in several rings fabricated on few-layer graphene. In this paper, we report on systematic measurements that we have performed on a device made on single-layer graphene as a function of temperature, density of charge carriers, and magnetic field.

6.2 DEVICE FABRICATION

The devices used in our experiments were fabricated following a by now established procedure [12]. Thin graphite flakes were exfoliated from natural graphite using an adhesive tape and transferred onto a highly doped Si substrate (acting as a gate) covered by a 300 nm thick SiO_2 layer. The flakes were imaged under an op-

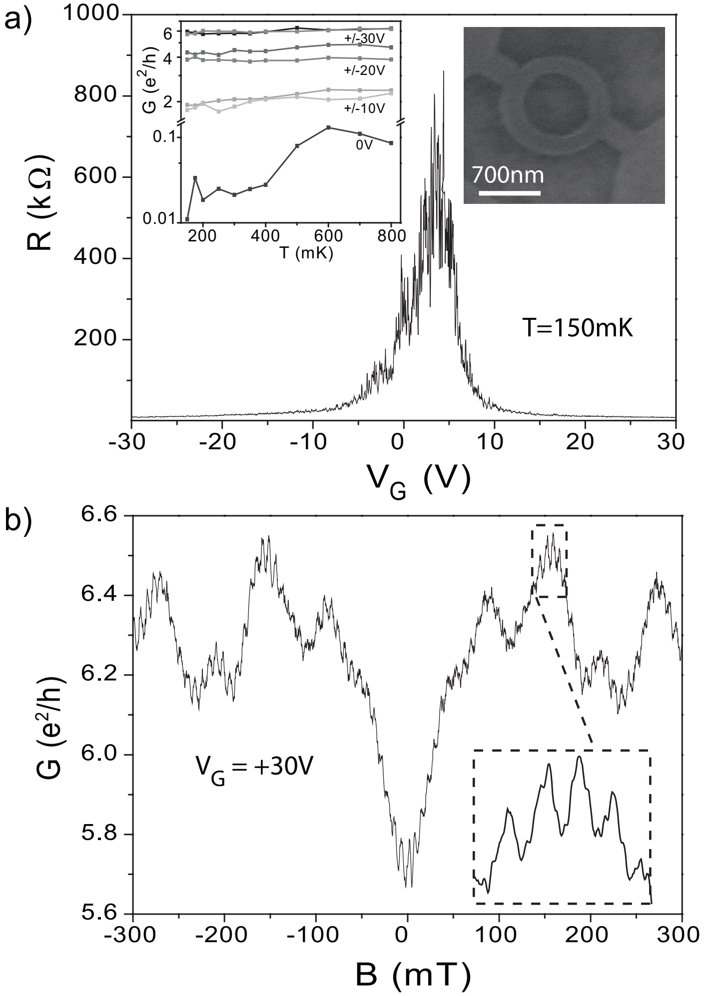

FIGURE 6.1: (a) The main panel shows the two-probe measurement of the ring resistance versus back-gate voltage at T = 150 mK. The charge neutrality point is at +4 V. Left inset: temperature dependence of the conductance measured for different values of gate voltage. Right inset: scanning electron microscopy image of a ring-shaped device etched in graphene similar to the one used in our measurements. (b) Magnetoconductance of the graphene ring measured at T = 150 mK and V_G = +30 V. On top of the aperiodic conductance fluctuations, periodic oscillations are clearly visible as also highlighted in the inset.

tical microscope and their position was registered with respect to markers already present on the substrates. Single layer flakes were identified by looking at the shift of the light intensity in the green channel of the red-green-blue scale relative to the adjacent substrate (see §2.7 and Ref. [13]). In subsequent nanofabrication steps, the devices were patterned using electron-beam lithography to define pairs of metallic electrodes (Ti/Au) and to etch the rings in an argon plasma. The rings have inner and outer radii of 350 and 500 nm, respectively; the inset of Fig. 6.1a shows a scanning electron micrograph of a typical device.

Measurements were performed in a dilution refrigerator in the temperature range between 150 and 800 mK. The conductance of the ring was measured using a lock-in amplifier in a current-biased two-terminal configuration. For the different measurements, the excitation current was varied to ensure that resulting voltage was smaller than the temperature to prevent heating of the electrons and the occurrence of nonequilibrium effects.

6.3 CHARACTERIZATION OF THE GRAPHENE RING

Figure 6.1a shows the resistance of the ring measured at $T = 150$ mK as a function of gate voltage. A clear peak, centered at approximately $V_G = +4$ V, is observed as it is typical for graphene. The large peak resistance value may be expected since the rings are made of fairly narrow ribbons (~150 nm). It may originate either from the opening of a small gap due to lateral size quantization (as recently proposed [14]) or from the fact that, close to the charge neutrality point, disorder at the edges is not screened effectively, resulting in enhanced scattering with valley mixing and localization of electron states. To estimate the mobility μ of charge carriers, we use the value of the conductance per square measured at high gate voltage. With the density of charge carriers being determined from the known capacitance to the gate (i.e., $G_{\square} = ne\mu = \epsilon_0 \epsilon_r e\mu V_G/d$), we obtain $\mu = 6000$ cm^2/Vs, essentially independent of V_G for $V_G > 10$ V and $V_G <$ -10 V. The diffusion constant is estimated from the Einstein relation $\sigma = \nu e^2 D$, where σ is the measured conductivity and ν the density of states at the Fermi level, which for graphene is given by $\nu(\varepsilon_F) = g_v g_s 2\pi|\varepsilon_F|/(h^2 v_F^2)$ [15]. Here, $g_v = 2$ and $g_s = 2$ account for the valley and spin degeneracies, $v_F = 10^6$ m/s is the Fermi velocity, and the value of ε_F is determined by equating the expression for the charge density $n(\varepsilon_F) = g_v g_s \pi \varepsilon_F^2/(h^2 v_F^2)$ to the value determined by the gate voltage. We obtain $D = 0.06$ m^2/s, not far from the value of diffusion constant that is estimated assuming diffusive scattering at the ribbon edges ($D = W v_F = 0.15$ m^2/s, with W the width of the ribbon). With this value of the diffusion constant, we obtain a Thouless energy for the ring of $E_{Th} = \hbar D/L^2 = 10$ μeV (L is the ring circumference), which is slightly smaller than the lowest temperature ($T = 150$ mK) at which the measurements have been performed.

6.4 AB-EFFECT AT LOW MAGNETIC FIELD

The low-field magnetoresistance measured at $V_G = 30$ V and $T = 150$ mK is shown in Fig. 6.1b. The presence of periodic oscillations is clearly visible. The period in field is approximately $B = 7$ mT and the corresponding Fourier spectrum is shown in Fig. 6.2b. In the spectrum, a peak is present, whose position and width correspond well to what is expected for h/e oscillations given the values of the inner and outer radii in our device. Figure 6.2a shows the evolution of the AB conductance oscillations (with the background removed by subtracting the magnetoresistance averaged over one period of the oscillations) measured at different temperatures. It is apparent that their amplitude decreases with increasing temperature. This decrease is quantified in the inset of Fig. 6.2b, where we plot the root mean squared value of the amplitude as a function of T in a double logarithmic scale. We find that the oscillation amplitude is proportional to $T^{-1/2}$. This dependence, which is commonly observed in metal rings, is due to thermal averaging of the h/e oscillations ($\delta G_{AB} \propto (E_{Th}/k_B T)^{1/2} \exp(-\pi r/L_\varphi(T))$, where r is the radius of the ring) [7]. It is expected for temperature values larger than the Thouless energy (which is the case here), if the phase coherence $L_\varphi = (D\tau_\varphi)^{1/2}$ length is longer than the arms of the ring. Indeed, with the value of diffusion constant given above and taking for the phase coherence time values estimated in the literature (away from the charge neutrality region $\tau_\varphi \sim 0.1$ ns at $T = 1$ K, increasing roughly linearly with decreasing T) [16][†], we find that in our ring also this condition is satisfied. A similar $T^{-1/2}$ dependence was observed for all gate voltages at which the AB oscillation amplitude was sufficiently large to be accurately measured.

The detailed dependence of the amplitude of the AB conductance oscillations on gate voltage is particularly interesting. It is apparent from Figs. 6.3a and 6.3b that at the charge neutrality point, essentially no AB oscillations are observed and that the amplitude of the oscillations becomes larger as the charge density in the sample is increased. This finding is summarized in Fig. 6.3c, in which the dependence of rms amplitude on V_G is shown to anticorrelate with the gate-voltage dependence of the total sample resistance. Indeed, if we plot the amplitude of the AB oscillations as a function of the device conductance (Fig. 6.3d), we observe that a linear relation is surprisingly well obeyed. Such a relation is predicted theoretically

---

[†] Note that in the experiments reported by Tikhonenko et al. [16], the phase coherence length becomes larger than the sample size below approximately 2.5 K. The value that we have used in our estimates is obtained by extrapolating the linear dependence observed at $T > 2.5$ K to the subkelvin regime relevant for our work. The numbers that we obtain are consistent with independent estimates of τ_ϕ reported in F. Miao, S. Wijeratne, Y. Zhang, U. C. Coskun, W. Bao, and C. N. Lau, Science 317, 1530 (2007).

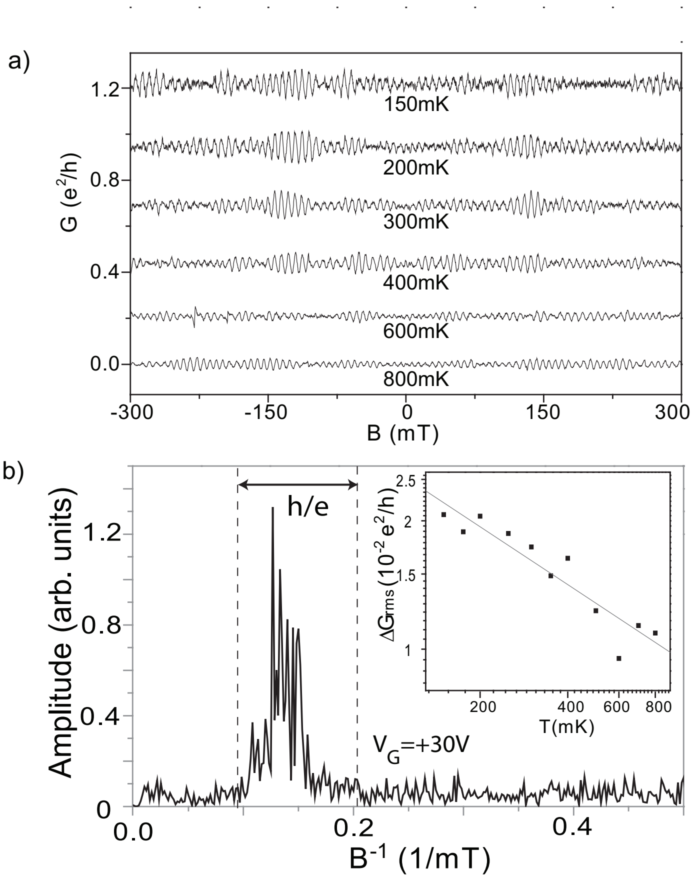

FIGURE 6.2: (a) Aharonov-Bohm conductance oscillations measured at $V_G = +30$ V for different temperatures (curves are offset for clarity). (b) Fourier spectrum of the oscillations measured at $T = 150$ mK shown in panel (a). The vertical dashed lines indicate the expected position of the h/e peak, as determined from the inner and outer radii of the ring. In the inset: temperature dependence of the root mean squared amplitude of the AB conductance oscillations, obtained from the measurements shown in panel (a).

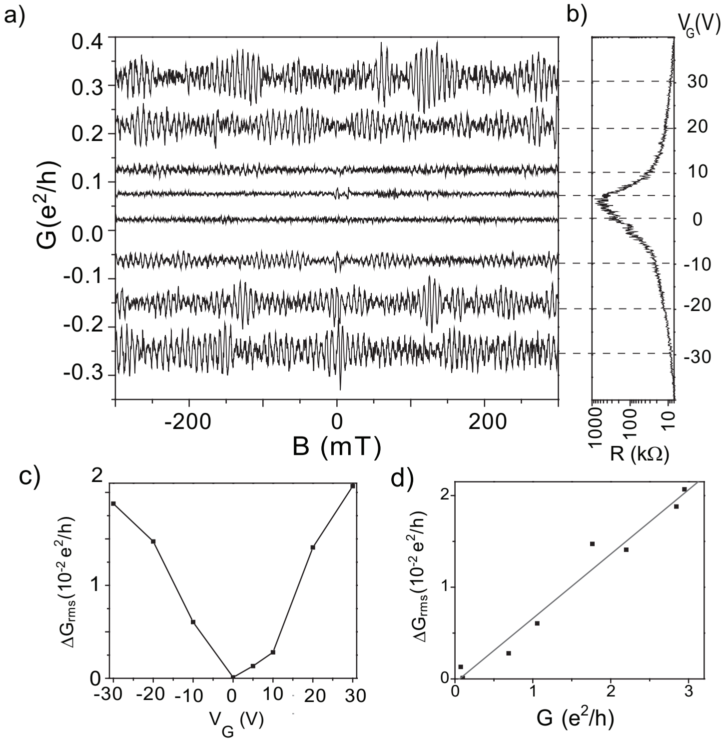

FIGURE 6.3: (a) AB conductance oscillations measured at T = 150 mK for different values of the back-gate voltage, as indicated by the dashed lines on panel (b). Panel (b) shows the dependence of the ring resistance (in logarithmic scale) on gate voltage, measured at T = 150 mK. (c) rms amplitude of the AB conductance oscillations as a function of gate voltage. In panel (d), the same data are plotted as a function of the ring conductance. The line is a guide to the eye.

for rings containing tunnel barriers [17] and it has not been observed previously in metallic rings. It is also not usually observed in rings formed in semiconducting heterostructures. Only recently, a similar dependence has been observed in experiments performed on rings fabricated using GaAs-based heterostructures in which the carrier density was changing by controlled illumination of the devices [18]. Both in these GaAs-based devices and in our graphene rings, the origin of this relation between conductance and AB oscillation amplitude is unknown.

6.5 AB-EFFECT AT HIGH MAGNETIC FIELD

All measurements discussed so far have been performed at magnetic fields smaller than 0.5 T, for which the maximum observed amplitude of the AB conductance oscillations is only $0.02e^2/h$. In Fig. 6.4c, we now plot the AB conductance oscillations measured in a larger magnetic field range (up to 9 T): the data clearly show that the rms amplitude of the oscillations is significantly larger at higher fields than around B=0 T (see also Figs. 6.4a and 6.4b). We have performed a quantitative analysis of the evolution of the h/e oscillations by determining their rms amplitude in a 350 mT interval (approximately 50 periods) as a function of magnetic field. Figure 6.5a shows that, irrespective of the temperature at which the measurement is performed, the oscillation amplitude increases and saturates starting from approximately 3 T. The relative increase is also comparable in magnitude (roughly four times) at the two different temperatures. Owing to the large amplitude, in the high field regime, the second harmonic in the Fourier spectrum of the AB oscillations becomes visible (see Fig. 6.4d, obtained from the measurement of magnetoresistance between 4 and 5 T). The temperature dependence of the amplitude of both the h/e and $h/2e$ components measured at high field still scales linearly with $T^{-1/2}$, similar to what is seen in the low field regime.

An increase in the amplitude of the AB conductance oscillations with increasing magnetic field is unusual. In metallic rings, a known mechanism causing such an increase is scattering off magnetic impurities [7,9]. At low field, the spin of these impurities can flip without any energy cost, causing dephasing of the electron waves. At higher field, the finite Zeeman energy prevents the spins to flip, leading to a decrease in dephasing and a corresponding increase in AB oscillation amplitude. Despite the fact that magnetic impurities have been predicted to form at defects in graphene or could be present at the edges [19,20], in our device, the presence of magnetic impurities cannot account for the experimental observations. In fact, if the effect observed was due to spin, one should observe that the magnetic field required for the enhancement of the oscillation amplitude increases with temperature (since the Zeeman energy has to be larger than $k_B T$), which is not what we see. An indication as to the origin of the anomalous in-

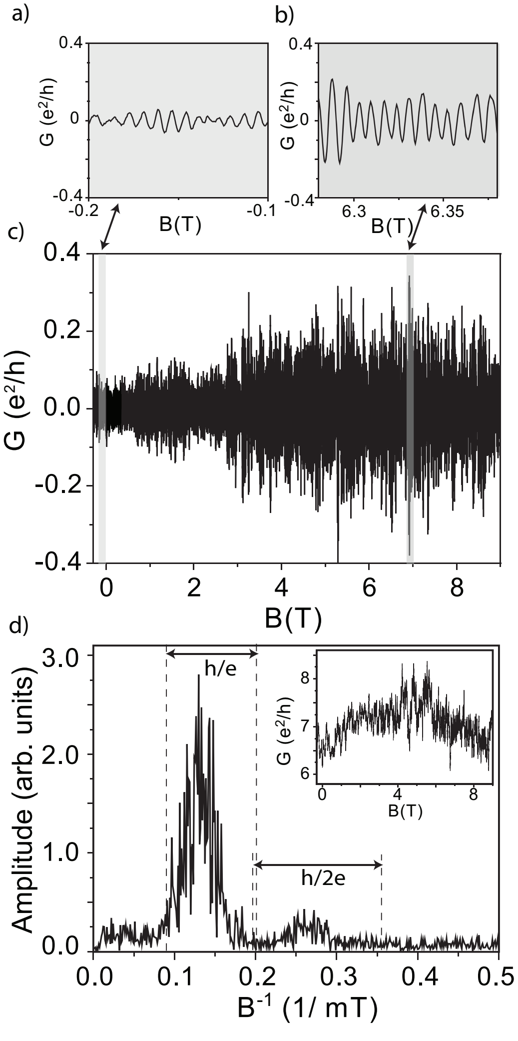

FIGURE 6.4: Panels (a)-(c) show the AB conductance oscillations measured at $V_G = +30$ V in different magnetic field ranges. For $B \sim 3$ T a clear increase of AB amplitude is observed. (d) Fourier spectrum of the AB oscillations measured between 4 and 5 T. The dashed lines indicate the position of the h/e and $h/2e$ peaks expected from the device geometry. The inset shows the magnetoconductance of the ring. All measurements were taken at 150 mK.

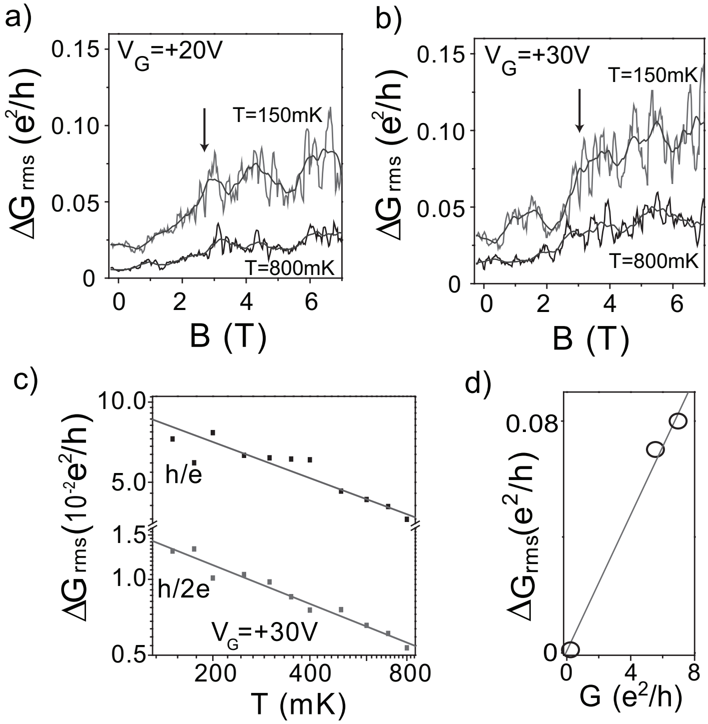

FIGURE 6.5: Panels (a) and (b) show the rms amplitude of the AB conductance oscillations determined on an interval of 50 periods as a function of magnetic field and for two different temperatures (T = 150 mK and 800 mK), measured at V_G = +20 and +30 V. The smooth curves are obtained by smoothing the corresponding data over 20 points. The arrows indicate the position in field where the oscillation amplitude starts to saturate, slightly higher at V_G = +30 V. Panel (c) shows the temperature dependence of the amplitude of the h/e and $h/2e$ components of the AB conductance oscillations measured between 4 and 5 T. The continuous lines are linear fits with slopes -0.5 ± 0.07. Panel (d) shows that the rms values of the AB oscillations measured between 4 and 5 T (at V_G = +4, +20, and +30 V) scale linearly with the conductance of the device.

crease observed in our graphene ring comes from the estimate of the diameter of the cyclotron orbit. At V_G = 30 V and 3 T − the field at which the amplitude starts saturating – the cyclotron diameter is approximately 140 nm, comparable to the width of the ribbons forming the AB ring. This suggests that the effect of the field is of orbital nature. Indeed, Fig. 6.5b shows the amplitude of the AB conductance oscillations as a function of field measured at V_G = 20 V, where the increase occurs for a slightly smaller magnetic field, as it is expected since the cyclotron diameter ($\hbar k_F/\pi eB$) is smaller at lower carrier density. The precise nature of the orbital mechanism leading to larger oscillation amplitude at higher magnetic field remains to be determined, but we suspect that the phenomenon originates from an asymmetry present in the arms of the ring caused by defects or inhomogeneity in graphene [‡].

Interestingly, the linear relation between the amplitude of AB oscillations and the device conductance persists also at high field. Although less data are available − we have only performed high field measurements at V_G = +4, +20, and +30 V − when plotted as a function of conductance, the points still fall on one single line (see Fig. 6.5d). As mentioned above, such a linear relation is predicted theoretically for rings containing tunnel barriers in their arms [17].

6.6 CONCLUSIONS AND DISCUSSION

The linear relation between the amplitude of AB oscillations and the conductance of the ring, observed at high and low magnetic field, may indicate that, consistent with the scenario that we propose to explain the observed magnetic field dependence [‡], the graphene ring is rather strongly inhomogeneous and contains small, highly resistive regions acting as weak links or tunnel barriers. Whereas the presence of such highly resistive regions would not be surprising in the low density regime, it is less obvious that it should be expected when the density of charge carriers is of the order of $(2-5)\cdot 10^{12}$ cm^{-2} (corresponding to the high V_G values in our experiments). A theoretical analysis of the relation between AB oscillation amplitude and ring conductance in graphene devices is called for, and it is likely that it will prove insightful to understand the nature of transport through narrow

---

[‡] We envision the possibility that a defect - e.g., a constriction - is present in one of the arms of the ring. For such an asymmetric configuration, the AB oscillation amplitude is smaller than for a symmetric ring, which may explain why at low field $\delta G_{AB} \sim 0.02e^2/h$ only. By squeezing the size of the cyclotron orbit, a large magnetic field can increase the transmission through the constriction and tends to equalize the transmission through the two arms. As a consequence, the oscillation amplitude increases. Note that one would then also expect an increase in conductance whose magnitude depends on the magnitude of the asymmetry between the two arms in the ring. Indeed, albeit small, an increase in the conductance is observed (see inset of Fig. 6.4d) to occur for the same fields that lead to the increase in the AB oscillation amplitude.

graphene ribbons.

In conclusion, we have reported the first observation and systematic study of Aharonov-Bohm conductance oscillations through a graphene ring. We find that in rings with a diameter of approximately 1 μm, the phase coherence length of electrons is comparable to or longer than the device size for temperatures below 1 K. As a result, the oscillation amplitude increases as $T^{-1/2}$ with decreasing temperature, owing to thermal averaging on an energy scale larger than the Thouless energy. We also observe an increase of the AB oscillation amplitude at high magnetic field, originating from an orbital effect of the magnetic field. Surprisingly, measurements as a function of gate voltage show that the amplitude of the conductance oscillations scales linearly with the total conductance of the device, a phenomenon whose microscopic origin remains to be understood in detail.

6.7 REFERENCES

1. A. K. Geim and K. S. Novoselov, The rise of graphene, Nat. Mater. 6, 183-191 (2007).
2. S. V. Morozov, K. S. Novoselov, M. I. Katsnelson, F. Schedin, L. A. Ponomarenko, D. Jiang, and A. K. Geim, Strong suppression of weak localization in graphene, Phys. Rev. Lett. 97, 016801 (2006).
3. E. McCann, K. Kechedzhi, V. I. Fal'ko, H. Suzuura, T. Ando, and B. L. Altshuler, Weak-localization magnetoresistance and valley symmetry in graphene, Phys. Rev. Lett. 97, 146805 (2006).
4. A. F. Morpurgo and F. Guinea, Intervalley scattering, long-range disorder, and effective time-reversal symmetry breaking in graphene, Phys. Rev. Lett. 97, 196804 (2006).
5. R. V. Gorbachev, F. V. Tikhonenko, A. S. Mayorov, D. W. Horsell, and A. K. Savchenko, Weak localization in bilayer graphene, Phys. Rev. Lett. 98, 176805 (2007).
6. H. B. Heersche, P. Jarillo-Herrero, J. B. Oostinga, L. M. K. Vandersypen, and A. F. Morpurgo, Bipolar supercurrent in graphene, Nature (London) 446, 56-59 (2007).
7. S. Washburn and R. A. Webb, Aharonov-Bohm effect in normal metal quantum coherence and transport, Adv. Phys. 35, 375-422 (1986).
8. A. E. Hansen, A. Kristensen, S. Pedersen, C. B. Sorensen, and P. E. Lindelof, Mesoscopic decoherence in Aharonov-Bohm rings, Phys. Rev. B 64, 045327 (2001).
9. F. Pierre and N. O. Birge, Dephasing by extremely dilute magnetic impurities revealed by Aharonov-Bohm oscillations, Phys. Rev. Lett. 89, 206804 (2002).
10. P. Recher, B. Trauzettel, A. Rycerz, Ya. M. Blanter, C. W. J. Beenakker, and A. F. Morpurgo, Aharonov-Bohm effect and broken valley degeneracy in graphene rings, Phys. Rev. B 76, 235404 (2007).
11. A. Rycerz and C. W. J. Beenakker, Aharonov-Bohm effect for a valley-polarized

current in graphene, arXiv:0709.3397 (2007).
12. K. S. Novoselov, A. K. Geim, S. V. Morozov, D. Jiang, Y. Zhang, S. V. Dubonos, I. V. Grigorieva, and A. A. Firsov, Electric field effect in atomically thin carbon films, Science 306, 666-669 (2004).
13. P. Blake, E. W. Hill, A. H. C. Neto, K. S. Novoselov, D. Jiang, R. Yang, T. J. Booth, and A. K. Geim, Making graphene visible, Appl. Phys. Lett. 91, 063124 (2007).
14. M. Y. Han, B. Özyilmaz, Y. B. Zhang, and P. Kim, Energy band-gap engineering of graphene nanoribbons, Phys. Rev. Lett. 98, 206805 (2007).
15. T. J. Ando, Screening effect and impurity scattering in monolayer graphene, J. Phys. Soc. Jpn. 75, 074716 (2006).
16. F. V. Tikhonenko, D. W. Horsell, R. V. Gorbachev, and A. K. Savchenko, Weak localization in graphene flakes, Phys. Rev. Lett. 100, 056802 (2008).
17. Y. V. Nazarov, Quantum interference, tunnel junctions and resonant tunneling, Physica B 189, 57-69 (1993).
18. L. Angers, E. Zakka-Bajjani, R. Deblock, S. Guéron, H. Bouchiat, A. Cavanna, U. Gennser, and M. Polianski, Magnetic-field asymmetry of mesoscopic dc rectification in Aharonov-Bohm rings, Phys. Rev. B 75, 115309 (2007).
19. M. A. H. Vozmediano, M. P. Lopez-Sancho, T. Stauber, and F. Guinea, Local defects and ferromagnetism in graphene layers, Phys. Rev. B 72, 155121 (2005).
20. A. Okada and A. Oshiyama, Magnetic ordering in hexagonally bonded sheets with first-row elements, Phys. Rev. Lett. 87, 146803 (2001).

7

STRONG LOCALIZATION IN GRAPHENE NANORIBBONS

In this chapter, we study the conductance in the transport gap of graphene nanoribbon devices. At low charge densities, we observe Coulomb blockade effects indicating that Coulomb islands are formed. We determine the magnetic field and temperature dependence of the average conductance in the gap. The average conductance increases with magnetic field (for $B \lesssim 3$ *T) and saturates at higher fields. These observations can be explained by the presence of strongly localized electron states with a localization length (*$\xi \approx 37$ *nm) that is of the same order as the mean free path (*$l_m \sim 10$ *nm). Moreover, these measurements indicate that the localization length increases by an applied magnetic field due to time reversal symmetry breaking. The temperature dependence of the average conductance in the gap is best described by a variable range hopping mechanism. The corresponding hopping energy at high magnetic field is lower than at low field. This observation indicates a larger localization length at high field, and is therefore qualitatively consistent with the magnetic field dependent measurements.*

Parts of this chapter have been submitted for publication:
J. B. Oostinga, B. Sacépé, M. F. Craciun, A. F. Morpurgo, *Magnetotransport through graphene nanoribbons.* Submitted to Physical Review Letters (2010).

7.1 INTRODUCTION

Graphene is a promising material for future use in high-speed integrated nanoelectronic circuits [1]. It has an almost perfect crystal quality and it is rather easy to produce. The electrons have a long mean free path and room temperature mobilities up to 10^4 - 10^5 cm^2/Vs have been measured (ten times higher, or more, than in silicon). However, since graphene has no bandgap, electric currents cannot be switched off in graphene devices. This is one of the most serious obstacles that needs to be overcome before graphene field effect transistors will be within technological reach.

Although graphene is intrinsically gapless, an energy gap has been predicted in graphene nanoribbons [2-4]. These ribbons are (quasi-)one-dimensional structures cut out of a two-dimensional sheet of graphene. The presence of a transport gap has been confirmed by transport measurements on graphene nanoribbons [5-11]. However, the physical origin of the observed gap is still under debate. In this chapter, we will argue that strong localization of interacting electrons can explain the transport gap observed in our graphene nanoribbons.

7.2 THE TRANSPORT GAP

Bandstructure calculations have shown that a bandgap arises in narrow graphene nanoribbons due to lateral confinement of electronic states and interaction effects [2-4]. The value of this bandgap highly depends on the boundary conditions, determined by the edge structure and the ribbon width. The predictions of a bandgap stimulated experimental groups to perform transport measurements on graphene nanoribbons [5-11]. In practice, narrow ribbons are etched out of large graphene flakes, and the edge structure cannot be controlled microscopically. Consequently, much disorder is introduced at the edges. The first experiments showed a transport gap in all ribbons with typical width $W \lesssim 100$ nm [5]. However, it is unclear if this transport gap originates from a bandgap.

More recent experiments have shown that, in the transport gap, the current is limited by Coulomb blockade effects [7-10]. These observations indicate that Coulomb islands are formed in the ribbon. Sols et al. [12] suggested that the variation of the ribbon width may give rise to the formation of a series of quantum dots in the ribbon, which could explain the observed quantum dot behaviour. Another suggested explanation is the presence of a bandgap in conjunction with a disorder potential [7-10]. This disorder potential may be induced by the presence of charged impurities at the surface of the ribbon [7,10], and may give rise to a distribution of isolated puddles of electrons and holes in the ribbons. The observed Coulomb blockade effects may be attributed to these puddles which act as quantum dots. However, a convincing experimental proof for this mechanism is still missing.

Alternatively, it is predicted that electrons in graphene nanoribbons can be strongly localized at low charge densities [13-17]. Since graphene nanoribbons are highly disordered, intervalley scattering will not be suppressed as in usual graphene. Edge and bulk disorder yield strong scattering, and consequently the tendency to localization will affect electronic transport much more effectively. Strong localization will give rise to an insulating state, even when a bandgap is absent. Additionally, a Coulomb gap will appear at the Fermi level when Coulomb interactions are relevant in the strong localization regime [18]. This may be an alternative explanation of the observed transport gap and the Coulomb blockade effects in graphene nanoribbons [17,19]. Recently, transport measurements have shown that the insulating properties are indeed consistent with localization of electronic states [11].

In this chapter, we study the properties of the transport gap as a function of charge density, magnetic field and temperature. Our experimental findings provide a better understanding of the nature of the transport gap in graphene nanoribbons.

7.3 GRAPHENE NANORIBBON DEVICES

We fabricated many electronic devices consisting of graphene nanoribbons by the following procedure. After mechanical exfoliation of natural graphite, we obtained graphene flakes on a Si/SiO$_2$ substrate. The highly p-doped Si was used as backgate with the SiO$_2$ as gate dielectric. We identified single-layer graphene flakes by determining their contrast with respect to the substrate in an optical microscope [20]. By conventional ebeam lithography techniques, the electrical contacts were patterned on graphene, followed by evaporation of 10 nm Ti and 40 nm Au. Subsequently, an etching mask was patterned during a second lithography step. The narrow ribbons were etched out of the flakes by using an Ar plasma. Different ribbons of various lengths ($L \approx 500-1000$ nm) and widths ($W \approx 50-100$ nm) were obtained. A typical device is schematically shown in the inset of figure 7.1a.

By applying backgate voltages we could control the charge density electrostatically: $n = (\epsilon_r\epsilon_0/te)V_{bg}$, where $t = 285$ nm is the thickness of the SiO$_2$ layer and ϵ_0 and $\epsilon_r = 3.9$ are the electric permittivity of vacuum and SiO$_2$, respectively. To study the transport properties, two-probe measurements were performed at cryogenic temperatures ($T = 2-60$ K) and magnetic fields up to 8 T. Since the ribbons were highly resistive, the contact resistances could be ignored (the metal electrodes were contacted at a wide part of the graphene flake resulting in a relative low contact resistance, usually a few hundred Ohms). We performed conductance measurements as a function of back-gate voltage, temperature and magnetic field on many different devices yielding consistent results (the conductance was mea-

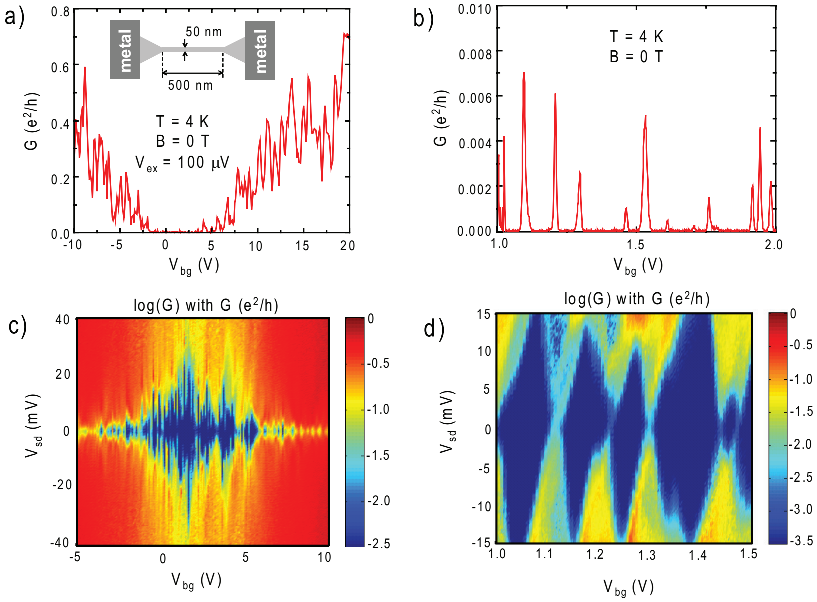

FIGURE 7.1: (a) The conductance G as a function of the gate-voltage V_{bg}, showing a transport gap at low charge densities. The inset shows a schematic picture of the device geometry. (b) In the transport gap, Coulomb peaks are observed when sweeping the gate voltage with smaller steps. (c) Colorplot of log(G) as a function of voltage bias V_{sd} measured at different V_{bg}, showing the insulating regime at low charge densities and small voltage bias V_{sd} ($T = 4$ K, $B = 0$ T). (d) When sweeping the gate voltage with smaller voltage steps, Coulomb diamonds are observed in the colorplot at low charge densities ($T = 4$ K, $B = 0$ T).

sured by using a lock-in amplifier in a voltage bias configuration). Here, we discuss the systematic results of a ribbon with length $L = 500$ nm and width $W = 50$ nm (see inset of figure 7.1a), which is representative of the overall behaviour observed. All data shown in this chapter corresponds to this ribbon, unless stated otherwise.

7.4 COULOMB BLOCKADE

First, we study the conductance in the transport gap. In figure 7.1a, the differential conductance G of the ribbon as a function of the gate voltage V_{bg} is shown. The conductance is strongly suppressed in the voltage range $[-2V, +4V]$. Effectively, the ribbon becomes insulating for these values of the gate voltage, therefore we refer to this voltage range as to the transport gap. Figure 7.1b shows the conductance in this insulating regime by sweeping the gate with smaller voltage steps. Reproducible conductance peaks appear at several gate voltages, while the conductance vanishes between these peaks. This is a strong indication that charging effects give rise to Coulomb blockade in the ribbon.

We also measured the conductance as a function of voltage bias (V_{sd}) at different gate voltages (figure 7.1c and 7.1d). We clearly observe an insulating regime, where the conductance is highly suppressed at low V_{sd}. The irregular structure of this insulating regime, shown in (figure 7.1c), results in a series of diamond-like structures when measurements are performed by sweeping the gate voltage with smaller steps (figure 7.1d). These diamond-like structures are expected when Coulomb blockade limits the current through the ribbon. Apparently, the electrons are confined or localized in small areas of the ribbon (which we will call islands). Figure 7.1d shows that the diamonds have different sizes and partially overlap, indicating that islands with varying size in series contribute to the current through the ribbon.

7.5 MAGNETIC FIELD DEPENDENCE

Next, we explore the effects of a magnetic field on the conductance in the transport gap. In figure 7.2a, the conductance as a function of backgate voltage at different magnetic fields from 0 to 8 T is shown. We observe that the transport gap becomes smaller if the magnetic field increases. Figure 7.2b shows a similar measurement as in figure 7.1c, but now at a high magnetic field ($B = 8$ T). It is apparent that the (bias and gate) voltage ranges at which we observe the insulating regime, are smaller at high field (note that we have observed similar behaviour in several devices).

We also observe Coulomb peaks (figure 7.3a) and Coulomb diamonds (figure 7.3b) at $B = 8$ T. Interestingly, in the presence of a high magnetic field, the average number of Coulomb peaks and the peak conductance are higher. This evolution

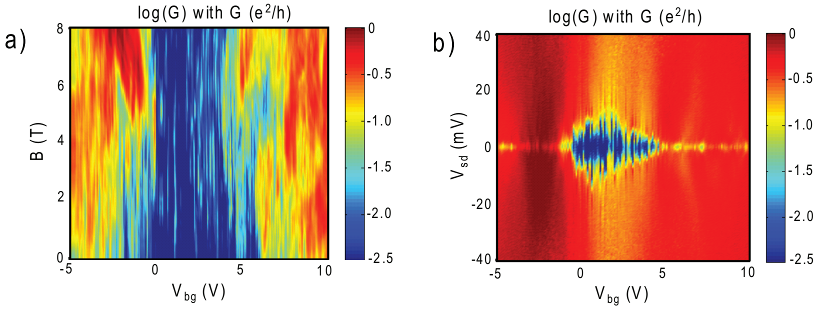

FIGURE 7.2: (a) Colorplot of log(G) as a function of V_{bg} measured at different magnetic fields B (T = 4 K), showing a decreasing transport gap for increasing B. (b) Colorplot of log(G) as a function of voltage bias V_{sd} measured at different V_{bg} at B = 8 T (T = 4 K), showing an insulating regime on a smaller bias- and gate-voltage range than at B = 0 T (see figure 7.1c).

from B =0 T to 8 T can be clearly seen in figure 7.3c. Qualitatively, these observations are expected when the average island size in the ribbon increases with magnetic field. This increase will be discussed in more detail in next section.

From the data shown in figure 7.3c, we determine the average value of the conductance as a function of magnetic field in the gate voltage range $[+1V, +3V]$. Since the conductance between the Coulomb peaks is negligibly small due to Coulomb blockade, this average value is mainly a measure of the average conductance at the Coulomb peaks and the number of peaks. Figure 7.4 clearly shows that the average conductance increases with magnetic field for $B < 3$ T and that it saturates for $B > 3$ T. Consequently, we can conclude that the average number of Coulomb peaks and the average peak conductance increase for $B < 3$ T, but remain approximately constant for $B > 3$ T. Similar measurements on two other ribbons, which have a different width, W = 80 nm and W = 110 nm, show that these ribbons exhibit qualitatively a similar magnetic field dependence (figure 7.4). Most surprisingly, the average conductance saturates at approximately similar values of the magnetic field, irrespective of the ribbon width. These observations can be explained by considering strong localization of electronic states.

7.6 STRONG LOCALIZATION OF ELECTRONS

Figure 7.1a shows that the transport gap is only observed at low charge densities. From the slope $\partial G/\partial V_{bg}$ at high charge densities, we can determine the field-effect mobility: $\mu = \frac{tL}{W\epsilon_r\epsilon_0}\frac{\partial G}{\partial V_{bg}} \approx 1000$ cm^2/Vs (note that we disregard the large conductance fluctuations). This value is smaller than the mobilities usually found for graphene flakes ($\mu \sim 5000 - 10000$ cm^2/Vs [1]), confirming that graphene nanorib-

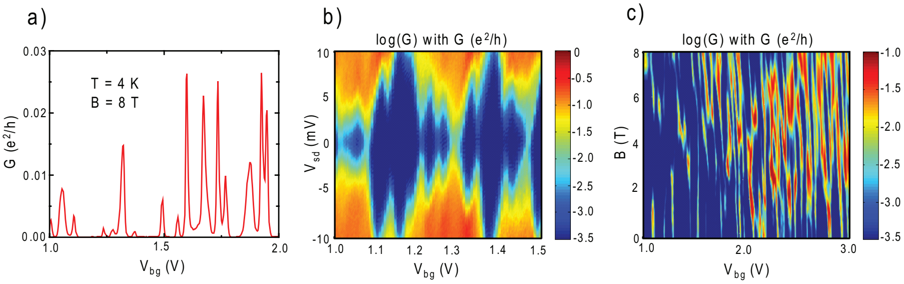

FIGURE 7.3: (a) The conductance G as a function of the gate-voltage V_{bg} at $B = 8$ T, showing Coulomb peaks in the transport gap. (b) Colorplot of $\log(G)$ as a function of voltage bias V_{sd} measured at different V_{bg} at $B = 8$ T ($T = 4$ K), showing Coulomb diamonds at low charge densities. (c) Colorplot of $\log(G)$ as a function of V_{bg} measured from $B = 0$ T to 8 T ($T = 4$ K), showing that the average number of Coulomb peaks and the average peak conductance increase if B increases.

bons are more disordered.

In this high density regime, we can determine the mean free path l_m using the Einstein relation $\sigma = \nu e^2 D$ (where D is the diffusion constant). At $V_{bg} = -10$ V, we determine the conductivity, $\sigma \approx G_\square = GL/W$, and the charge density, $\nu(\varepsilon_F) = 8\pi|\varepsilon_F|/(h^2 v_F^2)$ (with ε_F and v_F are the Fermi energy and Fermi velocity, respectively). Here, ε_F is obtained from the charge density induced electrostatically, $n(V_{bg} = -10V) = 4\pi\varepsilon_F^2/(h^2 v_F^2) \approx 1\cdot 10^{12}$ cm^{-2}. This yields $D \approx 0.006$ m^2/s and $l_m = 2D/v_F \approx 10$ nm. Thus, the mean free path at high charge density is smaller than the ribbon width ($W = 50$ nm).

While the ribbon is conducting at high charge densities, it becomes insulating at low densities. The short mean free path value indicates the presence of strong disorder and suggests that the electrons are strongly localized at low charge density. A signature of an insulating state due to strong localization is a positive magnetoconductance, which originates from an increase of the localization length ξ due to time reversal symmetry breaking [18,21-23]. In the strong localization regime, time reversal symmetry is broken when the magnetic flux through an area of ξ^2 is of the order of the flux quantum h/e. This mechanism can explain our data of figure 7.4, which shows that the average conductance at low n increases when sweeping the magnetic field from 0 T to ~3 T. The saturation of the average conductance at $B > 3$ T may indicate that time reversal symmetry is broken at $B \approx 3$ T, which corresponds to a localization length of $\xi \approx (h/eB)^{1/2} \approx 37$ nm (note that this value of ξ is smaller than the ribbon width, for all three ribbons plotted in figure 7.4).

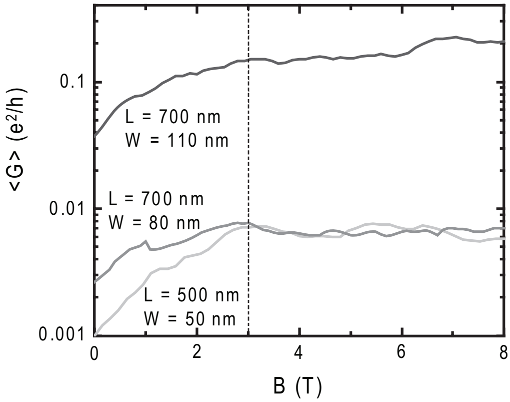

FIGURE 7.4: Average conductance $< G >$ in the transport gap as a function of B ($T = 4$ K) for three ribbons with different width ($< G >$ is determined in a gate-voltage range of $\Delta V_{bg} = 2$ V). Irrespective of the ribbon width, an increase of $< G >$ with increasing B is observed for $B < 3$ T, while $< G >$ saturates for $B > 3$ T.

Close to the charge neutrality point, it is theoretically expected that $\xi \sim l_m$, because the number of occupied transverse channels is low [13,18,19,21-23]. This indicates that close to the charge neutrality point l_m is of the same order as at high density (≈ 10 nm). In the strong localization regime, ξ should be smaller than the phase coherence length l_φ. We can estimate $l_\varphi = (D\tau_\varphi)^{1/2}$ by using $D = 0.006$ cm^2/Vs and $\tau_\varphi \approx 5$ ps (at T =4 K; estimated from the experimental data of Ref. [24]), which gives $l_\varphi \approx 175$ nm. This shows that $l_m \lesssim \xi < l_\varphi$ and, therefore, is consistent with what we would expect if strong localization occurs [21].

We propose that the electrons are strongly localized within domains of size ξ^2. Such localization domains can be considered as islands. Because of the small island size, not only the localization energy, but also the charging energy of an island and the Coulomb interactions between islands will affect electronic transport. This will give rise to Coulomb blockade effects and may explain our observations of conductance peaks and Coulomb diamonds at zero magnetic field (figure 7.1b and 7.1d) as well as at high field (figure 7.3a and 7.3b). The increase of the average conductance in figure 7.4, which corresponds to a decrease of the average peak spacing and an increase of the average peak height, indicates an increase of the average island size with magnetic field. This observation is qualitatively in agreement with an increase of the localization length, as expected when time reversal symmetry is broken.

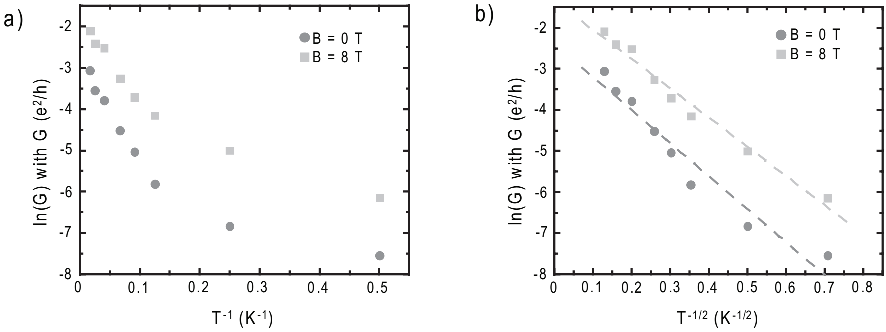

FIGURE 7.5: (a) Arrhenius plot of the average conductance $< G >$ in the transport gap at $B = 0$ T and $B = 8$ T ($< G >$ is determined in a gate-voltage range of $\Delta V_{bg} = 2$ V). (b) The same data plotted as a function of $T^{-1/2}$. The dashed lines are linear fits to the data.

7.7 VARIABLE RANGE HOPPING

When electrons are strongly localized, they can hop from one electron state to another yielding an electric current. In general, two hopping mechanisms are distinguished: nearest neighbour hopping and variable range hopping [18,22]. Since both hopping mechanisms yield a different temperature dependent conductance, we can use this difference to determine which transport mechanism dominates in graphene nanoribbons.

We measured the average conductance in the gap as a function of temperature at B =0 T and 8 T in the temperature range 2 – 60 K (figure 7.5a,b). If electronic transport occurs by nearest neighbour hopping, the temperature dependence of the conductance should be $G \propto \exp -(T_0/T)$ [18,22] (with a characteristic temperature T_0). However, the non-linear Arrhenius plots of figure 7.5a indicate that nearest neighbour hopping is not the dominant transport mechanism.

If variable range hopping occurs, the temperature dependence of the conductance should be $G \propto \exp -(T_0/T)^n$ [18,22], where the exponent n depends on the dimensionality of the system as well as on the presence of Coulomb interactions. Since Coulomb interactions are relevant in graphene nanoribbons, an exponent of $n = 1/2$ is expected (irrespective of the dimensionality of the system). Indeed, figure 7.5b shows that the data fits better to $G \propto \exp -(T_0/T)^{1/2}$. This result indicates that electronic transport is dominated by variable range hopping (note that we have observed a similar temperature dependence in several ribbons).

The parameter T_0 is related to the energy needed by an electron to hop between localized states. At $B = 0$ T, we obtain $kT_0 \approx 6$ meV from the fit to the data of figure 7.5b[†]. On the other hand, the fit to the data of $B = 8$ T yields a smaller value, $kT_0 \approx 4$ meV. This result is qualitatively in agreement with what we would expect if ξ is larger at high magnetic field, because the level spacing and the charging energy, which determine the hopping energy, become smaller if the localization length increases. Thus, this result is consistent with the magnetic field dependent measurements, which also indicates that the average island size at high field is larger than at zero field.

We should note that at high temperatures ($T > 10$ K), the Arrhenius plots of figure 7.5a become more linear. This may indicate that a crossover from variable range hopping to nearest neighbour hopping occurs if $T \gtrsim 10$ K. Such a crossover is theoretically predicted for strongly localized electrons in graphene nanoribbons [17]. On the other hand, we should take into account that at higher temperatures, the Coulomb peaks broaden and the conductance between the peaks increases significantly (i.e. effectively the conductance is not blockaded anymore at higher temperatures). While at low temperatures ($T \lesssim 10$ K), the average conductance is mainly determined by the conductance at the peaks, the conductance between the peaks starts to contribute to the average value at high temperatures ($T \gtrsim 10$ K). This may also explain the observed deviation of the temperature dependence at higher temperatures. However, the temperature dependence of the average conductance, which depends on the exact nature of the localized states, remains to be understood.

7.8 CONCLUSIONS AND DISCUSSION

The first experiments on graphene nanoribbons were performed by Han et al. [5] and Chen et al. [6]. They attributed the transport gap to the presence of a bandgap, which is theoretically predicted in nanoribbons. In the presence of a high magnetic field, when the magnetic length, $l_B = (\hbar/eB)^{1/2}$, becomes smaller than the ribbon width, Landau levels are expected to appear in the energy spectrum. These Landau levels will give rise to the appearance of edge states which contribute to the conductance ($\sim e^2/h$). Since graphene has a zeroth Landau level exactly at the center

---

[†] Note that this hopping energy of 6 meV is an order of magnitude smaller than what we would expect by simply considering the level spacing, $\Delta \sim \hbar v_F/\xi \approx 17$ meV, and the charging energy, $E_c \sim e^2/C_g \approx e^2/2\epsilon_0(\epsilon+1)\xi \approx 50$ meV [25] (by using $\xi = 37$ nm at $B = 0$ T). A possible explanation of this large mismatch is that, due to the coupling of neighbouring islands, the effective values of the level spacing and the charging energy may be much smaller than expected from an island with dimensions equal to the localization length. Furthermore, if an electron hops from one island to another, we would expect that it only needs to pay the difference in charging energy, ΔE_c, which is smaller than E_c. However, based on our measurements, a conclusive explanation of the mismatch cannot be given. A more quantitative study of the hopping mechanism in graphene nanoribbons is required to be able to explain the extracted values of T_0.

of the gap ($E = 0$), the appearance of this Landau level will close the bandgap. Although in our experiments $l_B \approx 10$ nm for $B = 8$ T, we did not observe any signature of the presence of edge states in the transport gap (while $l_B < W$). Therefore, in our measurements we cannot attribute the magnetic field dependence of the conductance to the formation of Landau levels. The absence of edge states is an indication that the ribbons are highly disordered.

Since the ribbons are disordered, some groups attributed the transport gap to a bandgap in conjunction with a disorder potential [7-10]. They assumed that disorder induced potential fluctuations give rise to puddles of electrons and holes, as observed in usual graphene [26]. These puddles may be separated by a bandgap [2-4] and give rise to Coulomb islands. However, it is unclear how this mechanism can explain the increase of the average conductance with increasing magnetic field, as we observed in our experiments.

More recently, experiments have shown that the transport gap of disordered nanoribbons can be explained by strong localization of electronic states [11], as theoretically predicted in disordered ribbons [13-17]. Complementary to these experiments, we have shown in this chapter that the transport gap, observed in our ribbons, can indeed be explained by strong localization: (i) We observed Coulomb peaks and Coulomb diamonds at low n, as expected when Coulomb islands are formed in the ribbon, which scale with the localization length ξ; (ii) We observed that the average peak spacing decreases and the average peak height increases with increasing magnetic field up to ~3 T, while they remain approximately constant at higher fields. This is expected in the strong localization regime, when ξ increases with magnetic field until time reversal symmetry is fully broken [18,21-23]; (iii) From the value of the crossover-field ($B \approx 3$ T), we have estimated the localization length, $\xi \approx 37$ nm. We found that $l_m \lesssim \xi < l_\varphi$, which indicates that electrons are indeed strongly localized [21]; (iv) We showed that electronic transport is best described by a variable range hopping mechanism: $G \propto \exp -(T_0/T)^n$ with $n = 1/2$. We found that the fitted value of T_0 is higher at $B = 0$ T than at 8 T, as expected when the localization length at high magnetic field is larger than at low field.

In conclusion, our transport measurements indicate that the transport gap, which appears at low charge densities, originates from strong localization of electronic states. We suggest that disorder induced localization effects effectively lead to the formation of Coulomb islands which scale with the localization length. The measurements show that the effective island size increases by a magnetic field, which can be explained by an increase of the localization length due to time reversal symmetry breaking. Moreover, our measurements indicate that electronic transport occurs by variable range hopping between these islands, while Coulomb blockade effects limit the current at low temperatures.

7.9 REFERENCES

1. A. K. Geim, K. S. Novoselov, The rise of graphene, Nat. Mater. 6, 183-191 (2007).
2. K. Nakada, M. Fujita, G. Dresselhaus, M. S. Dresselhaus, Edge state in graphene ribbons: Nanometer size effect and edge shape dependence, Phys. Rev. B 54 (24), 17954 (1996).
3. Y. -W. Son, M. L. Cohen, S. G. Louie, Energy gaps in graphene nanoribbons, Phys. Rev. Lett. 97, 216803 (2006).
4. L. Brey, H. A. Fertig, Electronic states of graphene nanoribbons studied with the Dirac equation, Phys. Rev. B 73, 235411 (2006).
5. M. Y. Han, B. Özyilmaz, Y. Zhang, P. Kim, Energy band-gap engineering of graphene nanoribbons, Phys. Rev. Lett. 98, 206805 (2007).
6. Z. Chen, Y. -M. Lin, M. J. Rooks, P. Avouris, Graphene nano-ribbon electronics, Physica E 40, 228-232 (2007).
7. K. Todd, H. -T. Chou, S. Amasha, D. Goldhaber-Gordon, Quantum dot behavior in graphene nanoconstrictions, Nano Lett. 9 (1), 416-421 (2009).
8. C. Stampfer et al., Energy gaps in etched graphene nanoribbons, Phys. Rev. Lett. 102, 056403 (2009).
9. X. Liu, J. B. Oostinga, A. F. Morpurgo, L. M. K. Vandersypen, Electrostatic confinement of electrons in graphene nanoribbons, Phys. Rev. B 80 (12), 121407 (2009).
10. P. Gallagher, K. Todd, D. Goldhaber-Gordon, Disorder-induced gap behavior in graphene nanoribbons, arXiv: 0909.3886 (2009).
11. M. Y. Han, J. C. Brant, P. Kim, Electron transport in disordered graphene nanoribbons, Phys. Rev. Lett. 104, 056801 (2010).
12. F. Sols, F. Guinea, A. H. Castro-Neto, Coulomb blockade in graphene nanoribbons, Phys. Rev. Lett. 99, 166803 (2007).
13. D. Gunlycke, D. A. Areshkin, C. T. White, Semiconducting graphene nanostrips with edge disorder, App. Phys. Lett. 90, 142104 (2007).
14. A. Lherbier, B. Biel, Y. -M. Niquet, S. Roche, Transport length scales in disordered graphene-based materials: Strong localization regimes and dimensionality effects, Phys. Rev. Lett. 100, 036803 (2008).
15. M. Evaldsson, I. V. Zozoulenko, H. Xu, T. Heinzel, Edge-disorder-induced Anderson localization and conduction gap in graphene nanoribbons, Phys. Rev. B 78, 161407 (2008).
16. E. R. Mucciolo, A. H. Castro-Neto, C. H. Lewenkopf, Conductance quantization and transport gaps in disordered graphene nanoribbons, Phys. Rev. B 79, 075407 (2009).
17. I. Martin, Y. M. Blanter, Transport in disordered graphene nanoribbons, Phys. Rev. B 79, 235132 (2009).
18. B. I. Shklovskii, A. L. Efros, Electronic properties of doped semiconductors

(Springer, Heidelberg, Germany, 1984).
19. M. Fogler, Low-temperature transport in graphene ribbons, Oral presentation at ESF-FWF Conference "Graphene Week 2009", Universitätszentrum Obergurgl, Austria, 2-7 March 2009.
20. P. Blake et al., Making graphene visible, App. Phys. Lett. 91, 063124 (2007).
21. S. Datta, Electronic transport in mesoscopic systems (Cambridge Univ. Press, Cambridge, UK, 1995).
22. Y. Imry, Introduction to mesoscopic physics (Oxford Univ. Press, Oxford, UK, 1997).
23. M. E. Gershenson, Y. B. Khavin, A. G. Mikhalchuk, H. M. Bozler, A. L. Bogdanov, Crossover from weak to strong localization in quasi-one-dimensional conductors, Phys. Rev. Lett. 79 (4), 725-728 (1997).
24. F. V. Tikhonenko, D. W. Horsell, R. V. Gorbachev, A. K. Savchenko, Weak localization in graphene flakes, Phys. Rev. Lett. 100, 056802 (2008).
25. L. A. Ponomarenko et al., Chaotic Dirac billiard in graphene quantum dots, Science 320, 356 (2008).
26. J. Martin et al, Observation of electron-hole puddles in graphene using a scanning single-electron transistor, Nat. Phys. 4, 144-148 (2008).

APPENDIX

In this appendix, we describe how graphene flakes are prepared, how electronic devices are fabricated, and how the fabricated devices are measured electrically in cryogenic measurement setups.

PREPARATION OF GRAPHENE FLAKES

Graphene flakes are prepared by the following procedure:

1. Highly p-doped Si wafers with thermally grown SiO_2 (thickness 285 nm) are obtained from the company Nova Electronic Materials, Ltd. We dice these 4" circular wafers to get square substrates of 19x19 mm^2.

2. After cleaning the 19x19 mm^2 substrates (similar to the pre-cleaning step that will be described in step 3), we pre-pattern the substrates by standard e-beam lithography techniques (see next section). The pattern consists of bonding pads and markers and is created by evaporation of 10 nm Ti followed by 50 nm AuPd (a mixture of 60% Au and 40% Pd). After lift-off, the substrates are cut into pieces, corresponding to eight samples of ~5x7 mm^2 with pre-defined markers and bonding pads.

3. Before graphene is transferred to a 5x7 mm^2 sample, the sample is pre-cleaned as follows, in an ultrasonic bath: (i) 2 minutes in aceton; (ii) 2 minutes in H_2O; (iii) 1 minute in fuming nitric acid (~100% HNO_3); (iv) 2 minutes in H_2O; (v) 2 minutes in isopropanol (IPA).

4. To mechanically exfoliate graphite, we take one single grain of graphite (typical size <1 mm) and put it on adhesive tape (scotch tape). Usually, we peel the graphite for about 5−10 times to get thinner graphite flakes on the tape. Then, we take a pre-cleaned sample directly from the IPA bath, we blow it dry with N_2-gas, and immediately press it with the SiO_2 side on the tape. After removing the sample from the tape, layers of graphite remain attached to the SiO_2 surface (figure A.1).

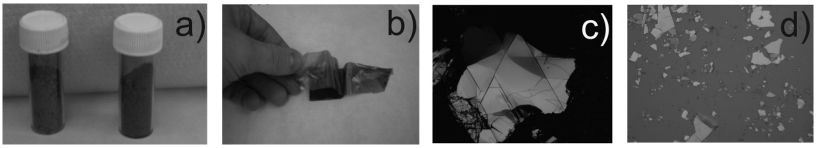

FIGURE A.1: (a) Natural graphite in a plastic cylinder, received from colleagues at other universities (e.g. from Andre Geim and Kostya Novoselov at Manchester University), (b) Repeatedly peeling of graphite with adhesive tape, (c) Optical image of graphite on the tape after cleaving, (d) Graphite flakes sticking on a Si/SiO$_2$ sample after pressing the sample on the tape.

5. After the transfer of graphite (and possibly single-layers, i.e. graphene), we post-clean the sample: (i) 30 seconds in tetrahydrofuran (THF); (2) 10 seconds in IPA. THF removes the glue residues from the sample and, additionally, removes graphite flakes that do not adhere well to the SiO$_2$ (note that these flakes are in general not useful for device fabrication).

6. In order to find graphene flakes, we inspect the sample surface with an optical microscope (Olympus BX60F5). An optical camera (Sony power HAD 3CCD color vedio camera), which is mounted on top of the microscope, is connected to a PC. By using standard real-time image-processing software (e.g. "Analysis" of Olympus), we obtain clear images of the sample surface on a computer screen. We use a digital green filter to get a better contrast between flakes and the underlying SiO$_2$ substrate. When graphene flakes are found, a digital picture is taken and the flake thickness is determined by measuring the average RGB-values of the flake relative to the substrate (see §2.7; we use the software "Adobe Photoshop" to determine the RGB-values). Using the images, the precise positions of the flakes are determined with respect to the pre-patterned reference markers on the sample.

DEVICE FABRICATION BY E-BEAM LITHOGRAPHY TECHNIQUES

Device fabrication is done under "clean-room" conditions to reduce the risks of contaminating the samples. After having identified and localized graphene flakes on a sample, devices are fabricated by the following procedure:

1. Device fabrication starts with a design in the software "Designcad". First, an optical picture of the flake with reference markers is imported into this software. Subsequently, the patterns of the different lithography steps are defined (e.g. patterns of electrical contacts, top-gates, etch structures). When a design is finished, the output file of "Designcad" is converted to a format

which can be read by the control software of the electron beam lithography (EBL) system.

2. Since we use an EBL to generate the patterns, a chemical resist that is sensitive to an electron beam (e-beam), is spun on the sample surface: (i) for the patterns of electrical contacts and top-gates, we use a double-layer resist consisting of a ~150 nm bottom-layer (PMMA 350K 3% in chlorobenzene or PMMA 495K 3% in anisol) and a ~100 nm top-layer (PMMA 950K 2% in chlorobenzene or PMMA 950K 3% in anisol); (ii) for patterns of etch structures, we only use the ~100 nm top-layer. After spinning each layer of resist, we bake the sample for 15−30 minutes at 175°C.
3. The sample with resist on top is loaded in an EBL system (Leica 5000+ EBPG operating at 100 kV). The design pattern is "written" in the resist by exposing it with a well-defined e-beam (figure A.2a). The PMMA that is exposed sufficiently by high-energy electrons, decomposes and becomes soluble in a developer. The settings of the e-beam are pre-determined by doing so-called dose-tests on test-samples (using patterns with critical dimensions of ~50 nm).
4. The chemical development of the exposed resist is done by using the following recipe (figure A.2b): (i) two minutes in a 1:3 solution of MIBK:IPA (MIBK = methylisobutylketone); (ii) one minute in IPA; (iii) blow-drying with N_2-gas.
5. After development, the electrical contacts or top-gates are evaporated, or the graphene flake is etched. In case of evaporation (figure A.2c), the sample is loaded into an e-beam evaporation system (see chapters 3−7 for details about the evaporated materials and thicknesses). In case of etching, the sample is loaded into the plasma-chamber of a sputtering machine (with this machine, 20 seconds in an Argon plasma (power of 70 Watt) is sufficient to etch graphene).
6. After evaporating materials, the remaining (unexposed) resist with metal on top needs to be removed (figure A.2d). This so-called lift-off process is done by leaving the sample for several hours in aceton (or alternatively in PRS-3000) at ~50°C. To remove the resist after etching, the sample is left for 1−2 hours in chloroform at ~50°C.
7. When all lithography steps are completed, the sample with one or more graphene devices is glued on a 32-pins golden chip-carrier by using conducting silver-paint (in order to be able to apply back-gate voltages at the conducting back-side of the silicon sample). All the contacts and top-gates on top of

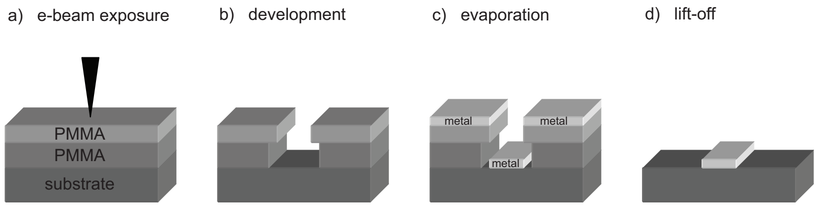

FIGURE A.2: The process of e-beam lithography: (a) a double-layer of PMMA on top of a substrate is exposed by an e-beam to "write" a pattern, (b) Development of the pattern in order to remove the exposed PMMA, (c) Evaporation of a metal, partly on the bare substrate and partly on the PMMA, (d) Lift-off process to remove the PMMA, leaving a substrate patterned with the metal.

the sample are electrically connected by bonding wires from the bonding-pads of the sample to the bonding-pads of the chip-carrier (note that the bonding-pads of the sample consist of a AuPd bottom-layer, as described in step 2 of previous section; since AuPd is a hard material, the SiO_2 is prevented to be damaged by the ultrasonic bonding machine).

ELECTRICAL MEASUREMENTS IN CRYOGENIC MEASUREMENT SETUPS

In order to measure quantum transport in the fabricated graphene devices, the chip carrier is mounted and cooled down in a cryogenic measurement setup. Different systems are used: an Oxford dilution refrigerator for temperatures from 4.2 K down to ~30 mK, a Heliox system for temperatures from ~60 K down to 235 mK, and a Desert Cryogenics dipstick setup for temperatures from ~ 60 K down to 2 K. All setups are equipped with a superconducting magnet for applying magnetic fields up to 8 or 10 T.

These cryogenic setups are optimized for performing low-noise electrical measurements. We use "in-house-built" electronic measurement systems, which are powered by batteries. Each system is controlled by a PC (we use the control software "Labview"). An optical fibre is used for communication between the PC and the measurement system in order to minimize interference effects from the PC. Additionally, each cryogenic setup contains copper shields and filters to minimize environmental noise. For instance, the setup in which we performed the supercurrent measurements (described in chapter 5), contains three different types of filters: π-filters, copper-powder filters and RC-filters.

SUMMARY

QUANTUM TRANSPORT IN GRAPHENE

Jeroen B. Oostinga

After the experimental discovery of graphene, a scientific rush started to explore graphene's electronic behaviour. Graphene is a fascinating two-dimensional electronic system, because its electrons behave as relativistic particles (i.e. they are described by the Dirac equation instead of the Schrödinger equation). Consequently, graphene has electronic transport properties which differ from usual materials. Moreover, graphene is a promising material for nano-electronic applications, because for instance, it is easy to produce and exhibits room temperature mobilities up to 10^4-10^5 cm^2/Vs. A thorough study is required to reveal graphene's exceptional electronic properties and to pave the way for the development of graphene nano-electronic devices. In this thesis, several experiments are described which contribute to a better understanding of electronic transport in graphene devices.

Single-layer and bilayer graphene are zero-gap semiconductors. At the charge neutrality (CN) point, the top of the highest valence and the bottom of the lowest conduction bands touch. Consequently, both types of graphene are gapless and have metallic properties. In chapter 3, we have presented resistance measurements of double-gated structures of single- and bilayer graphene as a function of a perpendicular electric field. Surprisingly, we observed in the bilayer a strong increase of the resistance at the CN-point with increasing electric field, while the resistance of the single-layer was unaffected by a field. In this experiment, we demonstrated that bilayer graphene can be turned from a metal to an insulator by the opening of a bandgap. Moreover, when a bilayer is turned into an insulator, we showed that its transport properties are best described by a variable range hopping mechanism.

While single-layer and bilayer graphene are zero-gap semiconductors, trilayer graphene is a semi-metal with a small band overlap. In chapter 4, we have presented resistance measurements of trilayer graphene at the CN-point as a function of temperature and perpendicular electric field. Contrary to the bilayer, in which the resistance increases with increasing electric field (due to the opening of a bandgap), the resistance of the trilayer decreases with the applied field. In our experiments, we demonstrated that the band overlap increases with an increasing electric field, which is consistent with theoretical predictions.

In ideal single-layer graphene, the density of states vanishes at the CN-point, while the conductivity does not vanish. The electronic transport properties at the CN-point are still not completely understood. In chapter 5, we have studied phase coherent transport in single-layer graphene by measuring the transport properties of graphene superconducting junctions (length $\lesssim$500 nm). Most strikingly, we observed Josephson supercurrents in all our devices, irrespective of the charge density. This demonstrated that electronic transport in single-layer graphene is phase coherent, even at the CN-point. However, these observations are in stark contrast with the magnetoresistance measurements on the same devices, which showed that weak localization is highly suppressed or even absent. We can explain this sample-specific behaviour of weak localization by considering the peculiar band properties of graphene.

In chapter 6, we have studied the Aharonov-Bohm (AB) effect in a ring-shaped structure, etched in single-layer graphene. The AB-effect gives rise to periodic conductance fluctuations as a function of magnetic field. Most surprisingly, we found that the amplitude of these oscillations scales linearly with the average conductance and vanishes at the CN-point (where the conductance is lowest). Furthermore, at high magnetic fields we observed an increase of the oscillation amplitude. The precise nature of these observations remains to be understood.

In graphene nanoribbons, a transport gap appears at low charge densities which gives rise to an insulating regime. In chapter 7, we have studied the temperature and magnetic field dependence of the average conductance in this transport gap. The average conductance increases with magnetic field and saturates at higher fields. These observations can be explained by the presence of strongly localized electron states with a localization length that increases with magnetic field due to time reversal symmetry breaking. The temperature dependence of the average conductance in the gap indicates that electronic transport occurs by variable range hopping.

In conclusion, we have shown in this thesis that we can control the bandstructure of bilayer and trilayer graphene. Simply by applying a perpendicular electric field in a graphene device, a bandgap can be tuned in the bilayer, and a band overlap can be induced in the trilayer. Furthermore, we have described transport measurements on graphene devices (length $\sim 0.1-1\ \mu$m) showing that electronic transport in graphene is phase coherent at cryogenic temperatures ($T \lesssim 4$ K). We have observed weak localization, bipolar supercurrents and the Aharonov-Bohm effect. We have also shown that in narrow graphene nanoribbons (width $\lesssim$100

nm) a transport gap appears, which can be well explained by strong localization of electronic states. Our experimental results provide a better understanding of electronic transport in graphene, and are also a first step towards the realization of graphene nano-electronic devices.

SAMENVATTING

KWANTUMTRANSPORT IN GRAFEEN

Jeroen B. Oostinga

Na de experimentele ontdekking van grafeen begon een wetenschappelijke race naar het elektronisch gedrag. Grafeen is een fascinerend tweedimensionaal elektronensysteem, omdat de elektronen zich gedragen als relativistische deeltjes (dat wil zeggen dat ze worden beschreven door de Dirac vergelijking in plaats van de Schrödinger vergelijking). Daardoor heeft grafeen andere transporteigenschappen dan gebruikelijke materialen. Bovendien is grafeen een veelbelovend materiaal voor toepassingen in nano-elektronica, want het is bijvoorbeeld gemakkelijk te produceren en het vertoont kamertemperatuur ladingsmobiliteiten hoger dan $10^4 - 10^5$ cm^2/Vs. Een grondige studie is nodig om de buitengewone elektronische eigenschappen van grafeen bloot te leggen en om de weg vrij te maken voor de ontwikkeling van grafeen nano-elektronica. In dit proefschrift zijn enkele experimenten beschreven die bijdragen aan een beter begrip van elektronentransport in grafeen.

Enkel- en dubbellaags grafeen zijn halfgeleiders zonder bandgap. De top van de hoogste valentie- en de bodem van de laagste geleidingsband raken elkaar bij het ladingsneutraliteitspunt (LNP). Daardoor gedragen beide grafeensoorten zich als metalen. Van enkel- en dubbellaagse grafeenstructuren met twee gates hebben we in hoofdstuk 3 weerstandsmetingen laten zien als functie van een loodrecht elektrisch veld. In de dubbele laag zagen we een sterke toename van de weerstand bij het LNP als gevolg van het elektrisch veld, terwijl in de enkele laag de weerstand niet veranderde. Dit experiment toonde aan dat dubbellaags grafeen veranderd kan worden van metaal naar isolator door een bandgap te openen. Bovendien hebben we laten zien dat in het isolerende regime de geleiding het beste beschreven wordt door een transportmechanisme waarbij de elektronen over variabele afstanden hoppen.

Terwijl enkel- en dubbellaags grafeen halfgeleiders zijn zonder een bandgap, is drielaags grafeen een metaal met een kleine bandoverlap. In hoofdstuk 4 hebben we weerstandsmetingen van drielaags grafeen bij het LNP laten zien als functie van temperatuur en loodrecht elektrisch veld. In tegenstelling tot dubbellaags grafeen, waarvan de weerstand toeneemt door een toenemend elektrisch veld (doordat een bandgap opent), neemt de weerstand van drielaags grafeen af. Met deze experimenten hebben we laten zien dat de bandoverlap groter wordt door een toenemend elektrisch veld, wat consistent is met theoretische voorspellingen.

In ideaal grafeen gaat de ladingsdichtheid naar nul bij het LNP, terwijl de geleiding niet naar nul gaat. Elektronentransport bij het LNP wordt nog steeds niet volledig begrepen. In hoofdstuk 5 hebben we fasecoherent transport in enkellaags grafeen bestudeerd door het transport in supergeleidende grafeenjuncties te meten (lengte $\lesssim$500 nm). We observeerden Josephson superstromen in alle juncties, onafhankelijk van de ladingsdichtheid. Dit toont aan dat elektronentransport in grafeen fasecoherent is, zelfs bij het LNP. Deze waarnemingen staan echter in contrast met de magnetotransportmetingen in dezelfde juncties, waarin werd laten zien dat zwakke lokalisatie van elektronentoestanden sterk onderdrukt wordt of zelfs afwezig is. We kunnen dit sample-specifieke gedrag begrijpen door de bijzondere bandenstructuur van grafeen te beschouwen.

In hoofdstuk 6 hebben we het Aharonov-Bohm (AB) effect in een ringvormige structuur van grafeen onderzocht. Door het AB-effect ontstaan periodieke geleidingsoscillaties als functie van magnetisch veld. Wij vonden dat de amplitude van deze oscillaties lineair afhankelijk is van de gemiddelde geleiding en dat de oscillaties verdwijnen bij het LNP (waar de geleiding het laagst is). Verder vonden we dat de amplitude van de oscillaties toeneemt bij een hoog magnetisch veld. Een fysische verklaring voor deze waarnemingen moet nog gevonden worden.

In grafeen nanoribbons verschijnt een transportgap bij lage ladingsdichtheden, wat isolerend gedrag met zich meebrengt. In hoofdstuk 7 hebben we de gemiddelde geleiding in de transportgap onderzocht als functie van temperatuur en magnetisch veld. Wij vonden dat de gemiddelde geleiding toeneemt met toenemend magnetisch veld en verzadigt bij hoge velden. Een verklaring voor deze waarnemingen kan zijn dat elektronentoestanden sterk gelokaliseerd worden, waarbij de lokalisatielengte toeneemt door een magnetisch veld. De temperatuursafhankelijkheid van de gemiddelde geleiding in de transportgap geeft aan dat transport gebeurt door elektronen die over variabele afstanden hoppen.

Samengevat: in dit proefschrift hebben we laten zien dat we controle kunnen hebben over de bandenstructuur van dubbel- en drielaags grafeen. Simpelweg door het aanleggen van een loodrecht elektrisch veld kunnen we een bandgap openen in dubbellaags en de bandoverlap vergroten in drielaags grafeen. Verder hebben we laten zien dat elektronentransport in kleine grafeenstructuren (lengte $\sim 0.1-1\ \mu$m) fasecoherent is bij cryogene temperaturen ($T \lesssim 4$ K). We hebben zwakke lokalisatie, bipolaire superstromen en het Aharonov-Bohm effect waargenomen. Verder hebben we laten zien dat een transportgap ontstaat in grafeen nanoribbons (breedte $\lesssim$100 nm) door sterke lokalisatie van elektronentoestanden. Onze experimentele resultaten verschaffen meer inzicht in het elektronentransport in grafeen en zijn daarmee een eerste stap in de ontwikkeling van grafeen nano-elektronische systemen.

CURRICULUM VITAE

Jeroen Bart OOSTINGA

13-02-1975	Born in Aduard, The Netherlands.

EDUCATION

1981–1987	Primary school, Christelijke Lagere School "De Tweesprong", Leek, The Netherlands
1987–1993	Secondary school (VWO), Christelijke Scholengemeenschap "De Waezenburg", Leek, The Netherlands
1993–1999	MSc Applied Physics (WO), University of Groningen, The Netherlands Supervisor: prof. dr. ir. T. M. Klapwijk
2006–2010	PhD research at Delft University of Technology, Delft, The Netherlands (2008–2010: two years' stay at University of Geneva, Switzerland) Promoters: prof. dr. H. W. M. Salemink and prof. dr. A. F. Morpurgo

WORK EXPERIENCE

1999-2006	Research scientist, TNO Physics and Electronics Laboratory, TNO Defence, Security and Safety, The Hague, The Netherlands

LIST OF PUBLICATIONS

1. J. B. Oostinga, B. Sacépé, M. F. Craciun, A. F. Morpurgo
   Magnetotransport through graphene nanoribbons
   Submitted to Physical Review Letters (2010)

2. I. Heller, S. Chatoor, J. Männik, M. A. G. Zevenbergen, J. B. Oostinga, A. F. Morpurgo, C. Dekker, S. G. Lemay
   Charge noise in graphene transistors
   Submitted to Nano Letters (2010)

3. X. Liu, J. B. Oostinga, A. F. Morpurgo, L. M. K. Vandersypen
   Electrostatic confinement of electrons in graphene nanoribbons
   Physical Review B **80** (12), 121407 (2009)

4. M. F. Craciun, S. Russo, M. Yamamoto, J. B. Oostinga, A. F. Morpurgo, S. Tarucha
   Trilayer graphene is a semimetal with gate-tunable band overlap
   Nature Nanotechnology **4** (6), 383-388 (2009)

5. S. Russo, J. B. Oostinga, D. Wehenkel, H. B. Heersche, S. Shams Sobhani, L. M. K. Vandersypen, A. F. Morpurgo
   Observation of Aharonov-Bohm conductance oscillations in a graphene ring
   Physical Review B **77** (8), 085413 (2008)

6. J. B. Oostinga, H. B. Heersche, X. Liu, A. F. Morpurgo, L. M. K. Vandersypen
   Gate-induced insulating state in bilayer graphene devices
   Nature Materials **7** (2), 151-157 (2008)

7. H. B. Heersche, P. Jarillo-Herrero, J. B. Oostinga, L. M. K. Vandersypen, A. F. Morpurgo
   Manifestations of phase-coherent transport in graphene - The Josephson effect, weak localization, and aperiodic conductance fluctuations
   European Physical Journal - Special topics **148**, 27-37 (2007)

8. H. B. Heersche, P. Jarillo-Herrero, J. B. Oostinga, L. M. K. Vandersypen, A. F. Morpurgo
   Induced superconductivity in graphene
   Solid State Communications **143** (1-2), 72-76 (2007)

9. H. B. Heersche, P. Jarillo-Herrero, J. B. Oostinga, L. M. K. Vandersypen, A. F. Morpurgo
   Bipolar supercurrent in graphene
   Nature **446** (7131), 56-59 (2007)

10. W. A. Schoonveld, J. B. Oostinga, J. Vrijmoeth, T. M. Klapwijk
    Charge trapping instabilities of sexithiophene Thin Film Transistors
    Synthetic Metals **101** (1-3), 608-609 (1999)

Propositions

accompanying the dissertation

QUANTUM TRANSPORT IN GRAPHENE

by

Jeroen B. OOSTINGA

1. Graphene is a promising material for future high-speed nano-electronic devices, because it is an excellent electrical conductor with a high crystal quality and a high room temperature charge carrier mobility. (chapters 1 and 2)
2. The tunability of the bandgap and band overlap in bilayer and trilayer graphene, respectively, are unique properties that can be used to distinguish bi- and trilayer from single-layer graphene. (chapters 3 and 4)
3. Due to strong intervalley scattering, electronic states in disordered graphene nanoribbons can be strongly localized. (chapter 7)
4. Progress and innovations in science, research and development are slowed down when non-experts try to micromanage them.
5. Modern organizations often push the ideal that employees should manage themselves and be responsible for their own employability. However, this does not seem to hold during reorganizations, when organizations usually force full control of their employees, violating their ideal without any self-criticism.
6. The more rules and procedures are implemented to increase the efficiency of organizations, the less efficient individual employees are working.
7. There is one European Union, but the European Union will never be one unity.
8. The greatness of a nation and its moral progress can be judged by the way its animals are treated (Mahatma Gandhi, 1869-1948). The Dutch policy of destroying healthy animals preventively when the human health is in danger shows that the Dutch society is still uncivilized.
9. By the numerous speculations about the economic crisis, terroristic threats and flu pandemics, the Dutch media spread more anxiety than useful information. Therefore, the media are a major cause of the growing unrest in the Dutch society and should take their responsibility for this.
10. The average intelligence level of programs on Dutch television reflects the average intelligence level of Dutch citizens.

These propositions are considered opposable and defendable and as such have been approved by the supervisors prof. dr. H. W. M. Salemink and prof. dr. A. F. Morpurgo.

Stellingen

behorende bij het proefschrift

QUANTUM TRANSPORT IN GRAPHENE

door

Jeroen B. OOSTINGA

1. Grafeen is een veelbelovend materiaal voor toekomstige snelle nano-elektronica, omdat het een voortreffelijke elektrische geleider is met een hoge kristalkwaliteit en een hoge kamertemperatuur ladingsmobiliteit. (hoofdstukken 1 en 2)
2. De instelbaarheid van de bandgap en de bandoverlap in respectievelijk tweelaags en drielaags grafeen zijn unieke eigenschappen waarmee twee- en drielaags van enkellaags grafeen onderscheiden kunnen worden. (hoofdstukken 3 en 4)
3. Door sterke intervalley scattering kunnen elektronentoestanden in wanordelijke grafeen nanoribbons sterk gelokaliseerd worden. (hoofdstuk 7)
4. Voortgang en vernieuwing in wetenschap, onderzoek en ontwikkeling worden afgeremd als ondeskundigen proberen ze te micromanagen.
5. Moderne organisaties dringen vaak aan op het ideaal dat werknemers zelfstuurbaar en verantwoordelijk voor hun eigen employabiliteit moeten zijn. Dit lijkt echter niet te gelden tijdens reorganisaties, wanneer organisaties gebruikelijk de volledige leiding over hun werknemers afdwingen, waarmee ze zonder enige zelfkritiek geweld doen aan hun ideaal.
6. Hoe meer regels en procedures geïmplementeerd worden om de efficiëntie van organisaties te verhogen, hoe minder efficiënt individuele werknemers gaan werken.
7. Er is één Europese Unie, maar de Europese Unie zal nooit één zijn.
8. De mate van beschaving van een samenleving is af te meten aan de wijze waarop deze met dieren omgaat (Mahatma Gandhi, 1869-1948). Het Nederlandse beleid om gezonde dieren preventief te ruimen wanneer de menselijke gezondheid in gevaar is, laat zien dat de Nederlandse samenleving nog steeds onbeschaafd is.
9. Door de talrijke speculaties over de economische crisis, terroristische dreigingen en griepepidemieën verspreiden de Nederlandse media meer angst dan zinvolle informatie. De media zijn daarom een belangrijke oorzaak van de groeiende onrust in de Nederlandse samenleving en dienen hiervoor hun verantwoordelijkheid te nemen.
10. Het gemiddelde intelligentieniveau van Nederlandse televisieprogramma's is een afspiegeling van het gemiddelde intelligentieniveau van de Nederlandse burgers.

Deze stellingen worden opponeerbaar en verdedigbaar geacht en zijn als zodanig goedgekeurd door de promotoren prof. dr. H. W. M. Salemink en prof. dr. A. F. Morpurgo.